

McGILL UNIVERSITY

DOCTORAL THESIS

**Single-Molecule Microscopy of Polymers
and Nanoparticles in Confinement with
Applications to Genetic Medicines and
Vaccines**

Author:

Albert Kamanzi

Supervisor:

Dr. Sabrina R. LESLIE

April 2021

*A thesis submitted to McGill University in partial fulfillment of the requirements of the
degree of Doctor of Philosophy*

©Albert Kamanzi 2021

Department of Physics

I dedicate this work to: my wife (Marie Ange Umutesi) for her love, support, patience and prayers; to my parents (Alphonse and Philomene Kamanzi) and to all my siblings for all their love, support and prayers.

Acknowledgements

I would like to start by thanking my supervisor Prof. Sabrina Leslie for giving me the opportunity to join her lab and pursue this work. I would also like to thank her for believing in my work even when results were slow to come by. Her continued support, energy, leadership and advice made this work possible.

I would also like to thank current and former members of the Leslie lab for all the support, interesting discussions, advice, and overall fun work environment. In particular, I would like to thank: Dr. Jason Leith for training me when I joined the lab and working together on the confinement paper; Yifei Gu for great team work on the Lipid Nanoparticle (LNP) project; Dr. Daniel Berard for providing me with CLiC devices, technique support, as well as interesting micro-fab discussions; Dr. Romain Berti for analysis and programming support and for helping me with project management; Dr. Radin Tahvildari for micro-fab support and collaboration on the LNP project; Dr. Kimberly Metera for interesting discussions and always answering my chemistry questions; Zhiyue Zhang, and Dr. Marjan Shayegan for their background work that contributed to the LNP paper.

Many undergraduates also contributed to the project including Zach Friedenberger and Raffles Zhu, who carried on from Zhiyue Zhang's MSc thesis, and I am very grateful for their multi-year support of our theory and data analysis development. Wendy Xu, Yash Patel, Haoran Liao also helped develop data analysis and I am grateful for their

time and contributions.

I would also like to thank Dr. Martin Kurylowicz for his support as the person of contact, during my Mitacs internship at Scopesys, as well as for his contributions throughout the LNP paper and project, especially with his background in nanoparticle science.

Next, I would like to thank all the collaborators on both papers presented for making this work possible, including Dr. Hendrick W. de Haan, Dr. David Sean, and Prof. Gary Slater who supported my research on confined polymers; as well as Dr. Dominik Witzigmann, Dr. Jayesh A. Kulkarni, Jerry Leung and Prof. Pieter Cullis who supported my research on confined lipid nanoparticles and applications to genetic medicines. I would like to thank Prof Mark Sutton for being a go-to support for interpreting noisy data and theory development in our team.

Further to this I am extremely grateful to McGill Physics and technicians Robert Gagnon, Richard Talbot, John Smeros for help in general operations of the Leslie Lab, such as air to float our optical tables and maintenance and support. And to the IT staff including Juan Gallego who readily helped with our server and computational needs.

Throughout my PhD, I am grateful for the opportunity to learn inventive work and processes with Dr. Leslie, as well as entrepreneurship. As part of this, I would like to thank Derrick Wong for his guidance in writing our reports of inventions and patents, as well as guidance on the startup company Scopesys being spun out of Dr. Leslie's lab. His guidance on intellectual property was really helpful to me and my team.

I would also like to thank Prof Vincent Tabard-Cossa and his team for our

collaboration that we started during part of my PhD, although we had to put on hold; which integrates nanopores with CLiC imaging and devices. I am excited to have taken the first data on the double-layer CLiC flow cell and look forward to seeing additional PhD students in the LeslieLab continue to pursue this concept. On this note I am grateful to the McGill Nanotools and INRS Facility and staff for extensive help and training in fabrication tools and methods, which helped me learn how to make micro/nano wells, grooves, and channels.

In closing, I acknowledge that I am submitting my thesis in an unusual year. I would like to especially thank Prof. Sangyong Jeon, Dept Chair, for his leadership of the Dept. during this time and providing me and us with access to the lab during the international COVID19 crisis. I am hopeful that my work will provide new tools which help with understanding and developing new vaccines and medicines, and grateful for the opportunity to continue my work and be part of the bigger picture.

Statement of Originality

I, Albert Kamanzi, claim that the following elements of this thesis are distinct contributions to original knowledge and are considered to be original scholarship:

- Used Convex Lens induced Confinement (CLiC) imaging to directly measure changes in concentration of free diffusing DNA polymers as a function of slit-like confinement, for a wide range of confinement heights (i.e from less than the Kuhn length of molecules to at least an order of magnitude larger than the radius of gyration of the molecules). [Published: *Leith, J.S.**, Kamanzi, A.*, *et al.* 2016. *Macromolecules*, 49(23), pp.9266-9271]
- Used results of my CLiC experiments, in addition to simulations developed to support this work, in order to obtain the transition in free energy of the polymers as a function of nano confinement. Connected my results to predictions of theoretical models to draw conclusions on scaling coefficients on the fundamental properties of biopolymers, which had not yet been validated in the literature. [Published: *Leith, J.S.**, Kamanzi, A.*, *et al.* 2016. *Macromolecules*, 49(23), pp.9266-9271]
- Used a combination of single-particle CLiC microscopy and micro/nano-fabricated wells in glass surfaces to confine, isolate and image freely diffusing and fluorescently labeled Lipid Nanoparticles (LNPs). More broadly speaking, this was the beginning

of pioneering lipid nanoparticle analytics using the CLiC single-particle imaging platform, with applications to vaccines and genetic medicines which we are now pursuing. [Manuscript in review: Kamanzi, A.*, *et al.* 2021.]

- Trialed a number of surface coatings in order to overcome the technical issue of lipid nanoparticles sticking to glass. Used advice from collaborators to permute recipes and eventually come to a solution, variations of which are now working for more than one kind of drug-delivery particle. [Manuscript in review: Kamanzi, A.*, *et al.* 2021.]
- Used the above method to track and size individual lipid nano particles for long times, and then build the distributions of size and cargo loading. This data enabled us to probe structural information from the scatter plots of particle size and loading, where each data point corresponded to a single particle. My paper establishes the first technique to simultaneously measure size and loading with single-particle resolution, in solution and without tethers, and in cell-like conditions. [Manuscript in review: Kamanzi, A.*, *et al.* 2021.]
- Used a combination of the above method, higher laser intensity, and photo bleaching measurements to obtain single-particle drug loading measurements with single-dye precision. Used these measurements to strengthen drug loading distributions in combination with the above experiments performed at lower laser intensity. [Manuscript in review: Kamanzi, A.*, *et al.* 2021.]
- Acquired preliminary imaging data on the fusion of single lipid nanoparticles in

solution, using the CLiC technique in combination with FRET. This is referenced in the outlook to my first LNP paper, cited here. This data and achievement will appear in a follow-up paper, beyond the scope of this thesis due to time limitations [Manuscript in Preparation: Kamanzi, A.*, *et al.* 2021.]

- Contributed to the design and fabrication of flow cells and devices, and acquisition of preliminary data, to combine confinement microscopy with sensors beyond fluorescence microscopes, such as with nanopore. This idea was initially recorded by Dr. Leslie in 2014 and developed into a patent on which I am a co-inventor. The preliminary devices and inventions include a dual-layer flow cell (to allow separation of two layers of fluid), integration of a nanoporous membrane in a flow-cell (between the layers), and integration of arrays of nanopores in flow cells (aligned to nanoscale conduits). I have contributed device design and fabrication, prototyping, and some experiments to help establish these concepts. This has not yet been published in manuscript format due to time limitations. I may publish the contributions in engineering journals as a next step. They will contribute important ground work to future research projects and developments. [Patent pending: S. R. Leslie, D.J. Berard, G. Henkin, A. Kamanzi, F. Michaud, Nanofluidic flow cell and method of loading sample: CA 2974368 and US 15/654339]
- Contributed to the design and fabrication of CLiC flow cells and instruments [Patent awarded: S. R. Leslie, D.J. Berard, A. Kamanzi, Flow cell: CA 184477 and US

29/611,297]

Contribution of Co-authors

This is a manuscript-based. One paper is published [1], and one paper is in review. Beyond these papers, I have contributed to two review articles by Dr. Leslie as a co-author, and two patents listed in the statement of originality. Here, I will outline the contributions of co-authors on the two manuscripts which are the main body of this thesis.

Chapter 2 is based on the following published manuscript:

Free energy of a polymer in slit-like confinement from the Odijk regime to the bulk. Leith, J.S.*, Kamanzi, A.*, Sean, D., Berard, D., Guthrie, A.C., McFaul, C.M., Slater, G.W., de Haan, H.W. and Leslie, S.R., *Macromolecules*, 49(23), pp.9266-9271. (2016)

I am a co-first author on this paper. I conducted all the experiments, collected all of the data, and analyzed most of the data presented in the figures of this paper. This data collection effort built on substantial background. S. Leslie, J.S. Leith and I designed the experiments, J.S. Leith performed most of the preliminary experiments prior to my experiments, and we collaborated on the analysis tools. It is worth pointing out that this project was conducted throughout the setup of Dr. Leslie's first lab at McGill and built directly on her post doctoral research, instrumentation, flow cells and codes to which she was the sole main developer. D. Sean and H.W. de Haan advised on the

theory, designed and executed the simulation tools for this study. D. Berard and S. Leslie designed the upgraded CLiC device used for these studies, and contributed to the initial experiments. A.C. Guthrie, C.M. McFaul and D. Berard made additional contributions to the analysis tools. G.W. Slater advised D. Sean and H.W. de Haan, and reviewed the manuscript. In addition to myself, J.S Leith, D.Sean, H.W. de Haan, and S.R Leslie assisted in writing the manuscript, with contributions from co authors in editing. S.R. Leslie initiated, supervised, and lead the overall project and invited the Slater team to assist with theoretical and simulation support.

Chapter 3 is based on the following manuscript:

Simultaneous, single-particle measurements of size and loading give new insights into the structure of drug-delivery nanoparticles Kamanzi, A., Gu, Y., Tahvildari, R., Friedenberger, Z., Xu, R., Berti, R., Kuryłowicz, M., Witzigmann, D., Kulkarni, J.A., Leung, J., Andersson, J., Dahlin, A., Hook, F., Cullis, P.R., Sutton, M., Leslie S.R., to be submitted.

I conducted most of the experiments presented in the paper (half of the experiments in Figure 3.1, all the experiments in Figures 3.2 - 3.6, and some of the experiments in Figure B.1 and Table B.2), and was responsible for day to day operations of the project - especially during the pandemic shutdown. This included daily collaboration in the lab with M.Sc. student Y. Gu, running and planning experiments, presenting at weekly update meetings with Dr. Leslie and my team.

I optimized the flow-cell surfaces to minimize surface interactions, an effort which took

from 2018 til recently to complete successfully and through much trial and error. This included testing several glass surface passivation protocols including PEG-Silane, PLL-PEG, several silanization protocols and several multi-step PEGylation protocols. I also worked on the analysis tools and simulations with Dr. R. Berti and others to optimize them for LNP experiments. I contributed to analyzing the experiments, preparing the data for presentation in weekly meetings for feedback and made the figures of the paper in collaboration with my team. Overall I worked on all aspects of the project and contributed significantly to writing the paper along with Dr. Leslie and my team.

Y. Gu performed most of the experiments in Figure B.1 and Table B.2 - to support corrections for confinement effects - and half of the experiments in Figure 3.1. She worked alongside Kamanzi on passivating surfaces for the experiments. She also contributed to analyzing the data, as well as to the simulations used to optimize experimental parameters.

Dr. R. Tahvildari performed preliminary experiments on particle sizing and photo-bleaching measurements using another kind of nanoparticles, which were used as input to optimizing our analysis and simulation tools. He fabricated the flow cells for this project. He also supported execution of analysis of data presented in this paper.

Dr. R. Berti lead the design and development of the overall analysis tools and simulation platform, guided closely by Dr. Leslie and with important technical contributions from Z. Friedenberger, Z. (Raffles) Xu, and Dr. M. Sutton on analysis and theory. Dr. R. Berti also helped with planning schedules for the project, especially during the COVID19 lockdown when we needed to adapt to a new way of working with

fixed schedules.

Dr. M. Kurylowicz worked on the preliminary experiments with Dr. Tahvildari on another kind of nanoparticle, helped with the literature review of sizing methods, advised and discussed results, and provided expertise on nanoparticle science. Dr. Kurylowicz, Dr. Berti, myself and Dr. Leslie made the most significant writing contributions to the manuscript and the extensive Supporting Information (SI).

Dr. D. Witzigmann, Dr. J.A Kulkarni and J. Leung provided lipid nanoparticle samples, through the collaborative relationship between S.R Leslie and P.R. Cullis, as well as discussed results in a collaboration meeting which was held every few months.

Dr. F. Hook, Dr. A. Dahlin and Mr. J Andersson advised on the final selection of surface passivation treatments to optimize for LNP experiments. This advice took place since late 2019 and helped minimize particles sticking to surfaces.

Dr. P. Cullis supported the project through discussions with S.R. Leslie, perspective on the field, and his lab provided the samples.

Dr. S. Leslie initiated, lead and supervised all aspects of the project and strongly supported the writing of the manuscript. Dr. S. Leslie's interaction with the project was on a daily or weekly basis throughout its duration. She also managed interactions with collaborators given the complexity of the project, which required microscopy, biophysics, surface chemistry, lipid nanoparticle biochemistry, computational and theoretical expertise to complete in addition to team work.

Abstract

The Coronavirus pandemic has highlighted the need for next-generation oligonucleotide (RNA or DNA) based medicines. However, development of such therapeutics faces novel challenges which will require new technology and instrumentation with single-molecule resolution to solve. One promising technology is lipid nanoparticle (LNP) drug delivery vehicles, which have proven to be a powerful tool for rapid response towards combatting new viruses. Optimizing the design of LNPs for drug delivery depends on being able to resolve, understand, and predict their biophysical and therapeutic properties, as a function of design parameters, as well as those of their oligonucleotide cargo in cell-like environments.

While existing tools have made great progress, gaps in understanding remain because of the inability to make detailed measurements of these biophysical properties with the necessary resolution. This thesis contributes to the development and application of a single-molecule platform for high-resolution measurements of the biophysics of nanomedicines, vaccines and biopolymers. It is based on the technique of Convex Lens-induced Confinement (CLiC) first introduced by my supervisor.

In chapter 2, we first apply CLiC to directly measure the free energy of confinement for semi-flexible biopolymers (i.e. DNA molecules) from the nanoscale to bulk regimes in slit-like confinement. We achieve this by loading molecules – freely diffusing in solution – into a chamber of continuously increasing height. By choosing a relatively

short polymer (linearized pUC19), we can access a continuum of confinement regimes. Hence our results provide a bridge with which to connect scaling theories established for qualitatively different regimes: including the Odijk theory describing sub-persistence-length confinement; the interpolation model by Chen and Sullivan extending Odijk to moderate confinement; and the Casassa theory describing the transition from moderate confinement to bulk. In addition, the results establish a robust, quantitative platform for understanding and manipulating biopolymers at the nanoscale, with key applications and insights toward emerging medicines and biotechnologies.

Next, we introduce a new application for CLiC imaging (chapter 3): namely single nanoparticle science, and more especially lipid nanoparticles which carry genetic medicines. This includes a general imaging and analysis method to isolate and simultaneously track many copies of single, freely diffusing lipid nanoparticles. This method uses CLiC microscopy in combination with microfabricated trapping wells to isolate and quantify the diffusive trajectories and fluorescent intensities of nanoparticles for long times. To validate this approach, We first apply the technique on fluorescent polystyrene nanoparticles and compare results to prior data. Next, we develop a simulation and analysis platform to interpret the images and optimize parameter selection for the experiments. These include characterizing the impact of well confinement, exposure time and signal-to-noise ratio on our single-particle measurements of lipid nanoparticles.

We apply this approach to investigate the size and loading properties of lipid

nanoparticle vehicles containing short interfering RNA (siRNA), as a function of lipid formulation, solution pH, and loading. With these measurements, we obtain new insights into LNP structure and how the siRNA is distributed in the LNP, enabled by taking a detailed look at the correlation between the intensity and size measurements. Beyond introducing a new analytic for size and loading, this work opens the door to new studies of dynamics, such as LNP fusion and drug-release kinetics. The broad impact is to help create a through-line of understanding between microscopic and macroscopic properties of drug-delivery vehicles as a function of design parameters, and by enabling this new information, help accelerate drug development and discovery.

Abrégé

La pandémie de coronavirus a mis en évidence le besoin de médicaments à base d'oligonucléotides (ARN ou ADN) de nouvelle génération. Cependant, le développement de telles thérapies est confronté à de nouveaux défis qui nécessiteront une nouvelle technologie et une instrumentation avec une résolution à une seule molécule pour être résolus. Une technologie prometteuse est celle des véhicules de médicaments à base de nanoparticules lipidiques (NPL), qui se sont révélés être un outil puissant pour une réponse rapide à la lutte contre les nouveaux virus. L'optimisation de la conception des NPL pour l'administration de médicaments dépend de la capacité à résoudre, comprendre et prédire leurs propriétés biophysiques et thérapeutiques, en fonction des paramètres de conception, ainsi que celles de leur cargaison d'oligonucléotides dans des environnements de type cellulaire.

Alors que les outils existants ont fait de grands progrès, des lacunes dans la compréhension subsistent en raison de l'incapacité de faire des mesures détaillées de ces propriétés biophysiques avec la résolution nécessaire. Cette thèse contribue au développement et à l'application d'une plateforme dédiée aux molécules uniques pour des mesures haute résolution de la biophysique des nanomédicaments, des vaccins et des biopolymères. Elle est basée sur la technique de Confinement induit par une lentille convexe (CLiC) introduite pour la première fois par mon superviseur.

Dans le chapitre 2, nous appliquons d'abord CLiC pour mesurer directement

l'énergie libre de confinement pour des biopolymères semi-flexibles (c'est-à-dire les molécules d'ADN) depuis l'échelle nanométrique jusqu'à des régimes moins contraints dans un confinement de type fente. Nous y parvenons en chargeant des molécules - diffusant librement en solution - dans une chambre de hauteur croissante. En choisissant un polymère relativement court (pUC19 linéarisé), nous pouvons accéder à un continuum de régimes de confinement. Par conséquent, nos résultats fournissent un pont avec lequel relier les théories d'échelle établies pour des régimes qualitativement différents: y compris la théorie d'Odijk décrivant le confinement en dessous de la longueur de persistance; le modèle d'interpolation de Chen et Sullivan étendant Odijk à un confinement modéré; et la théorie de Casassa décrivant la transition du confinement modéré au volume. En outre, les résultats établissent une plateforme quantitative robuste pour comprendre et manipuler les biopolymères à l'échelle nanométrique, avec des applications et des informations clés sur les médicaments et les biotechnologies émergentes.

Ensuite, nous introduisons une nouvelle application pour l'imagerie CLiC (chapitre 3): à savoir la science des nanoparticules uniques, et plus particulièrement les nanoparticules lipidiques porteuses de médicaments génétiques. Cela comprend une imagerie générale et une méthode d'analyse pour isoler et suivre simultanément de nombreuses copies de nanoparticules lipidiques uniques et diffusant librement. Cette méthode utilise la microscopie CLiC en combinaison avec des puits de piégeage microfabriqués pour isoler et quantifier les trajectoires de diffusion et les intensités de fluorescence des nanoparticules pendant de longues périodes. Pour valider cette

approche, nous appliquons d'abord la technique sur des nanoparticules fluorescentes de polystyrène et comparons les résultats aux données antérieures. Ensuite, nous développons une plateforme de simulation et d'analyse pour interpréter les images et optimiser la sélection des paramètres pour les expériences. Il s'agit notamment de caractériser l'impact du confinement dans les puits, le temps d'exposition et le rapport signal sur bruit pour nos mesures de particules uniques de nanoparticules lipidiques.

Nous appliquons cette approche pour étudier la taille et les propriétés d'encapsulation des véhicules de nanoparticules lipidiques contenant des petits ARN interférents (pARNi), en fonction de la formulation des lipides, du pH de la solution et de l'encapsulation. Avec ces mesures, nous obtenons de nouvelles informations sur la structure de la NPL et la façon dont le pARNi est distribué dans la NPL, grâce à un examen détaillé de la corrélation entre les mesures d'intensité et de taille. Au-delà de l'introduction d'une nouvelle analyse de la taille et du chargement, ce travail ouvre la porte à de nouvelles études de dynamique, telles que la fusion LNP et la cinétique de libération de médicaments. L'impact général est d'aider à créer une compréhension globale entre les propriétés microscopiques et macroscopiques des véhicules d'administration de médicaments en fonction des paramètres de conception, et en permettant ces nouvelles informations, d'aider à accélérer le développement et la découverte de médicaments.

Contents

Acknowledgements	ii
Statement of Originality	v
Contribution of Co-authors	ix
Abstract	xiii
Abrégé	xvi
List of Figures	xxiii
1 Introduction	1
1.1 Convex Lens induced Confinement (CLiC)	3
1.2 Ionizable Lipid Nanoparticles	5
1.3 Existing Particle Sizing Techniques	6
1.4 Outline of Thesis	9
2 Free Energy of a Polymer in Slit-like Confinement	13
2.1 Abstract	13
2.2 Introduction	14
2.3 Experimental Section	19

2.4	Results and Discussion	22
2.4.1	Experimental Results	22
2.4.2	Monte Carlo (MC) Simulations	23
2.4.3	Langevin Dynamics (LD) Simulations	25
2.4.4	Discussion	27
2.5	Conclusion	29
3	Single LNP size and loading measurements	32
3.1	Abstract	32
3.2	Introduction	34
3.3	Results	37
3.3.1	Validation of Single-particle Diffusivity Measurements	37
3.3.2	Particle Structure vs pH	41
3.3.3	Control measurements: Bilayer LNPs	45
3.3.4	siRNA drug-loading with single-molecule resolution	46
3.3.5	Simultaneous size and loading measurements of siRNA-LNPs	50
3.4	Discussion	52
3.5	Conclusion	55
3.6	Materials and Methods	56
3.7	acknowledgement	63
4	Conclusion and Outlook	64

A SI: Free Energy of a Polymer in Slit-like Confinement	69
A.1 Methods	69
A.1.1 Flow Cell Preparation	69
A.1.2 DNA Sample Preparation	70
A.1.3 Microscope and Illumination	71
A.1.4 CLiC Microscopy Setup	73
A.1.5 Data Collection	74
A.2 Data Analysis	75
A.2.1 Chamber Height Characterization	75
A.2.2 Particle Identification and Trajectory Analysis	79
A.2.3 Counting Particles as a Function of Height	79
A.2.4 Calculating the Confinement Potential	81
A.2.5 Assigning Bulk Concentration per Dataset	81
A.3 Simulations	83
B SI: Single LNP size and loading measurements	89
B.1 Comparisons with other sizing techniques	89
B.2 Particle detection, tracking and sizing	93
B.2.1 Pyramid approach to particle detection	93
B.2.2 Single-particle tracking in confinement	94
B.2.3 Corrections for size measurement under parallel planes of confinement	96
B.3 LNP cargo-loading distributions	98

B.3.1 Photobleaching measurements	98
B.4 Simulation of confined particles	100
B.4.1 Optimizing Imaging Parameters: Quantifying Bias and Variance .	100

List of Figures

1.1	Illustration of CLiC microscopy	4
2.1	Schematic of the CLiC device and micrographs of DNA molecules	19
2.2	Concentration of free diffusing linearized pUC19 molecules vs slit height	23
2.3	Scaling of the free energy of confined vs confinement	24
2.4	ΔG_{conf} versus slit height as obtained by the MC and LD simulations	26
3.1	CLiC nanoparticle characterization assay	38
3.2	LNP structural modifications as a function of pH	41
3.3	Control bilayer Lipid nanoparticles	44
3.4	Photobleaching analysis of siRNA-loaded LNPs	47
3.5	LNP drug loading (siRNA) measurements with single-molecule resolution	48
3.6	siRNA drug distribution in LNPs	50
A.1	Chamber height characterization	72
A.2	Distribution of pUC19 molecules in slit-like chamber with varyin heights	75
A.3	ΔG_{conf} versus h , showing the effects of alternative chamber-fitting technique	78
B.1	Diffusion coefficient measurements vs confinement depth	97
B.2	Simulation validation	102

Chapter 1

Introduction

The need for a next-generation gene therapy and oligonucleotide-based medicine has never been clearer: at least two of the currently approved vaccines for Covid-19 [2, 3] use lipid nanoparticles to deliver mRNA molecules which code for the production of coronavirus spike proteins. These in turn enable the body's defence mechanism to recognize coronavirus and inhibit its viral replication. Additionally, gene therapy has enormous potential to treat or cure a wide range of diseases including immunological disorders, cancers, hereditary conditions, and rare diseases by silencing or correcting pathogenic genes or causing therapeutic proteins to be expressed. The programmable nature of oligonucleotide drugs means that, in theory, personalized medicines can be rationally designed based on defined rules. Genetic drugs include short interfering RNA (siRNA) and antisense oligonucleotides (ASOs) for silencing pathogenic genes, messenger RNA (mRNA) for expressing therapeutic proteins, and CRISPR-Cas9 constructs for gene editing.

A key challenge for gene therapies is the successful delivery of these macromolecular drugs since they are degraded in biological fluids, do not accumulate in target tissue, and cannot cross cell membranes to access the interior of target cells. Major efforts have been made to use viral vectors as carriers, but this approach has been constrained by

limited carrying capacity (< 5 kbp), low delivery efficiency, problematic manufacturing processes, and immune reactions that prevent repeated administration [4–6].

Among non-viral delivery systems, lipid nanoparticle (LNP) systems are particularly promising. In 2018 patisiran - sold under the brand name Onpattro® - became the first siRNA therapeutic to gain US FDA regulatory approval. Onpattro® employs an LNP delivery system to deliver siRNA inside hepatic cells following intravenous administration [7]. The key advance enabling the LNP delivery system was the identification of optimized ionizable cationic lipids that not only facilitate siRNA encapsulation but also enhance intracellular delivery of the siRNA following uptake into target cells [8]. Pre-clinical studies have shown that related LNPs may effectively deliver much larger mRNA-based drugs [9–12], and have promise for protein replacement therapies and vaccine applications. Due to agreeable characteristics such as ease of manufacture, lack of immune response, large carrying capacity, and favourable interactions with endosome membranes, LNP formulations of genetic drugs are undergoing extensive pharmaceutical development [13].

Here, we present a suite of single-molecule and single-particle methods and experiments that we have devised to study how nucleic acid molecules respond to incrementally smaller spaces of applied confinement, emulating naturally occurring nano confinement environments. We then apply the same techniques to study lipid nanoparticles, by measuring their sizes at the single-particle level and their loading of siRNA drug cargo with single-molecule resolution. The overarching vision of our research is to investigate the complex behavior of biomolecules, such as protein, DNA, and RNA, in nanoscale confined spaces which mimic cellular and subcellular

environments, including the surfaces and interiors of nanoparticles which are used as delivery vehicles for these molecules.

Despite strong interest by both fundamental and applied scientists, investigations of individual macromolecules in these highly confined spaces has presented challenges to existing tools. The state-of-the-art in detecting macromolecular assembly and dynamics is primarily comprised of methods that detect binding of single molecules to each other, to surfaces created by other macromolecules, or to polymers of the cellular cytoskeleton such as DNA or microtubules. Direct imaging of individual molecules under nanoscale confinement has not been possible. Commonly used methods, such as “total internal reflection fluorescence” (TIRF) microscopy, allow detection of the appearance and disappearance of individual molecules on or near to a surface: if molecules are freely diffusing they can only be imaged for very short times before leaving the surface layer. For longer imaging times they can be tethered to the surface, but this changes their chemical identity as well as modifying their conformational degrees of freedom which are essential to macromolecular dynamics and function. We overcome these challenges by using Convex Lens-induced Confinement (CLiC) microscopy as a novel single-molecule imaging technique.

1.1 Convex Lens induced Confinement (CLiC)

As shown in Figure 1.1, the CLiC device is made up of a flow-cell with a deflectable roof and a pusher lens. The deformable glass “lid” is lowered to seal the array of wells and

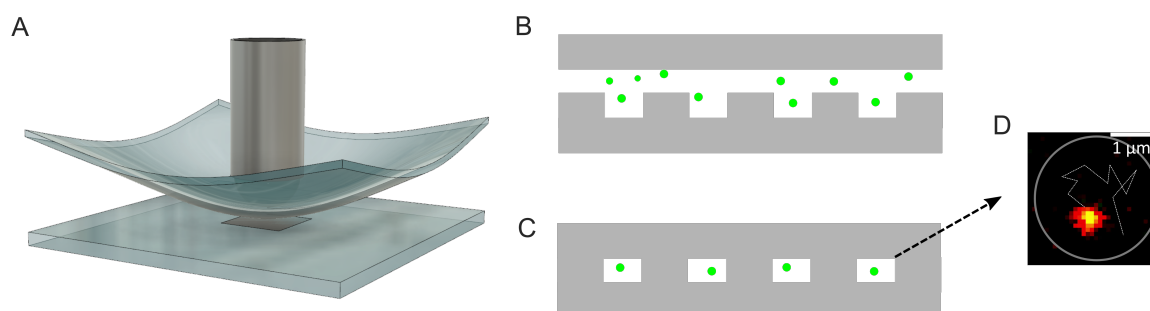


Figure 1.1: Schematic of CLiC microscopy showing: a) illustration of a CLiC chamber - made up of 2 coverslips - being deformed by a pusher lens, to confine samples in nano-features; b) cross-section of the CLiC chamber, showing the nanofabricated features, as well as freely diffusing samples; c) the same cross-section is shown for the case of fully deflected top coverslip, with samples getting tracked in the nanofeatures; and d) fluorescence image of a single particle - trapped in a micro well - that is freely diffusing (the dashed line shows the trajectory of the particle in the preceding frames).

lifted to refresh the sample. This allows for untethered and freely diffusing molecules to be confined to arrays of nano- or micro-scale wells etched into one of the flow-cell's surfaces.

What CLiC provides that TIRF does not allow is the capacity to continuously follow the trajectory of a freely diffusing single molecule for long periods of time, tracking the molecular history from before it is bound to a substrate, when it is bound and when it dissociates. This capability is particularly important in biophysics because many elements of cellular activity, such as DNA transcription or movement of molecules on microtubules, are processive; that is, important biomolecular events are dependent on a sequence of previous events. This history can often be inferred, but not directly measured with current techniques. CLiC microscopy makes it possible to track the full dynamic history of biomolecular events.

By confining and visualizing biomolecules from molecular to microscopic dimensions,

we can directly investigate how confinement physics can regulate macromolecular behavior. CLiC is a new tool which enables us to tackle open biological questions on how physiologically important molecules, DNA or RNA, behave in nanoscale environments such as the cell's nucleus or inside the lipid nanoparticles.

Thus, it is possible that CLiC will contribute to verifying or disproving some of the most fundamental models of biomolecular dynamics, such as DNA-topology-mediated regulation of transcription. Furthermore, by looking at molecules in a thin volume, compared to other techniques, CLiC microscopy can resolve single-molecule trajectories in the presence of reagent concentrations orders of magnitude higher, and over time periods orders of magnitude longer than is possible without confinement. This in turn allows us to discern and follow weak and slow interactions - which are uniquely relevant to a wide variety of biological processes.

1.2 Ionizable Lipid Nanoparticles

Several different types of lipid nanoparticles have been designed for drug delivery applications. In this thesis we use ionizable cationic lipid nanoparticles (LNPs), designed in the Cullis Lab at the University of British Columbia.

The LNPs are made up of 4 different lipid components including several types of ionizable cationic lipids, phospholipid DSPC (1,2-distearoyl-sn-glycero-3-phosphocholine), several types of PEGylated phospholipids (e.g DSPE-PEG2000) as well as Cholesterol. Each of these components has been chosen, and their relative

abundance tuned to achieve desired particle properties including poly-dispersity of the size distributions [14], as well as drug carrying capacity. In particular ionizable cationic lipids allow the LNPs:

- to load negatively charged nucleic acid cargo (i.e mRNA or siRNA molecules), during particle formation, as they are rapidly mixed with intended cargo in low buffer pH (4), and then dialyzed to a higher buffer pH (7.4)
- to keep the cargo safely encapsulated during storage and transport to the intended target tissues, in physiological conditions (pH 7.4)
- to fuse with the target cells and then deliver the drugs, as they experience a drop in pH (4) inside the cells [15]

Hence ionizable lipids have been optimized for drug delivery applications, by tuning their pKa to 6.5, in order for them to undergo transitions in their electrostatic properties. Currently several start-up companies hold patents for producing various types of these lipids [3], including those used for Covid-19 vaccines (e.g Moderna and Acuitas). We use nanoparticles made with DLin-KC2-DMA (KC2) ionizable lipid, a predecessor for DLin-MC3-DMA lipid used in Onpattro® drugs.

1.3 Existing Particle Sizing Techniques

The most commonly used technique to characterize particle size is Dynamic light scattering (DLS) [16], which uses a coherent light source to create a fluctuating

interference pattern due to Brownian motion changing the relative distance between particles [17]. The diffusion constant can be extracted from the decay of the autocorrelation function of these fluctuations, which reflects the time scale of particles moving relative to each other. Particle size information is then obtained from diffusion constant and buffer viscosity, using the Einstein-Stokes relation. This technique has been used to measure the sizes of particles with sub-nanometer resolution [18].

However, the presence of large particles, even in small quantities, skews the results and masks the underlying size distribution. Heterogeneity in particle size within a sample is challenging to quantify, and the indirect interpretation of size from DLS data can obscure results [19] [20]. Single-molecule measurements are required to have a better understanding of the size distribution of samples, and to quantify aggregates or sub-populations with distinct sizes.

Nanoparticle tracking analysis (NTA) is able to measure the sizes of individual particles by imaging their scattering in unconfined solution. However, particles drift in and out of the focal plane of the microscope resulting in significant fluctuations in the scattering intensity [21] and limiting the precision and accuracy of size measurements.

In Atomic force microscopy (AFM), the size and shape of immobilized particles can be estimated with sub-nanometer resolution [22]. However, surface-immobilization may strongly affect the structural properties of the particles, inducing conformational changes such as particle spreading and flattening due to interaction with the surface potential. Moreover, AFM necessarily applies a force to measured objects which can add significant bias [23], especially for soft polymeric materials.

Cryo electron microscopy (Cryo-EM) avoids both staining and fixation by rapidly freezing the particle suspension in liquid ethane [24], [25]. Low throughput, complicated sample preparation protocols, and high cost are all limiting factors for this technique, although it is often used to complement DLS [26]. Hence it is difficult to construct a statistically significant distribution from hundreds or thousands of independent measurements.

Flow cytometry (FC or FCM) is an indirect technique used to analyze single cells and particles in the sub-micrometer range [27]. The optical signal depends on both the size and refractive index of the particle, and drops dramatically with smaller radius. This makes the detection of sub-wavelength particles challenging [28].

In Resistive pulse sensing (RPS) [29] the aperture size must be comparable to the size of the nanoparticles, which poses limitations on the heterogeneity and size range of the sample [30].

Optical tweezers can be used to measure the size of a single nanoparticle, but with such low throughput that it would not be possible to construct a statistically significant distribution from hundreds or thousands of independent measurements. Tethering is also necessary, as well as the application of force, which biases the conformational freedom of the molecule under investigation.

DLS and NTA are both of particular interest for comparison with CLiC data, since as with CLiC these techniques both make direct measurements of diffusivity, and derive size distributions from Stokes-Einstein models relating diffusivity to size. Light scattering techniques measure the correlation time of light scattered from a focal point within a

suspension of particles in a fluid. This is derived from the autocorrelation function of light scattering at a given angle, which is related to the diffusivity of particles traversing the illumination volume. While DLS measures the auto-correlation function for scattered light, CLiC measures the Mean Square Displacement - which is related to the velocity autocorrelation function - to determine particle diffusivity. The similarity in the physical basis of these measurements gives us an opportunity to compare a bulk measurement of an ensemble average to the average over an ensemble of directly measured microscopic states.

1.4 Outline of Thesis

Below is a summary of the content of this thesis. Chapter 2 is based on a published article on the confinement physics of bio-polymers, and Chapter 3 is based on a manuscript soon to be submitted, on the characterization of LNP loading with siRNA for drug delivery applications..

In Chapter 2 we use CLiC microscopy to perform rigorous equilibrium studies of transitions in DNA conformations, from “blob-like” in an unconfined regime, to “rod-like” in a nanoconfined regime. Importantly, we can visualize DNA over several orders of magnitude of applied confinement, in a single experiment and device.

Our research contributes a direct measurement of the “free energy of confinement” experienced by the DNA molecules, over several orders of magnitude of applied confinement. When a flexible polymer is confined, fewer conformations are accessible,

making confinement energetically unfavourable. Our measurement of the confinement free energy is direct: we count the number of DNA molecules, at equilibrium, in a single chamber of smoothly varying height. A much lower density of molecules is observed in regions of the chamber where the height is much smaller than the diameter of unconstrained molecules.

Importantly, our data provide a “bridge” that connects prior measurements and theories in the literature, typically obtained in limiting cases using devices of fixed dimensions. Our experimental data and simulations have served to link (a), “nano confinement theory” (by Odijk [31]), (b), an interpolation model which extends Odijk to “moderate confinement” (by Chen and Sullivan [32]) and (c), “unconfined theory” which describes the transition from moderate to unconfined conditions (by Casassa [33]). In the nanoconfined regime, the applied confinement is so severe that the polymer is unable to form random coils the way it does in free solution; its conformations look like “deflecting stiff segments” off of the walls. In the unconfined regime, the polymer appears as a “blob”, as one would intuitively expect. In between - in moderate confinement - the DNA conformations smoothly transition from a deflecting rod, to a network of blobs, to a single blob, according to theory that our experiments and simulations agree with.

In Chapter 3 we introduce a general imaging and analysis method to isolate and track many copies of single diffusing nanoparticles at once. We confine the particles in an array of circular microwells using the CLiC imaging technique. This enables simultaneous measurements of the size and fluorescence intensity of each particle, without using tethers.

We validate our method by using measurements of polystyrene nanoparticles with known size, as well as developing simulations for guiding the choice of experimental parameter. To correct for confinement effects, we perform a series of experiments with varying well depth, and then compare our results to theoretical models on the scaling of diffusivity with confinement. We establish agreement between our measurements and the mean particle size reported using other methods.

We then apply this method to investigate the structural properties of different formulations of lipid nanoparticles (LNPs) designed for drug delivery. This includes unloaded nanoparticles in two buffer conditions - specifically pH 4 25mM sodium acetate buffer and pH7.4 1xPBS - as well as siRNA loaded LNPs. Our results provide detailed size and loading distributions. This allows us to directly investigate structures of nanoparticles as a function buffer conditions or drug cargo loading.

Additionally, we combine CLiC with photobleaching measurements to measure drug loading with single molecule resolution. Our measurements are sensitive enough to capture single freely diffusing drug molecules, and hence quantify the encapsulation efficiency of the LNPs.

Preface to Chapter 2

Chapter 1 introduces Convex lens induced confinement (CLiC) microscopy, a single molecule imaging technique. In this chapter, we combine CLiC with fluorescent microscopy to study the behavior of biopolymers under applied confinement. We do this by confining linearized pUC19 DNA molecules in a chamber of smoothly increasing gap height. The results section shows how we obtain confinement potential from the concentration of molecules across the imaging chamber.

Chapter 2

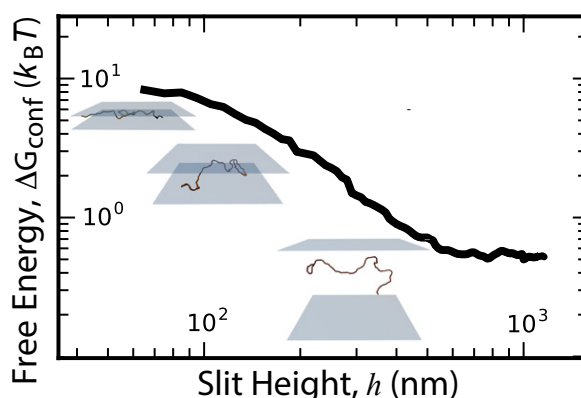
Free Energy of a Polymer in Slit-like Confinement

This section is based on the published manuscript: Leith, J.S.*, Kamanzi, A.*, Sean, D., Berard, D., Guthrie, A.C., McFaul, C.M., Slater, G.W., de Haan, H.W. and Leslie, S.R., 2016. Free energy of a polymer in slit-like confinement from the Odijk regime to the bulk. *Macromolecules*, 49(23), pp.9266-9271.

2.1 Abstract

We directly measure the free energy of confinement for semi-flexible polymers from the nanoscale to bulk regimes in slit-like confinement. We use Convex Lens-induced Confinement (CLiC) microscopy of DNA to directly count molecules at equilibrium in a single chamber of

smoothly increasing height. Our data, acquired across a continuum of confinement regimes, provides a bridge with which to connect scaling theories established for



qualitatively different regimes. We present new experimental data and simulations that connect the Odijk theory describing sub-persistence-length confinement, the interpolation model by Chen and Sullivan extending Odijk to moderate confinement, and the Casassa theory describing the transition from moderate confinement to bulk. Further, this work establishes a robust, quantitative platform for understanding and manipulating biopolymers at the nanoscale, with key applications and insights toward emerging genomic analysis tools.

2.2 Introduction

Detailed understanding of the behavior of polymers under confinement has critical applications in the fields of nanotechnology, genomics, biophysics, and materials science. Particularly, direct manipulation and separation of biopolymers have contributed to the development of advanced nucleic-acid analytical technologies [34, 35] which integrate nanofluidics techniques such as extensional flow [36], physical confinement [37], and molecular combing [38].

Key to these efforts have been technical innovations in nanofluidic confining devices. Among them are nanochannels [39], nanopillar arrays [40], nanoslits [41], and staircase-like devices [42]. Experimental studies using these systems have generally employed long (\gg hundreds of persistence lengths) polymers. The high free-energy cost of confining such long polymers under the strongest-confinement regime, the Odijk regime [43], makes it challenging to make equilibrium measurements of this free energy without using indirect

techniques [44]. Direct measurements under this strong confinement require advances in populating highly confined geometries, which can be facilitated by using shorter polymers. Further, experiments with short polymers expand on prior verification of theoretical and simulation-based studies [32].

Historically, slit confinement of polymer molecules has been divided into three regimes: strong confinement, or the Odijk regime [43], moderate confinement, and weak confinement or the bulk [45]. These regimes are defined by comparing the polymer's unconfined radius of gyration, R_g , and Kuhn length, L_K , to the confining height h . The least-confined regime is the bulk regime, $h \gg 2R_g$, in which the polymer generally is not deformed from its free-solution conformation, except possibly when it comes close to a wall.

In the Odijk regime, $h \ll L_K$, and the polymer is stiff for distances on the order of the slit height. As a consequence, the polymer is unable to form random coils like it does in free solution, and its conformations are affected by *deflecting* stiff segments off of the walls (Fig. 2.1c, left). Odijk [31, 43] predicted that for cylindrical tube-like confinement, as opposed to slit-like confinement, the free energy of confinement, G_{conf} , in this regime scales as

$$\frac{G_{\text{conf}}(h)}{k_B T} \propto \frac{L_c}{L_K} \left(\frac{L_K}{h} \right)^{2/3}, \quad (2.1)$$

where h is the the diameter of the cylinder, k_B the Boltzmann constant, T the temperature, and L_c is the contour length of the polymer. The free energy of a polymer in a rectangular tube was later shown to be the sum of two terms, each identical to

Eq. 2.1, except with h replaced in either term by the length of one of the two sides of the rectangle [46] and with prefactors to the scaling relationship determined.

In the moderate-confinement regime ($L_K \ll h \ll 2R_g$), the polymer has enough room to bend back on itself in all three dimensions. Here, free energy is predicted [33, 47] to scale with slit height according to:

$$\frac{G_{\text{conf}}(h)}{k_B T} \propto \left(\frac{R_g}{h}\right)^2, \quad (2.2)$$

where we have assumed an ideal polymer since the effects of self-avoidance are weak for short chains [48].¹ This regime has a lower bound given by the structural scale L_K and an upper bound of $2R_g$, which is dependent on the length of the polymer. For semi-flexible chains that are short, the lack of sufficient separation between these length scales can lead to a regime that is too narrow to clearly give rise to the pure scaling (as opposed to the transitions).

In describing the behavior of polymers from extreme nanoconfinement to bulk regimes, we must therefore study two transition regions: i) h between Odijk ($h \ll L_K$) and moderate confinement ($h \gg L_K$), and ii) h between moderate confinement ($h < 2R_g$) and bulk ($h \gg 2R_g$). The first transition (which we will call the ‘‘CS transition’’) was studied by Chen and Sullivan [32], who calculated the transition from moderate-confinement to

¹Previous studies indicate that in this moderate-confinement regime, the free energy for finite chains will scale with the steric exclusion radius instead of the radius of gyration [49]. However, our concern here is the scaling with h as we do not vary the polymer size but rather the confinement dimensions.

Odijk regimes for an infinitely long polymer and proposed an empirical equation:

$$\frac{G_{\text{conf}}(h)}{k_B T} = \frac{\pi^2 L_c}{6 L_K} \frac{\left(\frac{L_K}{h}\right)^2}{\left[C_1 \left(\frac{L_K}{h}\right)^2 + C_2 \left(\frac{L_K}{h}\right) + 1\right]^{2/3}} \quad (2.3)$$

where $C_1 = 1.2865$ and $C_2 = 0.992$ [32]. Chen and Sullivan's result was later confirmed using a Monte Carlo method for long polymers [50].

For the second transition (which we will call the ‘‘Casassa transition’’), a prediction for the conformational cost of an ideal polymer between impenetrable plates was given by Casassa [45]. In free-energy terms, it can be expressed as

$$\frac{G_{\text{conf}}(h)}{k_B T} = -\ln \left[\frac{8}{\pi^2} \sum_{m=0}^{\infty} \frac{\exp\left(-\frac{(2m+1)^2 \pi^2}{4} \left(\frac{2R_g}{h}\right)^2\right)}{(2m+1)^2} \right] \quad (2.4)$$

which agrees with moderate confinement scaling of Eq. 2.2 in the $h/R_g \rightarrow 0$ limit. At large heights, a polymer will experience confinement only when it diffuses near the walls. This can be viewed as a narrow exclusion layer near the surfaces, which for hard spheres would equal their radii. As $h \rightarrow \infty$, this is a diminishing contribution which scales as $G_{\text{conf}}(h) \propto k_B T (R_g/h)$.

An outstanding challenge in the field of polymer physics has been to experimentally resolve the transitions between all of the above confinement regimes. Experimental measurements of spatially resolved polymers have observed a CS transition at $h \approx L_K$ in the scaling of polymers' in-plane radius of gyration, $R_{\parallel}(L_c)$, first in channel-like confinement [51] and later in slit-like confinement [52]. Theoretical studies assessing

whether this observed transition in the scaling of R_{\parallel} corresponds to the predicted transition in free-energy scaling have given less clear results [53–55]. One study [54] even suggests that the CS free-energy transition may not exist in slit-like confinement.

Testing this theory requires loading and observing the same polymer under a continuum of applied confinement. It is hard, however, to populate nanoscale imaging volumes where molecules are excluded by a large potential, especially while keeping polymers intact.

In the present experiments, we overcome this challenge by using dsDNA fragments of contour length $1047 \text{ nm} \approx 10L_K$. Polymers of this size sufficiently populate regions of low height for adequate statistics in more strongly confined regimes, while maintaining a sufficiently low bulk concentration for molecules to avoid interacting with each other.

In this article, we experimentally measure the transition between the bulk and moderate-confinement regimes and the crossover into the Odijk regime using a single-molecule imaging and manipulation platform called Convex Lens-induced Confinement (CLiC) [56, 57]. CLiC microscopy allows for a range of confinement heights from the nanoscale to the tens of microns to be probed simultaneously in one device. It loads molecules quickly, yet gently, into nanoscale environments, overcoming limitations of traditional side-loading nanofluidics [34].

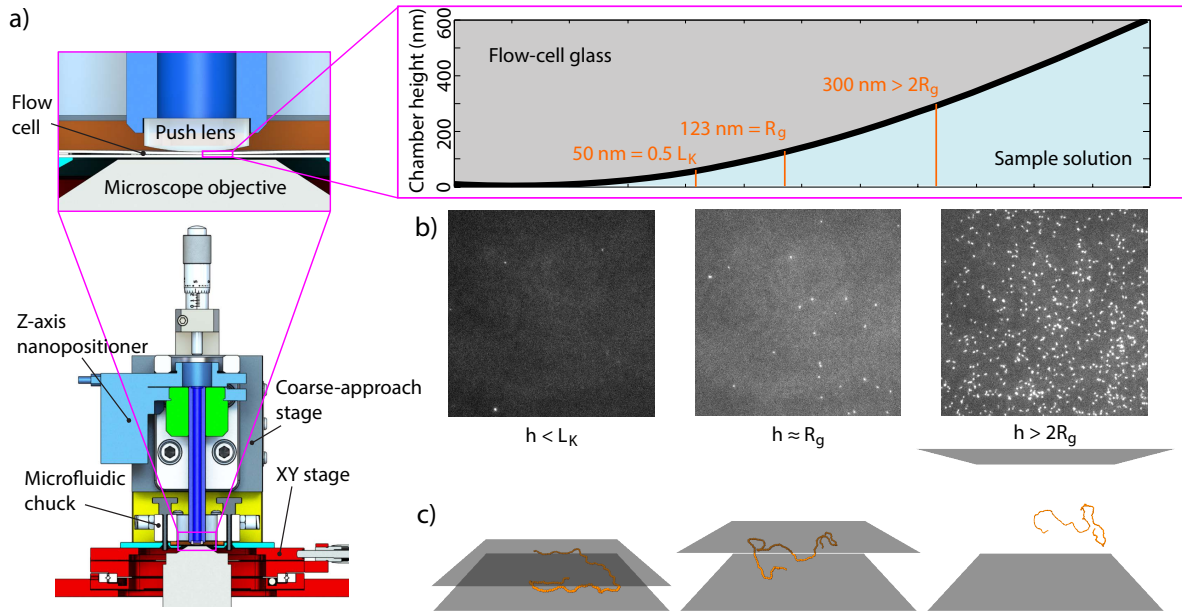


Figure 2.1: (a) Schematic of the CLiC imaging device: Includes an imaging flow cell, a “push lens” for forming the chamber, and a chuck with sample inlets for flowing in samples. It is mounted above the imaging objective. b): $91 \times 91 \text{ nm}^2$ micrographs of pUC19 dsDNA molecules with unconfined radius of gyration, $R_g = 123 \text{ nm}$, located at different points in the CLiC chamber. Left panel shows a chamber region with height $h < L_K$ (the Odijk regime); center panel shows a region centered roughly on $h = R_g$ (the moderate-confinement regime); right panel shows a region with $2R_g < h < 3R_g$ (transition between moderate-confinement and bulk regimes). c): Renderings of different polymer conformations in different regimes obtained by simulation. The three orange vertical lines in the chamber profile [a], upper right] indicate heights at which the three simulated polymers respectively are confined.

2.3 Experimental Section

The CLiC system (Fig. 2.1a) enables direct counting of individual DNA molecules in a chamber of tunable height profile and hence tunable particle concentration profile. The molecules are loaded into a flow cell, initially between $10\text{-}\mu\text{m}$ and $30\text{-}\mu\text{m}$ thick, which is compressed to make a curved chamber height profile of shallow curvature (see Supporting Information, SI). The height of the chamber can be essentially zero at the center (to within the surface roughness of the flow cell glass, $0.3 \sim 0.5 \text{ nm}$) and several

microns at the edges. This allows our molecules of $L_c = 1047$ nm having a free-solution size of $R_g = 123$ nm (using ideal worm-like chain theory, e.g. as in [58]) to quickly equilibrate among all regimes of confinement. CLiC microscopy produces a continuum of confinement heights without the need for micro- or nanofabrication, unlike devices with pillars [40] or staircases [42]. An earlier work of ours employed an additional mechanism, electrophoresis, to populate the most confined regions of the chamber for direct observation [59] and made measurements of DNA concentration away from equilibrium; the present work relies on no such mechanism and as such allows us to measure the free energy solely of *confinement*.²

To study DNA that is both under strong confinement and in equilibrium with DNA under weak confinement, we used linearized pUC19 plasmids labeled with the fluorescent stain YOYO-1. The YOYO-1-labeled DNA, along with dilute, spectrally disjunct Cy5 dye, used for a fluorescence intensity signal proportional to local chamber height, was flowed into a CLiC chamber and allowed to equilibrate for over an hour. This period was sufficient to establish equilibrium concentration profiles which were measured reproducibly as a function of chamber height (see SI). Data collection involved a sequence of raster scans over the chamber of the Cy5 fluorescence (SI Fig.

²The main advantages of the CLiC approach, for this work, are: 1) Top-loading [34] of molecules into the slit, which is efficient and gentle. That is, the molecules are positioned above their equilibrium positions, and then the confinement is applied. A static lithographic chamber would require molecules moving to their equilibrium positions from an unconfined reservoir into the nanoscale-confined staircase region, which is comparatively slow. CLiC combined with lithography would be redundant for this study; furthermore, the deformation of the lithographed-coverslip would still make h vary continuously throughout the chamber, which would be measured using the same methods. 2) Low cost and ease of experiments. We are able to perform many experiments in quick succession at low cost, using many molecules, since our set-up is not limited by custom micro/nano-fabrication of fragile components. By contributing a highly quantitative study using the CLiC approach, part of our intention is to validate its potential widespread dissemination as an enabling agent for further discovery e.g. of how polymers and molecules behave on the nanoscale.

A.1), labeled-DNA fluorescence (Fig. A.2), and interferometry (Fig. A.1), in that order.

To obtain accurate measurements of the chamber height, h , we mapped the chamber geometry by fitting Cy5 fluorescence intensity to a polynomial function subject to constraints imposed by interferometry of the chamber, building on our methods in Ref. [57] (see SI). We then binned the height map into areas of approximately equal height-ranges, forming annuli about the center of the chamber (SI Fig.A.1).

The DNA concentration profile as a function of local height was obtained using an ImageJ particle tracking plugin originally developed by Sbalzarini and Koumoutsakos [60], which we modified for this work (see SI). The trajectories were manually inspected to eliminate false particles and to include any missed particles. Particles were tracked for a duration of 2.5 seconds (50 frames at 50 ms exposure).

For a given bulk concentration, there is a limited range of heights where data can be taken. A practical lower limit is imposed at very small heights by the scarcity of DNA (first panel of Fig 2.1b), and an upper limit by particles being too dense to be reliably identified and tracked, or by exceeding the optical system's depth of field, resulting in particles diffusing in and out of focus. Since the CS and Casassa transitions for our experiments' R_g , L_K , and L_c span a large range of heights [32, 50], we performed experiments using several bulk concentrations in order to count particles at each height (Fig. 2.2a). The free-energy profile was constructed piece-wise using these datasets taken with overlapping observable height ranges and different bulk concentrations.

We divided our particle counts by the volume of the relevant annulus to find the resulting DNA concentration (Fig. 2.2b), where the local concentration $C(h)$ is normalized

by the bulk concentration C_{bulk} . Establishing the true C_{bulk} of a dataset is complicated by lack of an *in situ* measurement and is achieved with a best fit described in the SI. The true C_{bulk} is lower than the concentration of the injected sample due to a small fraction of molecules adhering to device surfaces and incomplete replacement of the wetting buffer (further details in SI).

2.4 Results and Discussion

2.4.1 Experimental Results

Figure 2.3 shows the confinement potential measured via CLiC as a function of confinement height h as well as the predicted values of G_{conf} from the Chen-Sullivan (Eq. 2.3) and Casassa (Eq. 2.4) theories. The confinement energy G_{conf} is calculated using the DNA concentrations and the Boltzmann distribution expression

$$\frac{G_{\text{conf}}}{k_{\text{B}}T} = -\ln\left(\frac{C(h)}{C_{\text{bulk}}}\right). \quad (2.5)$$

Using the CLiC setup, data has been acquired down to $h < L_{\text{K}}$. As can be seen, this is well into the crossover regime where the scaling transitions from $G_{\text{conf}} \sim h^{-2}$ in the moderate-confinement regime to $G_{\text{conf}} \sim h^{-2/3}$ in the Odijk regime. The experimental data follow the smooth, gradual change predicted by Chen-Sullivan, albeit with a discrepancy at very low h , representing a direct observation of the CS transition for slit-like confinement.

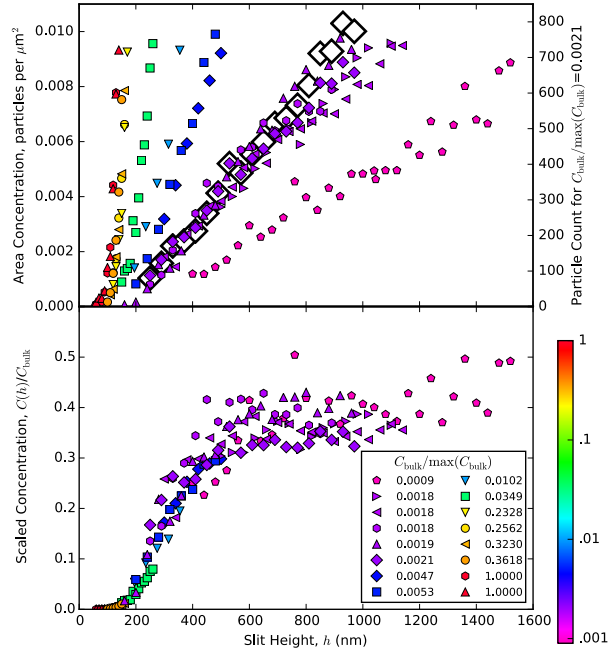


Figure 2.2: (top) Colored markers, left-hand axis: Areal concentration of particles in bins of height h . Open markers, right-hand axis: Total number of particles counted for a selected dataset. The bulk concentration, C_{bulk} , for the 16 different experiments, was varied to investigate a wide range of confinement heights. C_{bulk} reported as fraction of $\max(C_{\text{bulk}})$, 12.9 nM, determined for the highest-concentration experiments, described in SI. (bottom) Particle concentration $C(h)$ normalized by C_{bulk} .

2.4.2 Monte Carlo (MC) Simulations

We complement these experimental data with Monte Carlo simulations. An attempt is made to build a persistent random walk of ≈ 10 Kuhn segments (see SI for details). Any random walk that crosses the walls is rejected and the free energy can be calculated from the ratio between the number of allowed conformations to the number of attempts. The simulation results for G_{conf} are shown in the main plot of Fig. 2.3 (gray crosses). The results agree with the CS transition from Odijk to moderate confinement and then smoothly follow the Casassa transition into the bulk scaling of h^{-1} .

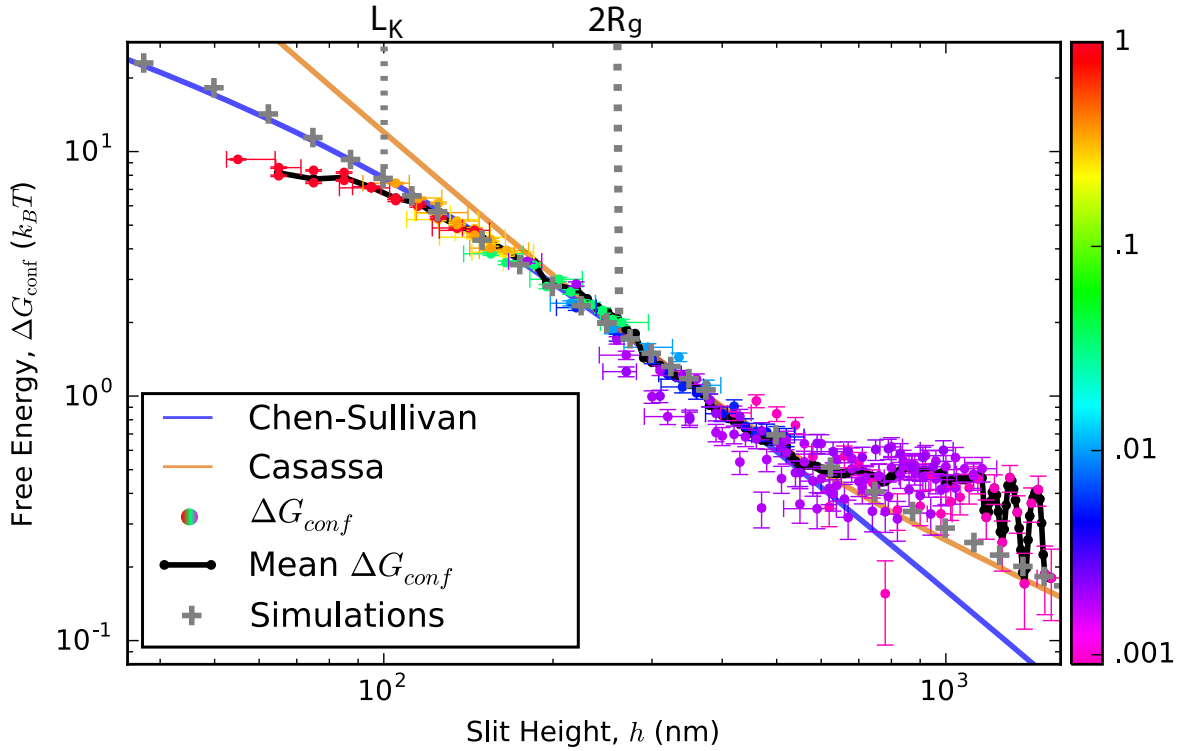


Figure 2.3: Confinement free energy for experiments, simulations, and CS and Casassa theories as a function of the slit height h . The Casassa line has been shifted down to meet the CS line to give a smooth crossover. Filled markers are experimental data coded as in Figure 2.2. Absolute concentrations were determined by a one-parameter fit of the combined datasets to a combined theory curve defined by the Chen-Sullivan (CS) curve at heights lower than the height at which the CS and Casassa curves coincide and by the Casassa curve at greater heights. Vertical error bars indicate the ranges of ΔG_{conf} corresponding to one standard deviation in the fit parameter (SI). Horizontal error bars indicate the range from the 25th to the 75th percentile of heights implied by the Cy5 fluorescence intensity within an annular height bin as defined by the polynomial chamber fit (see SI). For clarity, horizontal error bars are shown only for the lowest, highest, and central (rounded downward) height bins for each dataset. Gray crosses are simulation data. Vertical dotted lines mark regime boundaries L_K and $2R_g$.

Note that Eq. 2.4 is derived for a freely jointed chain while these simulations are performed with a semi-flexible chain which could modify the prefactor (see SM for details). Further, the Casassa result is derived for infinitely long chains and previous work has shown that finite chains can exhibit a different prefactor [49]. In any case, the data in Fig. 2.3 and Fig. 2.4 demonstrates that the difference is quite negligible and thus it is

ignored here. The agreement between the Chen-Sullivan theory, the CLiC data, and the simulations indicates that although Eq. 2.3 is derived for infinitely long chains, it is also remarkably accurate for chains such as pUC19 which comprise only 10 Kuhn lengths.

2.4.3 Langevin Dynamics (LD) Simulations

The Monte Carlo algorithm used in this work becomes very inefficient at tight confinement. Hence, we also performed Langevin dynamics (LD) simulations to explore the free energy of confinement at very small heights. In these simulation, we set the bead-size, σ , to be 5 nm which is on the order of the effective width of dsDNA. From this, the persistence length is set to 10σ and the polymer is composed of 183 beads to give a contour length corresponding to pUC19. The polymer is initialized between two walls and monomer-wall interactions are defined by standard coarse-grained potentials (see SM for details). The free energy of confinement is measured by recording the force exerted on the walls by the polymer at different slit heights. This data is then integrated to determine the free energy.

Fig. 2.4 displays the LD and MC data across a wide range of slit heights. Note that the LD and MC data overlap for a significant range of heights and are found to be in excellent agreement with each other. Further, the LD simulations go to very tight confinement where pure Odijk scaling (exponent of $-2/3$) is obtained. Conversely, the MC calculations extend to very large heights and the bulk confinement scaling of -1 is clearly recovered. The two numerical approaches overlap in the moderate confinement regime. Although the range is quite small for this particular polymer model, a steeper

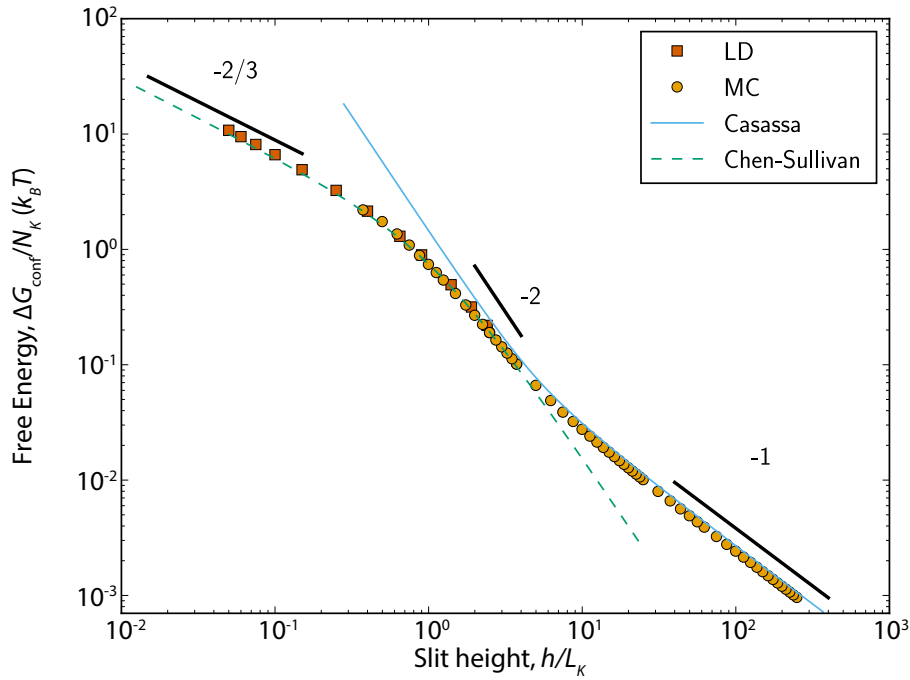


Figure 2.4: ΔG_{conf} per number of Kuhn lengths N_K , versus slit height per Kuhn length, h/L_K , as obtained by the Monte Carlo (circles) and Langevin Dynamics (squares) simulations. The three scalings of $-2/3$, -2 and -1 as well as all transitions between them are obtained for the pUC19 polymer model.

scaling of around -2 is apparent from both approaches. The Chen-Sullivan and Casassa transitions are also plotted in Fig. 4 and the agreement between both calculations and these expressions is excellent. The combination of these two simulation approaches for the free energy of confinement for a semi-flexible polymer thus starts in the pure scaling Odijk scaling of tight confinement, follows the Chen-Sullivan transition to moderate confinement and finally transitions to bulk scaling in accordance with the Casassa formulation. To the best of our knowledge, this represents the first time that this complete mapping of $\Delta G(h)$ has been performed.

2.4.4 Discussion

Returning to the experimental data shown in the main plot of Fig. 2.3, the points at the lowest h values lie in the CS transition where $h \lesssim L_K$ (and thus not $h \ll L_K$). For $h > L_K$, the data is transitioning from a scaling close to Odijk ($G_{\text{conf}} \sim h^{-2/3}$) towards moderate-confinement scaling ($G_{\text{conf}} \sim h^{-2}$). As pure moderate-confinement behavior is not expected until $h \gg L_K$, the CS transition is quite broad with a gradual approach to h^{-2} scaling. While we observe a shallower slope in the dependence of G_{conf} on h at $h < L_K$ than predicted by Chen and Sullivan, we cannot conclude that the Chen-Sullivan prediction is in error, as experimental uncertainty and artifacts may be significant enough to explain the discrepancy.

The difference between experimentally measured G_{conf} and simulated and theoretical G_{conf} at very low h ($< L_K$) may owe to a combination of (1) chamber characterization being less accurate near the point of contact between the two surfaces of the CLiC chamber (see SI); (2) statistical error in the small number of particles counted at very low heights; and (3) attraction of DNA to the glass surface, which would be the most significant at chamber locations with high surface-to-volume ratios. The wall attraction effects are likely contributors, as the attraction would result in the observed decrease in free energy. Additionally recent molecular simulations have shown weak DNA-silica attraction despite the electrostatic repulsion between negative silanolate moieties and the backbone phosphates and in the absence of chaotropic salts [61]. Moreover, the DNA in our experiments is likely to be attracted still more to the glass surface, as

YOYO-1 is positively charged. These factors would also explain why the simulations agree with CS but not with experiments, as experimental error in height determination, greater statistical error at low h , and surface effects are not included in the simulation model. Surface interactions beyond excluded-volume repulsion have received little attention from theorists working under an Odijk-theory paradigm, although our results suggest that they may be important in experiments taking place in the Odijk regime or the transition from moderate confinement thereto. Future research could incorporate results from size-exclusion chromatography theory that does consider these interactions (*e.g.*, Ref. [62, 63]) and might bring simulations and a modified Chen-Sullivan theory into closer agreement with our experimental results.

Because for pUC19, $2R_g$ is little larger than L_K , the range of h in which pure, non-transitional moderate-confinement behavior is observed is small. This moderate-confinement window is defined by the range of h in which both CS and Casassa theory show approximately h^{-2} scaling, roughly $2R_g < h < 4R_g$. Above this window, the free energy is expected to depart the CS curve and approach the $G_{\text{conf}} \sim h^{-1}$ scaling predicted by Casassa in the limit of very large h . Indeed, our data depart the CS curve at a height predicted by Casassa, roughly $4R_g$. To the best of our knowledge, this result represents the first experimental and simulation test of the predicted Casassa transition to bulk for a semi-flexible polymer.

We note that the measured free energy slope appears slightly shallower than the theoretical slope at large h . However, one cannot infer from our data that the Casassa theory is incorrect.. The deviation is likely due to biases associated with two kinds

of systematic experimental errors present for large heights. First, the free energy of confinement in log-space is especially sensitive to the bulk pUC19 concentration, which depends on a one-parameter fit of the combined datasets (see SI). Indeed, the larger error bars in the free energy at large h reflect reduced confidence in the fitted value of G_{conf} at large h (Fig. 2.3). Further, particles can be identified and tracked only if they stay reasonably within the depth of field of our optical system: at higher h , it is increasingly possible for particles to make excursions out of this range, allowing for small fractions of their trajectories to be lost, and thus G_{conf} overestimated (SI).

2.5 Conclusion

This work has contributed new measurements of the free energy of confinement for semi-flexible polymers in a slit-like geometry across a wide range of slit heights, by counting DNA molecules within a CLiC chamber. The experimental results and Monte Carlo simulations connect confinement regimes described by different theories, including the theories of Odijk (strong), Chen and Sullivan (strong-to-moderate), and Casassa (moderate-to-bulk). This comprehensive validation indicates that Eqs. 2.3 and 2.4 provide accurate and versatile predictions even beyond the polymer length-scales for which the Chen-Sullivan model was derived. The experimental and simulation results, methods, and instrumentation delivered by this paper provide crucial information for modeling and understanding the behavior of polymers in a range of nanofluidic devices, and facilitate efficient loading of and control over biopolymer samples within

next-generation nanotechnology devices.

Preface to Chapter 3

In chapter 2, we combine CLiC with fluorescent microscopy to study the behavior of relatively long biopolymers under confinement. Our results have potential applications in genomics as well as in the design and delivery of nucleic acid drugs. One of the most promising drug delivery techniques for genetic medicine is Lipid nanoparticles (LNPs), which were introduced in Chapter 1. In this chapter we combine CLiC fluorescent microscopy with microfabrication, as well as simulation and analysis tools, to directly probe size and loading of LNPs with small interfering RNA (siRNA) molecules. These molecules are quite small; however, the nanoparticles have been shown to successfully load and deliver longer mRNA and plasmid DNA molecules, similar to those studied in chapter 2. In the results section we correlate the size and loading distributions to extract structural information of the LNPs. Additionally, we measure the drug loading distributions with single molecule resolution.

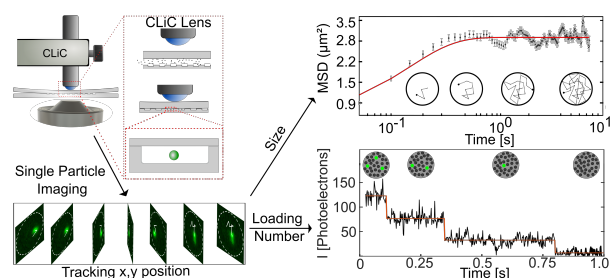
Chapter 3

Single-particle Measurements of Size and Loading of Drug-delivery Lipid Nanoparticles

This section is based on a manuscript in review: Kamanzi, A., Gu, Y., Tahvildari, R., Friedenberger, Z., Xu, R., Berti, R., Kurylowicz, M., Witzigmann, D., Kulkarni, J.A., Leung, J., Andersson, J., Dahlin, A., Hook, F., Sutton, M., Cullis, P.R., Leslie S.R., 2021. Simultaneous, single-particle measurements of size and loading give new insights into the structure of drug-delivery nanoparticles

3.1 Abstract

Nanoparticles are a promising solution for delivery of a wide range of medicines and vaccines. Optimizing their design depends on being able to resolve, understand, and predict biophysical and therapeutic



properties, as a function of design parameters. While existing tools have made great

progress, gaps in understanding remain because of the inability to make detailed measurements of multiple correlated properties. Typically, an average measurement is made across a heterogeneous population, obscuring potentially important information. In this work, we develop and apply a new method for characterizing nanoparticles with single-particle resolution. We use CLiC (Convex Lens-induced Confinement) microscopy to isolate and quantify the diffusive trajectories and fluorescent intensities of individual nanoparticles trapped in microwells for long times. First, we benchmark detailed measurements of fluorescent polystyrene nanoparticles against prior data, to validate our approach. Second, we apply our method to investigate the size and loading properties of lipid nanoparticle (LNP) vehicles containing silencing RNA (siRNA), as a function of lipid formulation, solution pH, and drug-loading. By taking a comprehensive look at the correlation between the intensity and size measurements, we gain new insights into LNP structure and how the siRNA is distributed in the LNP. Beyond introducing a new analytic for size and loading, this work opens the door to new studies of dynamics with single-particle resolution, such as LNP fusion and drug-release kinetics. The prime contribution of this work is to better understand the connections between microscopic and macroscopic properties of drug-delivery vehicles, enabling and accelerating their discovery and development.

3.2 Introduction

Nanocarriers and nanoparticles are increasingly used in medicine as vehicles for functional cargo. Broadly speaking these vehicles include micelles, liposomes, nanoemulsions, as well as lipid, polymeric and dendritic nanoparticles, which exhibit a variety of useful properties including biopersistence, targeting, enhanced cellular penetration, stimuli-sensitivity and direct carrier visualization. [64]. Lipid-based nanoparticles (LNPs) [65] have been developed to deliver a rapidly growing class of genetic medicines [66–68], including silencing RNAs (siRNAs), messenger RNAs (mRNAs) and other biologics, with growing importance. LNPs aid delivery of these molecules by preventing degradation in biological fluids [66], improving transit across cell membranes, and providing targeted and concentrated delivery [67]. Furthermore, LNPs exhibit a number of desirable characteristics, such as ease of manufacture, lack of immune response, high carrying capacity, and can be dosed repeatedly [9].

LNPs made from ionizable cationic lipids have been successful as delivery vehicles for mRNA vaccines [69], including Covid-19 vaccines [2,3]. It has also been shown that LNPs may effectively deliver large mRNA-based drugs in the context of gene therapy [3,70].

The ionizable cationic lipids are especially suited for these applications, as their properties have been tuned to have several advantages, including: increased loading efficiency during their formation [15] as a result of lipid-drug charge interactions, which simultaneously promotes the self-assembly of the nanoparticles; reduced toxicity during transport, as a result of lowered surface charge of the nanoparticles [8]; and optimized

drug delivery following endocytosis to the target cells [15]. Additionally, ionizable lipids are generally found to be non-immunogenic, non-oncogenic, and have minimal cytotoxicity compared to other delivery vectors [71]. Optimizing their formulation parameters involves tuning the acid dissociation constants (pK_a) of the ionizable cationic lipids to values in the range of 6.2-6.7 [15].

Despite the promise of LNPs as drug-delivery vehicles, there are significant challenges to overcome in their optimization, especially with regard to efficiency of delivery and uptake in cells. A broad range of methods are available for characterizing nanoparticles, including dynamic light scattering (DLS), nanoparticle tracking analysis (NTA), atomic force microscopy (AFM), cryo-electron microscopy (Cryo-TEM), flow cytometry (FCM), and resistive pulse sensing (RPS). These techniques have provided valuable insights into the physical characteristics of nanoparticle samples, but since microscopic properties of the LNPs, including particle size, structure, cargo-loading, and surface chemistry, are often heterogeneous [69]. Each of these methods has limitations (See Table B.1) and leave important gaps even when used in combination. The available techniques are either bulk measurements and lack single-particle resolution (DLS, FCM), or have single-particle resolution for very short times (NTA, RPS), or require surface immobilization to achieve longer times (AFM, Cryo-TEM) which can bias results by altering particle structure. What is missing, and what this work addresses, is a platform for tether-free, single-particle measurements with sufficiently long per-particle observation times in cell-like conditions; as well as the capacity to change conditions and image the response.

In this work, we introduce a multi-parametric nanoparticle imaging platform capable

of imaging many individually confined nanoparticles which are diffusing in controlled solution conditions. This platform uses the CLiC microscopy technique [56, 72, 73] which has been applied to study confined DNA and polymers [1, 34, 74], DNA plasmids [75, 76] and proteins [77], as well as their responses to changes in solution conditions.

Integral to this platform, we develop simulations of model data crucial for obtaining precise and accurate measurements and analysis. These analysis tools inform a dynamic “feedback loop” which optimizes the selection of parameters for data acquisition and analysis, customized for a given molecular sample, in order to minimize the statistical and systematic error in the size and loading measurements. To inform this platform, we develop a robust theoretical treatment of the effect of micro/nano-scale confinement on the imaged diffusivity of the nanoparticles in the CLiC device and take these effects into account in interpreting nanoparticle size (See Figure B.1 and Table B.2, as well as the corresponding section in Appendix B).

To establish and validate our multiparametric platform we first study polystyrene nanoparticles of known size, measuring their diffusivity and size distributions under a range of confinement conditions. We then use this platform to investigate more complex biological samples of lipid nanoparticles (LNPs) with less-understood size and loading characteristics. Here, we investigate changes in (non-loaded) LNP structures as a function of pH and ionizable lipid composition and take a detailed look at how LNP size and structure change once the LNPs are loaded with siRNA. Significantly, the ability to simultaneously measure both size and siRNA-loading of individual LNPs enables a scaling analysis which reveals the spatial distribution of siRNA cargo within the LNP. The ability

to measure size and loading simultaneously, as well as the dynamic changes of these variables at the single-particle level is important for designing multi-functional LNPs for drug delivery. Our method can be developed further to imaging LNP dynamics at the interface of and inside cells.

3.3 Results

3.3.1 Validation of single-particle diffusivity and size analytic measurement using 48nm diameter polystyrene nanoparticles

We demonstrate the sizing and simulation components of our method using measurements of carboxylate-modified microspheres composed of polystyrene, from ThermoFisher [78]. Figure 3.1 shows the flow of experimental and analytic steps which transform a sequence of CLiC images of diffusing nanoparticles into a distribution of individually measured diffusivities and sizes.

Figure 3.1A shows a schematic of the Convex Lens-induced Confinement (CLiC) imaging device, which holds a flow-cell containing embedded microwells, and is mounted on an inverted microscope. A suspension of nanoparticles is introduced in the flow-cell using a microfluidic chuck. The CLiC lens is controlled by a nanopositioner, deflecting the top of the flow cell downwards to confine the suspension within the array of microwells. The seal formed between the glass surfaces excludes out-of-focus material

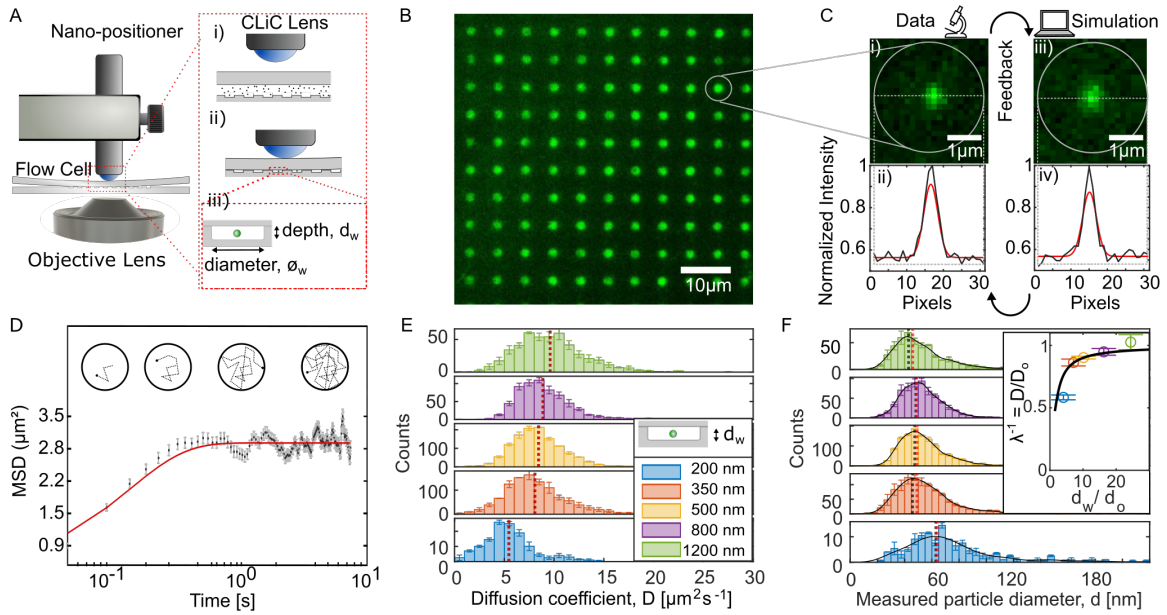


Figure 3.1: CLiC nanoparticle characterization assay. (A) Schematic of the CLiC instrument and cross section of a flow cell. (i) The curved CLiC lens deflects the top surface downward (ii) and traps sample in the microwells embedded in the bottom surface of the flow cell (iii). (B) Image of fluorescently labeled, 24-nm radius polystyrene particles in an array of 3 μm microwells. (C) A close-up image of a single NP inside a 3 μm microwell, with cross section and fitting curve inset, and comparison to simulations. Microscopy data is shown on the left (i) and (ii), and was obtained under 100x magnification with 160 nm/pixel resolution. Simulation data is shown on the right (iii) (iv). (D) Particle tracking is used to construct the confined-Mean Square Displacement (MSD) curve for each LNP, described in Methods and SI. Confined particle diffusion is shown over time, illustrating that the shoulder in the MSD curve relates to the finite area of the microwell. (E) Individual NP diffusivities are extracted from fitting each curve in (D) and compiled into a distribution for the measured population. Diffusivity distributions are measured for NPs confined in microwells with 200, 350, 500, 800 and 1200 nm depths and 10 μm diameter. The distributions in (E) and (F) represent averaged measurements from at least 2 to 3 experiments, where each bar plot was obtained by averaging bins of the corresponding histograms. (F) To account for hydrodynamic effects at the walls of the microwell, we use a modified Stokes-Einstein equation described by Eq. 2 to correct for confinement geometry. This collapses the different diffusivity distributions onto a single size distribution, exception for the case of 200 nm depth. The size of the particle is obtained by fitting the measured diffusion coefficient values to a theoretical model (Eq. 3.3) as shown in (F insert), and was found to be 49 ± 6 nm. All the dashed lines are summarized in Table B.2 of Appendix B

which enables sensitive detection of single diffusing nanoparticles.

Figure 3.1B shows a series of fluorescence images of nanoparticles trapped in an array of about 100 microwells (3 μm diameter and 500 nm depth) in an $82 \mu\text{m} \times 82 \mu\text{m}$ field

of view. The concentration of nanoparticles is approximately 1 nM, which results in trapping an average of one nanoparticle per well and is convenient for analysis. Serial measurements are made by raising and lowering the CLiC lens and replenishing the array of wells with fresh nanoparticles, so that thousands of single particle trajectories can be obtained in a relatively short time (i.e. 1 - 3 hrs with the current implementation). In this way, the CLiC method provides sensitive, single-particle measurements with good statistics, and a number of advantages including: being able to replenish the sample in an array of wells using the CLiC actuator, tune the sample concentration so there is one particle per well on average, and use information from other wells to improve the analysis (i.e. empty wells to establish the local background, and excluding wells with stuck or aggregated molecules such that calculations are performed exclusively on freely diffusing particles).

Figure 3.1C shows an image of a single microwell, in which a single particle is a diffraction-limited spot. Its trajectory (x, y position) is recorded over the course of many sequential images using particle-tracking software (see SI: – ‘Particle detection, tracking and sizing’ for details). Imaging and experimental parameters include exposure time per frame, number of frames, laser intensity, dimension and number of wells per field of view, sample concentration and number of trajectories per data set.

The selection of these parameters is informed by an iterative process which generates simulations of diffusing nanoparticles under confinement, using these input parameters; analyzes the simulated data to assess the statistical and systematic error on the output size and intensity measurements; and iterates on these parameters to reduce these errors

to be below an acceptable bound (see Methods and SI:– ‘Simulation of confined particles’).

The Mean Square Displacement (MSD) curve is constructed for each particle trajectory (Figure 3.1D). The diffusion coefficient for every particle is determined by fitting this curve to the analytical expression derived for the MSD under the confined conditions [79, 80] (see Methods and SI – ‘Simulation of confined particles’). Figure 3.1E shows the distribution of measured diffusion coefficients for the sampled population under a range of confinement depths. The measured diffusivity is lower for the same nanoparticles under more constrained conditions due to hydrodynamic effects near confining surfaces [81–83]. For these measurements this effect is less than 15% for wells with heights between 200 nm and 1200 nm and fixed diameter of 10 μm , as shown in the inset of Figure 3.1 F.

To convert diffusivity to size distributions we use a modified Stokes-Einstein relation which includes a correction for the hydrodynamic effects near surfaces (see Methods). [81–83] We obtain the correction factor (λ) – for each confinement depth – by fitting the diffusion coefficients to a theoretical model given by Eq. 3.3. After this correction, we observe the diffusivity distributions acquired under different confinement conditions to converge to the same size distribution (Figure 3.1F), with a peak at 49 +/- 6 nm diameter in agreement with the manufacturer’s specifications. This validates our nano characterization method for particle size, including the necessary simulation and theoretical tools to account for confined diffusion of hard spheres near surfaces.

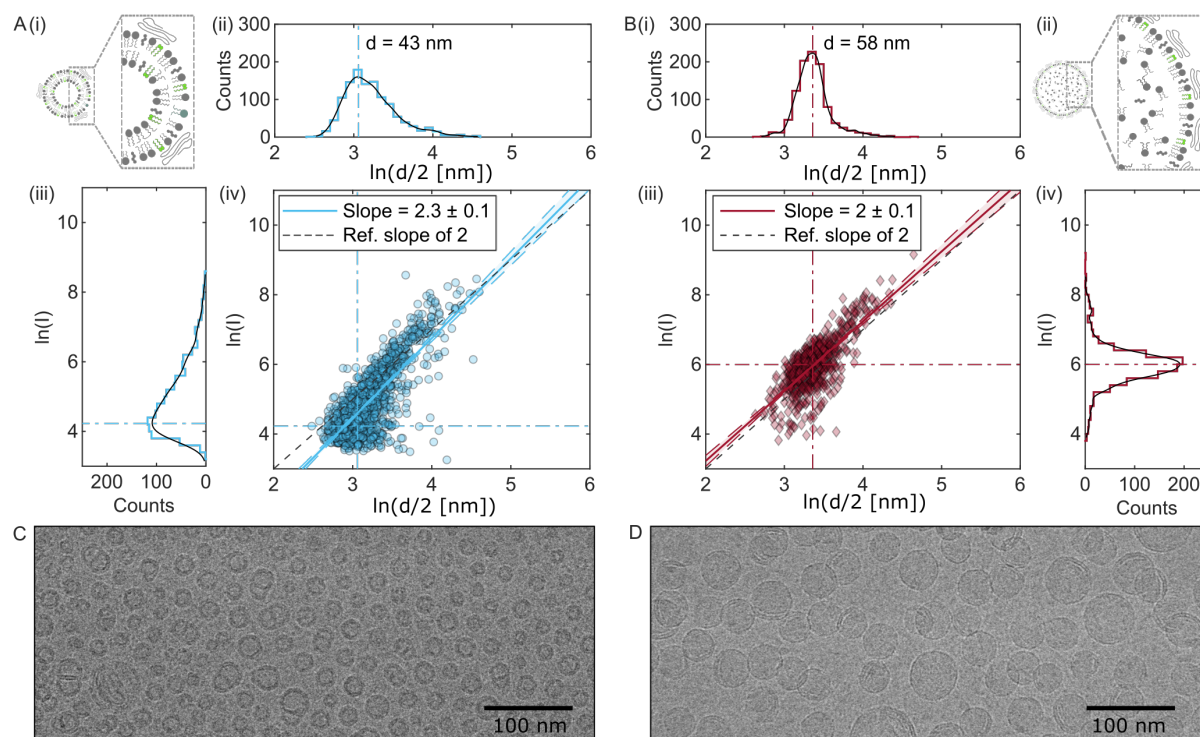


Figure 3.2: LNP structural modifications as a function of pH. Measurements of LNPs in pH4/pH7.4 buffer conditions (25mM NaOAc)/(1xPBS) are shown in blue/red (A/B). Size (A (ii), B (i)) and fluorescence intensity (A(iii), B(iv)) distributions for LNP populations at pH 4 and pH7.4, respectively, are projected onto a log-log scatter plot (A(iv), B(iii)). Counts refers to number of particles. Linear fits to the correlated data indicate the scaling of intensity with radius. The scaling coefficient gives information about the expected distribution of fluorophores within the LNP structure. For example, if intensity scales as radius raised to the power of two (or three), the fluorophores would reside on the surface (or in the volume). Schematics of the LNP structures and spatial distribution of fluorophores is shown in A(i) and B(ii) respectively [reproduced based on schematics in Kulkarni et. al. [84]]. Corresponding Cryo-TEM images of the LNPs are shown in C (pH4) and D (pH7.4). For LNPs formed in the pH7.4 solution, the fluorophores are expected to be excluded from the LNP volume and be present only on outermost surface of the LNP. This is consistent with the observed scaling between intensity and radius raised to the power of two (shown in red). For LNPs formed in the pH4 solution, bilayer structures are expected in which the fluorophores can be integrated, which may correspond to a layer around 5 to 6 nm thick based on prior work. This is consistent with the observed scaling coefficient between two and three (shown in blue), when the log-log scatter plot is fit over a large range of radii.

3.3.2 Probing structural transition in unloaded LNPs, induced by changing buffer conditions (pH)

We apply our single-molecule methodology to investigate the impact of buffer pH on the biophysical properties of LNPs. For this, we use the LNP formulation based on

OnpattroTM (patisiran), the first FDA approved LNP-based drug. The LNPs are composed of ionizable lipid 2,2-dilinoleyl-4-(2-dimethylaminoethyl)[1,3]-dioxolane [8] (DLin-KC2-DMA or KC2), cholesterol (Chol), as well as two structural lipids: distearoylphosphatidylcholine (DSPC) and PEG-lipid (DSPE-PEG2000). We produce nanoparticles at pH4 using an established rapid mixing method, described in Refs. [9, 84, 85], at a mixing ratio of KC2/Chol/DSPC/PEG-lipid (50/39/10/1 mol% respectively). We then generate nanoparticles at pH7.4, by taking the above LNPs suspended in the pH4 sodium acetate buffer (25mM NaOAc), and dialyzing them into a pH7.4 phosphate-buffered saline solution (1x PBS). This induces a fusion process that results in the formation of a different nanoparticle structure [86].

Figure 3.2 illustrates a previously proposed change in particle structure from a small bilayer LNP at pH4 (Figure 3.2A(i)) to a larger particle with an oil droplet core surrounded by a lipid monolayer shell at pH7.4, with Cryo-TEM measurements [84, 87] (Figure 3.2B(i)). The structural transitions and LNP formation process are driven by neutralization of the ionizable lipids and is thought to be essential to the complete formation of LNP systems. The pKa of the ionizable lipids (6.7 for KC2) has been tuned to optimize the LNPs' entrapment of nucleic acid loads, as well as their intracellular delivery [3, 66].

For our single-particle fluorescence imaging experiments, we label nanoparticles with lipophilic fluorescent dyes DiI-C18, a dialkylcarbocyanine derivative commonly known as DiI, at a labeling ratio of 1%. This allows us to simultaneously measure the spatial trajectory and fluorescence intensity of individual LNPs. DiI has a polar structure with a

hydrophilic headgroup attached to hydrophobic tail chains, which are expected to insert into the LNP surface membrane. Our measurements use approximately 26 dyes per LNP, inserted so as to randomly sample the outer surface.

By compiling many single-particle measurements, we establish the distributions of size and intensity for the LNP population, as shown in Figures 3.2A(ii), 3.2A(iii), 3.2B(i) and 3.2B(iv). The size distributions are the result of a full diffusivity analysis as described above, including corrections for confinement (details shown in Table B.2 of Appendix B). Our results show increase in both particle size and intensity distributions as a function of increased pH. The size distribution probes important properties of the nanoparticles, such as monodispersity which is hypothesized to help with cell-uptake once the particle-size is optimized, and self-affinity or tendency for aggregation which may lower therapeutic effectiveness.

Figures 3.2A(iv) and 3.2B(iii) show scatter plots combining both of these distributions, where each point represents the size and intensity of a single LNP. By fitting log-log plots with linear regression, we obtain a slope of 2.01 ± 0.06 for LNPs at pH7.4 and a significantly higher slope 2.29 ± 0.05 for LNPs at pH4. The corresponding R-squared values for the fitting are 0.54 and 0.60 respectively, and the p-values for the fitting, with t-statistic null hypothesis testing, are both $\ll 0.05$. Hence the linear regressions are good representations for the data. The results at pH7.4 are consistent with fluorescent dyes inserted into the surface of the LNPs, resulting in particle brightness that scales as particle radius squared (Figure 3.2B(ii)). On the other hand, the higher scaling slope observed at pH4 is consistent with the dye distribution being partially on the outer surface as well

as in the volume of the LNP (i.e. inner surface of bilayer). This can be explained by the presence of DiI molecules on the inner surface of the bilayer membrane structure of the (smaller) nanoparticles, as show in the schematic of 3.2A(i).

Our measurements are sensitive to the available lipid-aqueous interface per LNP, and as a result we can use DiI labels to directly extract structural information for the nanoparticles.

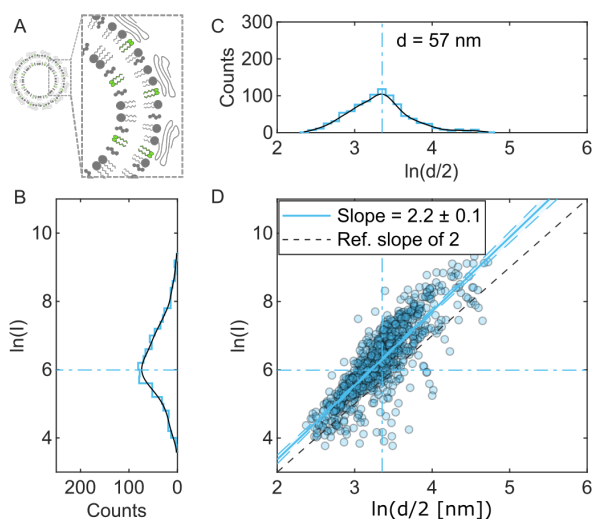


Figure 3.3: Control Lipid nanoparticles: Measurements on unloaded neutral LNP, with no ionizable lipids in their formulation. (A) Schematic of the neutral LNPs, showing a bilayer structure as well as a layer of the PEG brushes. Size (B) and fluorescence intensity (c) distributions for the LNP are projected onto a log-log scatter plot (D). Counts refers to number of particles. A linear fit to the correlated data indicate the scaling of intensity with radius. The fitting was performed using MatLab’s linear regression model and resulted in an Rsquared value of 0.768. Similar to the pH4 ionizable LNP samples in the main paper, the fluorophores are able to reside on both surfaces of the bilayer, hence resulting a radius-intensity scaling greater than 2.

3.3.3 Control measurements: Bilayer LNPs without ionizable lipids, in pH7.4 buffer

To further validate our measurements, we use the same approach to measure the size and fluorescent dye loading of nanoparticles with no ionizable lipids in their composition, as a control sample with no additional complexity arising from charge or ionization effects. These LNPs have no drug encapsulated, and were formulated as described in Methods using Chol/DSPC/PEG-lipid compositions at a mixing ratio of (39/56/5 mol % respectively), where the structural lipid components are increased to replace the KC2 component. In this case the nanoparticles are known to maintain their bilayer structure in both buffer conditions.

Figures 3.3B and C show the fluorescence intensity and size distributions for the control LNPs in pH7.4 buffer conditions. In Figure 3.3D these distributions are projected onto a log-log scatter plot. Again, a linear regression fit to the data is used to measure the scaling of fluorescence intensity with particle size. In this case the scaling exponent is 2.17 ± 0.05 , indicative of fluorophores partially filling the volume of the sphere. The corresponding R-squared values for the fitting is 0.70, and the p-value for the fitting, with t-statistic null hypothesis testing, is $\ll 0.05$ and validates the linear regression.

The difference in the scaling coefficients for the two bilayer LNPs (Figures 2A and 3) can be explained by the difference in relative size of the bilayer thickness (e.g. 5 – 6 nm) with respect to radius of the particle (e.g. 20 nm to 30 nm). For smaller particles, the relative volumetric contribution of dyes in the bilayer can be more significant, since

the finite bilayer thickness occupies more of the sample volume, which means that the observed scaling coefficient will be greater than two. By contrast, for larger particles and with a smaller relative bilayer thickness, the scaling of the intensity with radius will more closely approach a power of two.

Additional t-statistic hypothesis testing was performed to compare the 3 different measurements for linear regression slopes. The corresponding p-values obtained were all below 0.03 (3.2×10^{-7} for pH4 vs pH7.4 samples, 6.6×10^{-4} for pH7.4 vs control samples, and 0.03 for pH4 vs control sample). Hence the differences are significant with 97% confidence or more.

3.3.4 Quantification of siRNA drug-loading with single-molecule resolution

To study cargo loading of the nanoparticles, we again use LNPs with a formulation based on that of the OnpattroTM (patisiran) drug. In this case the nanoparticles were loaded with siRNA molecules chosen to achieve amino lipid nitrogen-to-siRNA phosphate (N/P) charge ratio of 3. This formulation is expected to result in the loading of hundreds of siRNA molecules per LNP, as estimated from the mixing ratios. For these, fluorescent dyes Ty563 were covalently bonded to the siRNA molecule, and the labeling fraction was varied for different experiments.

To analyze siRNA loading in the lipid nanoparticles, we use two complementary methods. The first is a photobleaching analysis (Figures 3.4 and 3.5), where the number of fluorophores is counted using the number of photobleaching steps. To optimally

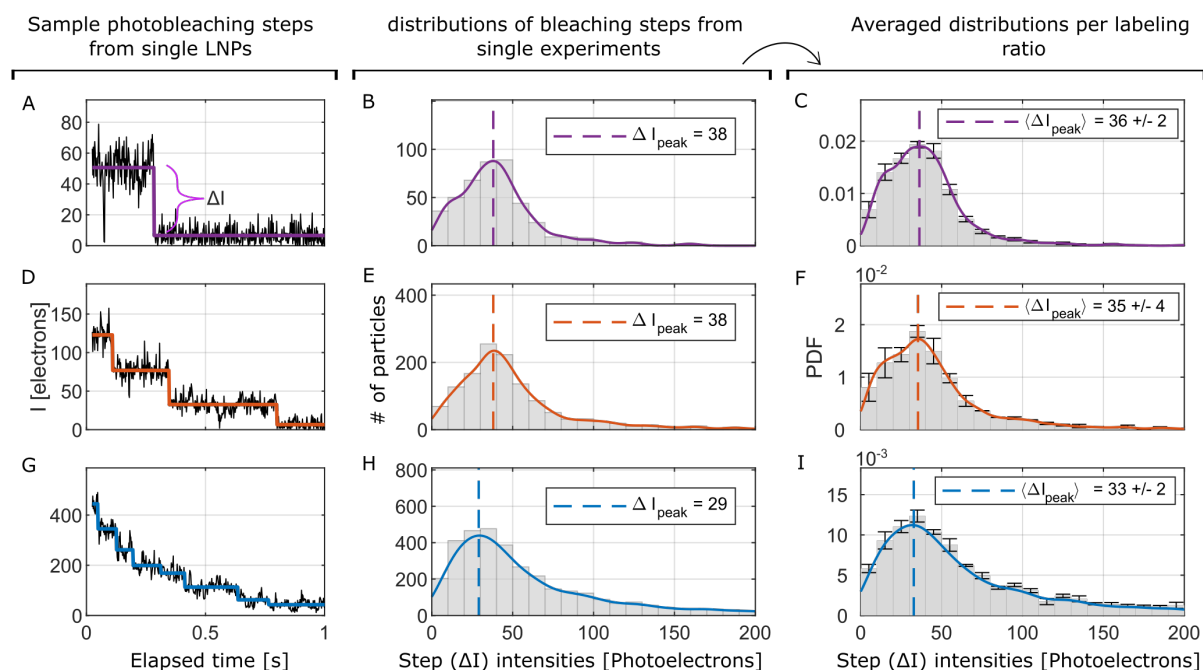


Figure 3.4: Photobleaching analysis of siRNA-loaded LNPs to measure single dye intensities. Left column: (A), (D) (G) show sample intensity traces - with discrete photobleaching steps - for samples labeled with 1, 3 and 10 fluorophores per LNP respectively. Middle column: (B), (E) (H) show Step-size distributions - from single experiments - with kernel density fits to obtain maximum likelihood step intensity. Right Column: (C), (F) (I) show averaged step intensity distributions for the 3 different samples. The bar chart is obtained by averaging corresponding histogram bins, to obtain a mean distribution, with error bars. The dashed lines represent average of peak intensities from different experiments, and lines up nicely with a fitted kernel density.

resolve consecutive bleaching events of individual fluorophores, this requires high signal-to-noise per fluorophore with short exposure times (low fluorophore loading and high laser intensity).

The second method uses the particle-tracking size and intensity analysis described above. This benefits from high fluorophore loading and low laser power to obtain long single-particle trajectories, in order to improve the signal-to-noise of the measurements of diffusivity and size (Figure 3.6). Applying both methods to characterize a given LNP-drug construct gives consistent results.

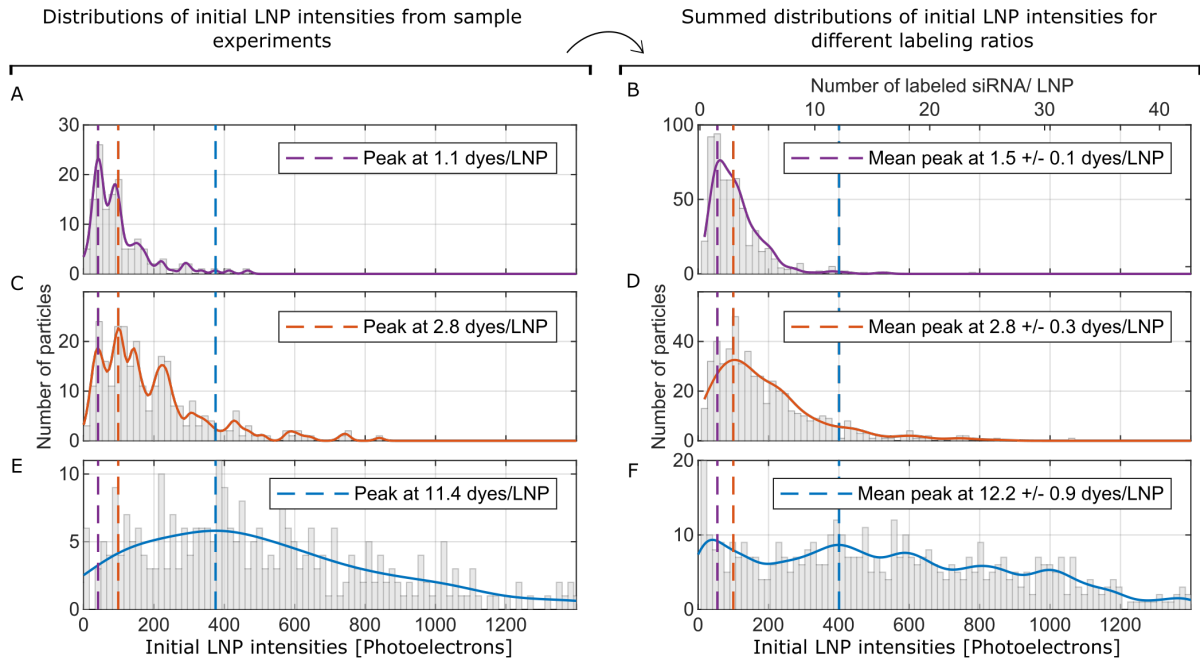


Figure 3.5: LNP drug loading (siRNA) measurements with single-molecule resolution. Left column: (A), (C) and (E) show distributions of initial particle intensities - before photobleaching - from sample experiments. Kernel density fits to the data are used to obtain peak intensities. Right Column: (B), (D) and (F) show the pooled distributions of the initial intensities. The dashed lines represent average of peak intensities from different experiments, which line up well with kernel density fits to the data.

Three representative intensity traces are shown in Figures 3.4(A), (D) and (G), in which single LNPs undergo stepwise photobleaching. The solid colored lines show fitting for the mean of the discrete intensity levels. The fitting is performed with the photobleaching detection algorithm reported by Chen et al. [88], which uses the two-sample t-test to determine the discrete plateau regions in the intensity traces. Each intensity step corresponds to a single photobleaching event. An example of a fitted step is indicated by ΔI in Figure 3.4(A). Distributions of step sizes - from individual experiments - are shown in Figures 3.4(B), (E) and (H), for each of the 3 labeling ratios. The colored lines show fitting with a kernel density estimation for the maximum likelihood step intensity,

as described in Methods below. The fitted peak intensities are shown by a dashed line.

Figure 3.4(C), (F) and (I) show the average distributions of the step intensities, with error bars calculated from the standard deviation of values replica experiments (at least 2 - 3 experiments were performed per labeling ratio). The dashed lines represent average of peak intensities (36 ± 2 , 35 ± 4 and 33 ± 2 photoelectrons for the 1, 3 and 10 fluorophores/LNP samples), corresponding to the intensity of a single dye. These mean intensities line up well with peaks from kernel density fitting to the distributions. We observe that higher fluorophore loading can lead to a wider step-size distribution due to some steps catching more than one fluorophore bleaching event in the same exposure time.

Figure 3.5 shows the initial intensities of the nanoparticles before photobleaching. The left column of Figure 3.5 (A, C and E) shows distributions from individual experiments, with kernel density fitting for the maximum likelihood particle intensities. The right column of Figure 3.5 (B, D and F) show the combined distributions of all replicas per labeling ratio. Mean initial particle intensities are calculated from the corresponding experiments and are shown by dashed lines. We convert these distributions to labeled drug loading numbers using the measured bleaching steps in Figure 3.4 listed above, to obtain mean peak loading per labeling ratio (1.5 ± 0.1 , 2.8 ± 0.3 and 12.2 ± 0.9 labeled siRNA molecules for the same three samples with nominally 1, 3 and 10 fluorophore/LNP loading as calculated from formulation fractions). Again, kernel density fitting curves are in good agreement with the measured mean loading per sample.

3.3.5 Simultaneous size and loading measurements of siRNA-LNPs

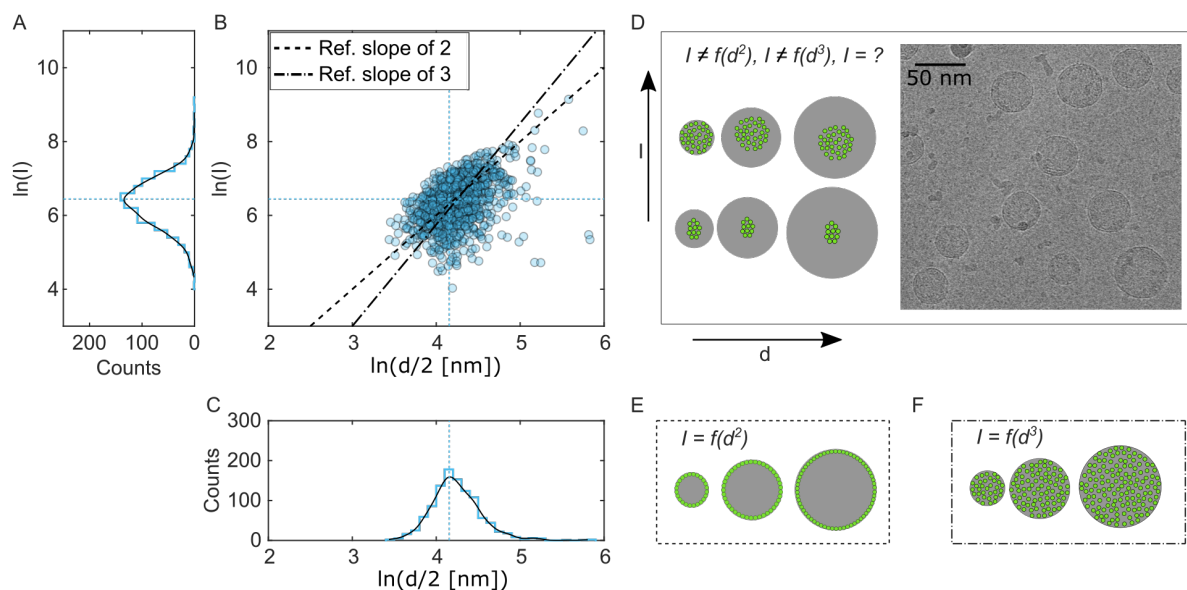


Figure 3.6: siRNA drug distribution in LNPs. Measured fluorescence intensity (A) and size (C) distributions for populations of LNPs formulated with siRNA drugs are projected onto a log-log scatter plot (B); reference lines (dotted/dashed) correspond to potential scaling coefficients between intensity and radius (squared/ cubed), in scenarios where the siRNA is uniformly loaded (on the surface / within the volume). Schematics of three possible distributions of the siRNA drug inside the nanoparticles: surface-loaded (D); volume-filled (E); and uncorrelated (F). The acquired data is consistent with uncorrelated loading.

Figure 3.6 shows the size and intensity analysis of siRNA-loaded nanoparticles, with the same formulation as used above. The nanoparticles were loaded with hundreds of siRNA molecules per LNP (estimated to be 200 to 400 molecules/LNP), where 100 siRNA molecules per LNP were tagged with Tye563 fluorescent dyes. The lipid components were kept the same as those in Figure 3.2, and the nanoparticles were imaged in pH7.4 buffer conditions.

The measured per-particle size (Figure 3.6C) and fluorescence intensity (Figure 3.6A)

distributions are shown projected on a log-log plot in Figure 3.6B for the siRNA loaded LNPs at pH7.4. Interestingly, the scatter plot for the loaded sample does not show strong correlation between intensity and particle size, especially when viewed in comparison to the unloaded data in Figure 3.2. Specifically, while the unloaded LNPs are characterized by a similar spread in size, their intensity has larger relative spread and falls closer to a linear regression line.

This qualitative difference in the two scatter plots provides insight into how the siRNA are distributed inside the LNPs. For instance, our measurements are not consistent with two candidate distributions: a shell-like distribution where the siRNA molecules are embedded between two pairs of bilayers inside the particle (Figure 3.6E), or a volume-filled distribution where the siRNA fills the LNP interior (Figure 3.6F). Both would result in correlated scatter plots which we do not observe (dotted and dashed lines of Figure 3.6B).

Rather, our data is consistent with a weakly correlated scenario (Figure 3.6D), where self-assembled siRNA structures may be loaded in LNPs in a manner which is independent of LNP size. These measurements are consistent with a similar interpretation of Cryo-TEM images of particles with similar compositions (see inset in Figure 3.6D) [84]. Self-assembly of RNA structures is conjectured to be sensitive to properties such as chemical modifications and length of RNA cargo, as well as to the ionic properties of the LNP environment and LNP composition. This analysis thus opens the door to new, quantitative measurements of RNA-LNP size and loading properties, and the relationship between them; measurements which are needed to

understand and optimize a broad class of emerging genetic medicines.

3.4 Discussion

This work begins by benchmarking our tether-free, single-particle measurements of polystyrene nanoparticles with respect to the manufacturer's specifications and establishing agreement with the expected size within ± 1 nm. This analysis involved developing single-particle tracking analysis methods suitable for measuring the diffusion coefficients of confined particle trajectories. Further, converting diffusion coefficient to size measurements required taking into account hydrodynamic effects associated with diffusion near surfaces. Performing measurements for a suite of particle sizes and micro-well dimensions was important to validating our nano characterization approach, demonstrating quantitative agreement with other methods such as Cryo-TEM and DLS.

The most novel aspect of this study is the ability to measure the loading of drug molecules in delivery vehicles, with single-drug and single-particle resolution, at the same time as measuring single-particle diffusion and size. The ability to correlate a loading and diffusion/size measurement on every nanoparticle allows for the construction of the scatter plots and scaling coefficients described in Figure 3.2, 3.3 and 3.6, which give new insights into the spatial distribution of molecules (or drugs) within the nanoparticles. Our technique is capable of delivering simultaneous size and loading information, with the power to discriminate between structural and spatial distribution hypotheses which are essential to understanding drug uptake and delivery mechanisms. To the best of our

knowledge, we have developed the only single-particle technique capable of providing this information without tethering the particles or adhering them to surfaces, and which can be extended to study dynamic changes in particle size and loading, in response to solution conditions such as pH. Dynamic change in these conditions is relevant to driving LNP uptake and drug release in cellular environments.

To date, Cryo-TEM and NMR have been the dominant techniques for measuring indicators of the internal structure of nanoparticles. For example, the Cryo-TEM data on ionizable LNPs has been used to show that the siRNA loading-fraction can change the internal structure of these LNPs from unilamellar to multilamellar, and back to unilamellar internal structure [84]. It's clear that dynamic structural rearrangements of LNPs are possible, which has implications towards how drugs are distributed through the LNPs in changing physiological contexts.

In fact, we obtain average sizes larger than those predicted by Cryo-TEM images of the same LNPs, which was the comparative technique used by prior publications on the same LNP formulations [84]. Our diffusivity measurements correspond to smaller values – slower particles – than would be expected in the scenario where the LNPs were described by hard spheres with diameters reported by Cryo-TEM. This discrepancy could arise for a variety of reasons, including the need for further development of the theoretical model to accommodate the more complex biophysical properties of the deformable LNPs with polymer exteriors (i.e. the PEG brushes are expected to extend out to about 4 nm around the nanoparticles [89]), and potential biases of Cryo-TEM measurements. In comparing our measurements to Cryo-TEM and other techniques, we recognize that different tools

probe different measurable quantities, and that “size” is a term used to describe more than one such quantify. Further, more sophisticated analyses are required to refine and interpret observations of increasingly complex materials, which are made in different contexts - such as diffusion is measured in solution, while Cryo-TEM is performed using particles adhered to a surface.

Soft and structured materials such as LNPs may have more complex diffusive behavior than hard spheres, arising from non-elastic internal degrees of freedom. This may indicate a need for additional modifications of the transfer function Eq. 2 (modified Stokes Einstein equation including hydrodynamic effects) that we used to compare our measurements to Cryo-TEM. While the limited model that we used assumes a hard sphere moving through a viscous fluid, where thermal perturbations are converted into kinetic energy of the particle through elastic collisions, an expanded model could take into account the deformable nature of particles with their own viscosity, diffusing in a medium of different viscosity. This would also include the possibility for thermal perturbations from the medium to exchange energy with the particle’s internal degrees of freedom through inelastic collisions.

In this regard, one outlook of this work is to open the door to new quantitative studies of confinement effects and soft matter biophysics. This would especially apply to samples and environments of increasing biological complexity and physiological relevance, such as confined diffusion in the vicinity of artificial membranes, organelles and living cells.

It is also worth noting that the samples used in our experiments are characterized by a range of siRNA loading which falls between the multilamellar-to-lamellar transition

previously observed with Cryo-TEM. Our measurements are consistent with neither surface nor volume loading but suggest the possibility of a localized cluster of aggregated siRNA whose size has only a weak dependence on the size of the LNP enveloping it. Previously, polarization enhanced NMR spectroscopy has been used to distinguish between homogeneous and heterogeneous shell-core models of LNP structure. The broadening of the NMR signal has suggested that siRNA becomes less mobile upon encapsulation [90]. While this may indicate that siRNA resides in the lipid phase of the LNPs, it is also consistent with localized siRNA aggregation as suggested in this work. Understanding of these structural properties of loaded LNPs, as a function of modifications to the siRNA cargo and LNP carrier, is the subject of future research and will be enriched by the new methodology introduced in this work.

3.5 Conclusion

We have presented a single-particle, high-throughput nano-characterization platform for size/diffusion and loading measurements of drug delivery vehicles. By analyzing many particles individually, we have obtained detailed distributions of particle size/diffusion and cargo loading. The ability to analyze the scaling of intensity with size has made it possible to distinguish between surface and volumetric distributions of cargo loading within LNPs, as well as other more complex distributions. In the case of empty LNPs with labelled phospholipid headgroups, we measured a change from small, bi-lamellar micelles to larger, unilamellar vesicles induced by a change in pH. Analysis of cargo-

loaded LNPs showed that siRNA loading increased the size of LNPs, and suggested that the cargo may be aggregated in a cluster within the LNP rather than being uniformly distributed on the surface or through the volume of the LNP.

Our new technique opens the door to performing size and loading experiments as a function of dynamic changes in solution conditions such as pH, since the entropic confinement of the nanoparticles in wells leaves a thin fluid layer for exchange of reagents during the single-particle imaging experiments. This work is broadly applicable to investigating microscopic and therapeutic properties of a wide range of nanomedicines, as a function of modifications to the drugs and vehicles. We hope that our contributions will help to accelerate the development of next generation of personalized medicines where a high level of resolution and analytical information is required to optimize performance.

3.6 Materials and Methods

Sample Preparation: Polystyrene nanoparticles.

Carboxylate-modified polystyrene nanoparticles (Life Technologies, 48 ± 0.6 nm diameter [78] from EM analysis, excitation/emission = 505/515 nm) were purchased from ThermoFisher Scientific. The nanoparticle samples were diluted to 1 – 2 nM, empirically determined concentrations for achieving a single particle per microwell. The dilutions we performed in serial steps 1:10, and samples were sonicated for at least 20 seconds at each dilution step. Finally, the samples were imaged at concentrations

ranging from 0.82×10^7 to 8.2×10^7 particles \cdot mL⁻¹.

Sample Preparation: Lipid Nanoparticles (LNPs).

Unloaded lipid nanoparticle (LNPs) formulations were prepared by the Cullis laboratory at the University of British Columbia, using the T-junction mixing technique [84, 91–93]. This involved dissolving the 4 different lipid components - including KC2/ Chol/ DSPC/ DSPE-PEG2000 - in ethanol at a molar ratio of 50/ 39/ 10/ 1 mole % respectively, to a final concentration of 10mM total lipid. Then using the T-junction mixer, the organic solution was then mixed with the appropriate aqueous buffer solution. In the case of unloaded LNPs this was either 25mM Sodium Acetate buffer (pH4), or 1X phosphate buffered saline pH7.4.

LNPs containing siRNA drugs were prepared as previously described [84,92], using the T-junction mixer. Again the 4 lipid components (KC2/ Chol/ DSPC/ DSPE-PEG2000) were dissolved in ethanol at a mixing ratio of 50/ 39/ 10/ 1 mole % respectively. The organic solution was then rapidly mixed with an aqueous solution (25mM sodium acetate pH4) containing the siRNA drugs. The concentration of the siRNA drugs was chosen to achieve a high level of encapsulation with charge ratio N/P = 3.

The nanoparticle samples were prepared for imaging by diluting them in the respective buffers - as described above - to empirically determined concentrations for achieving single particles per micro-well (approximately 1 - 2 nM LNP concentration).

Flow cell cleaning and assembly

The flow cell is made of two (25 mm \times 25 mm) glass substrates separated by a 30 μ m thick double-sided adhesive (Nitto Denko, Product No. 5603). The bottom layer

of the flow cell, made of a $200 \pm 10 \mu\text{m}$ thick cover glass (Ted Pella, Product No. 260452), contains an array of wells of varying diameters and depths, patterned by standard photolithography and dry-etched by reactive ion etching (RIE) [74]. For measurements shown in Figure 3.1, the micro-well diameter was $10 \mu\text{m}$ diameter and the depth was varied from 200 to 1200 nm. In Figure 3.2, 3.3 and 3.6, the micro-wells used had $3 \mu\text{m}$ diameter and 500 nm depth, and for Figure 3.4 and 3.5 they had $3 \mu\text{m}$ diameter and 350 nm depth. The top layer of the flow cell, made of $150 \pm 20 \mu\text{m}$ thick standard microscope cover slips (VWR, Product No. CA48366-089-1), has two holes drilled at opposing corners of the square, for sample introduction.

Both top and bottom layers of each flow cell were passivated with PEG layers, using a cloud point PEGylation technique described in literature [94, 95]. The layers were rinsed thoroughly three times with Deionized (DI) water and blow-dried with high purity nitrogen before flow cell assembly. The assembled flow cell is then sealed in a custom microfluidic chuck [73].

Single-molecule CLiC microscopy

The microscopy setup and imaging were performed using CLiC [72]. Briefly, a microfluidic chuck for sample exchange was used to hold the flow cell on a microscope sample plate, located between the objective and the CLiC pusher lens (Figure 3.1A). The bottom coverslip was patterned with arrays of cylindrical, open face microwells (Figure 3.1A (i)) within which the nanoparticles were laterally confined (Figure 3.1A (ii) and (iii), and 1 B), as the two coverslips were deflected and brought into contact.

During the experiments, the CLiC lens was lowered and raised repeatedly to trap and

refresh the wells with new particles from the bulk solution. This allowed for quantitative measurements of a statistically relevant number of individual nanoparticles, which is important for characterizing heterogeneous samples. Videos of single particle trajectories (Figures 1 B and C (i)) were collected using an iXon Ultra 897 EMCCD camera with either 40x (Figure 3.1 and S1) or 100x (Figures 3.2 – 3.6) magnifications (on-camera pixel size was 16 $\mu\text{m}/\text{pixel}$). Optimal imaging parameters such as exposure time and laser power were chosen with feedback from variance and bias values obtained from computer simulations of particles diffusing in a 2D Gaussian light intensity profile under, a circular well confinement with a known diffusion coefficient. This procedure led us to choose 600 frames (at 20 ms exposure) for polystyrene nanoparticles (Figure 3.1), and 2000 frames (at 6 ms exposure) for LNPs (Figures 3.2, 3.3 and 3.6). In the case of the photobleaching experiments (Figure 3.4 and 3.5), at least 6000 frames were collected at 2 ms exposure time.

Single-particle trajectory analysis to determine diffusivity

To measure the size and intensity of single-particles, we employed single-particle identification, tracking, and a mean-squared displacement (MSD) analysis adapted for confined diffusion in a circular geometry. Wells with single diffusing particles were identified (details in SI - Pyramid approach to particle detection) and used for analysis, while wells containing multiple particles were excluded. Single-particle tracking (SPT) was then applied to each individual well [96, 97]. Localization of the single diffusing particle was achieved by fitting the signal in each frame with a two-dimensional symmetric Gaussian [98–100] (Figure 3.1 C, ii)). Trajectories were obtained by

compiling successive positions obtained on each frame.

To determine the diffusion coefficients, empirical MSD points were generated for increasing time lags from SPT trajectories using Eq. S3 in SI. The points are shown in Figure 3.1D. The diffusion coefficients are extracted by fitting with a theoretical confined MSD model for circular confinement [79]. We additionally modified the existing 2-D circular confinement MSD model for fitting, as the finite exposure time effect and shot noise are expected to contribute in the form of an offset [80]. For long time scales, the MSD curve saturates and this is characteristic of the particle experiencing confined diffusion due to the microwell. At short time scales, the particle undergoes free diffusion and the MSD curve is approximately linear. Further information is provided in the SI.

Single-particle diffusivity analysis to determine size

Normally the Stokes-Einstein equation is invoked to transform diffusion coefficient (D_0) to hydrodynamic radius (a):

$$a = \frac{k_B T}{6\pi\eta D_0}, \quad (3.1)$$

where k_B is the Boltzmann constant, T is the temperature, and η is kinetic viscosity of the solution. Because our measurements are taken under confined conditions where the size of the particle can be a significant fraction of the vertical dimension of our microwell, we must correct for the effect of hydrodynamic forces acting near the top and bottom confining surfaces. When the particle is near a surface it slows significantly, resulting

in lower diffusion coefficients which would result in diameters that are too large if the unmodified Stokes-Einstein equation were used. We use the following equation [81]:

$$D_{\parallel} = \frac{k_B T}{6\pi\eta\lambda a} = \lambda^{-1} D_0, \quad (3.2)$$

for the diffusion coefficient D_{\parallel} measured near to parallel confinement surfaces. λ is the correction factor for diffusivity of particles confined between two parallel walls with a separation distance d_w . For a particle midway between the walls, with a radius $a = d/2$, λ can be obtained as a polynomial expansion in a/z [81, 101]:

$$\lambda^{-1} = 1 - 1.004 \left(\frac{a}{z}\right) + 0.418 \left(\frac{a}{z}\right)^3 + 0.21 \left(\frac{a}{z}\right)^4 - 0.169 \left(\frac{a}{z}\right)^5 + O\left(\frac{a}{z}\right)^6. \quad (3.3)$$

where $z = d_w/2$ is the midway distance between the two planes of confinement. We use a series of experiments (Figure B.1 and Table B.2) with varying confinement heights to fit for the correction factor (see SI: - ‘Corrections for size measurement under parallel planes of confinement’ for details). By doing this we are able to use information from measurements at all confinement depths to yield a particle size that best fits all the data.

Photobleaching analysis for cargo loading

We used a stepwise photobleaching approach to count the fluorophores attached to a given molecule or nanoparticle. While this is easier to implement compared to other advanced statistical methods, it can be hard to detect photobleaching steps when the total number of fluorophores is large, or the signal-to-noise ratio is low. Therefore, the

method used here should only be used when the average number of fluorophores per particle is small or the last photobleaching steps are easily distinguishable. On the other hand, when the average number of fluorophores is large, advanced methods should be used (i.e. Bayesian counting methods [102, 103]). Fortunately, given the fast imaging timescales used (at frame rate of 2 ms as shown Figures 3.4A, D and G) for intensity traces obtained using the CLiC platform, any fluorophore counting method using raw intensities can be used.

A particle labeled with multiple fluorophores shows stepwise drops in intensity, corresponding to independent photobleaching events. These intensity steps are detected using an algorithm reported by Chen et. al [104], which is based on the two-sample t-test edge detection. Due to noise in the intensity trace, the edge detector will sometimes miss transition times and count multiple steps as a single one. This is evident in the increasing skewness of the single bleaching step distributions (3.4D, E and F). By using kernel density estimation to fit the distribution of these intensity steps, we can accurately find and avoid overestimating the unit step size ΔI of a single photobleaching event (details in SI - Analysis Method: Particle loading). To determine the number of fluorophores per particle, we divide the total change in particle intensity by the unit step size of a single fluorophore.

3.7 acknowledgement

The authors acknowledge technical, operational and financial support from a number of sources. A number of members of the Leslie laboratory and collaborators contributed to the work. This includes Z. Zhang who contributed background theory to this work, which was published in his M.Sc. thesis. Former undergraduate students in the Leslie laboratory H. Liao, Y. Patel, Y. Ji and S. Chen also contributed to the project. Further to this Dr. D. Berard supported aspects of the technical research and Dr. K. Metera supported communication aspects of the project. Dr. M. Shayegan took data with a different class of nanoparticles which preceded this work and helped validate its continuation. Operational support of the research laboratory was provided by Department technicians R. Talbot, R. Gagnon and J. Smeros at McGill Physics. Further, the McGill Nanotools facility provided fabrication infrastructure for constructing the flow cells. Funding for this work was largely provided by the NSERC Idea to Innovation research programs (Phase 1 and 2), the NMIN Strategic Initiative at UBC, and Mitacs fellowships, all in partnership with ScopeSys, a company spun out of the Leslie lab.

Supporting Information Available, including:

- Comparisons with other sizing techniques
- Particle detection, tracking and sizing
- LNP cargo-loading distributions
- Simulation of confined particles

Chapter 4

Conclusion and Outlook

In closing, this thesis makes significant contributions to the fields of biophysics and biotechnology, with applications to new genetic medicines and vaccines, by performing innovative work at the interface between physics, biochemistry, polymer science, and medicine. It includes two complementary studies on biopolymers and lipid nanoparticles. In the first study, we investigated the behavior of DNA molecules under a continuum of confinement regimes. In the second, we developed a single-particle analytic approach for probing multiple correlated properties of lipid nanoparticles developed for drug delivery.

These achievements were made by using and further innovating a combination of CLiC microscopy, micro-fabricated flow cells, as well as computational simulations and data analysis tools. The research in this thesis is performed in the context of a single-molecule biophysics team, which collaborates with health scientists, theoretical physicists and data scientists and experts on surface chemistry.

The first study is presented in Chapter 2. This work applied CLiC to directly measure the free energy of confinement for linearized DNA polymers in a slit-like geometry across a wide range of slit heights. This was achieved by directly counting individual molecules and then calculating concentrations as a function of applied confinement. We used linearized

pUC19 – a relatively short molecule – in order to access a wide continuum of confinement regimes. Using our experimental results, as well as Monte Carlo and Langevin dynamics simulations we were able to connect confinement regimes described by the theories of Odijk (strong), Chen and Sullivan (strong-to-moderate), and Casassa (moderate-to-bulk).

This comprehensive validation indicates that Eqs. 2.3 and 2.4 provide accurate and versatile predictions even beyond the polymer length-scales for which the Chen-Sullivan model was derived. The experimental and simulation results, methods, and instrumentation delivered by this paper provide crucial information for modeling and understanding the behavior of polymers in a confined space – including nanoparticles and target cells – with important applications for drug delivery.

The second study featured in this thesis in Chapter 3 introduces a single-particle, high-throughput nano-characterization platform for size and loading measurements of drug-delivery vehicles. This was achieved by combining CLiC microscopy with micro-fabricated array wells, which allow for many cycles of parallelized measurements on single-particles. In parallel we developed quantitative simulations and models of our data. We validated our methods with measurements on polystyrene nanoparticles, which showed agreement with the manufacturer’s specifications after corrections for confinement effects.

We then applied our approach to lipid nanoparticles. By analyzing many (1000) particles individually, we obtained detailed distributions of particle size and cargo loading. The single-particle resolution of these measurements gives us the ability to analyze the scaling of fluorescence intensity (i.e. drug loading) with particle size and yielded new insights which distinguish different particle structures e.g. surface (scaling

of 2) or volumetric (scaling of 3) distributions of cargo loading within LNPs, as well as other distributions. In the case of empty LNPs with labelled phospholipid headgroups, we measured a change from small, bi-lamellar micelles to larger, unilamellar vesicles induced by a change in pH. We then verified our approach by performing measurements on well-characterized, larger bilayer LNPs.

Measurement and analysis of drug cargo loaded LNPs showed that siRNA loading increased the size of LNPs as expected. However, the resulting size and intensity distributions of fluorescently labeled drug molecules show very weak correlation, with no clear scaling exponent. If size and loading are not correlated, this suggests that the cargo may be aggregated in a cluster of random size within each LNP rather than being uniformly distributed on the surface or through the volume of the LNP.

These results lead to an array of future investigations into important questions regarding the loading of LNPs with drug cargo, as well as its release. Fluid cells can be designed with nano-pillars to act as spacers for the roof of the CLiC cell, with a gap much smaller than the trapped LNPs but large enough to allow a continuous fluid layer for exchange of reagents during the single-particle imaging experiments. This opens the door to performing size and loading experiments as a function of dynamic change in solution conditions such as pH. Moreover, drug cargo can also be introduced in real time to bare LNPs, and the non-equilibrium loading kinetics of the particles can be observed in real time. Similar experiments can be designed to investigate the release of drug cargo from loaded LNPs, in response to changes in chemical conditions which mimic those encountered by the drug carriers at various stages of the intracellular

delivery pathway. Moreover, the CLiC fluid cell can be adapted for cellular applications by making much larger micro-wells designed to trap whole cells with larger gaps at the ceiling to allow for the introduction of LNPs, for studies of cellular uptake.

A number of fundamental biophysical and soft-matter studies also arise from the results presented here. Sizing measurements on LNPs resulted in lower diffusion coefficients than expected from comparisons with DLS and CryoEM data, even after applying confinement corrections. Further work is needed for a better understanding of the behavior of soft particles in confinement. One possibility is that the soft particles get deformed under the entropic force they experience, resulting in the observed deviations. A more detailed theoretical model may be needed for making confinement corrections to the Stokes-Einstein relation, which account for sticking and deformations at the confining surface. A related hypothesis is that for soft materials a fraction of thermal perturbations are absorbed into internal degrees of freedom, as inelastic collisions which do not propel the particle through solvent, resulting in lower diffusivities for soft particles of the same size as hard particles. CLiC microscopy provides an excellent platform for detailed investigations of these fundamental questions.

Another interesting study would be to design confinement experiments like those we used for polymers in Chapter 2, but applied to deformable LNPs in Chapter 3, to probe structural changes in the particles as a function of applied confinement. Further studies of model carrier systems are also needed to explore the scaling exponent in our plots of drug loading vs nanoparticle size, especially to understand the significance of uncorrelated

relationships seen in our study of siRNA loading of LNPs.

As an immediate outlook to this thesis, it would be interesting to establish optimal model systems which would be expected to show uniform volume (exponent 3), surface (exponent 2), linear (exponent 1) and point (uncorrelated) distributions of cargo loading. Performing these measurements on increasingly complex samples and as a function of confinement, varieties of and modifications to biomaterials (polymers, particles, viruses, etc), and environment (glass, coated glass, bilayer, cell membrane, etc) will provide new insights into how complex biomaterials behave in confined spaces such as in the interior of cells. A broad outlook is to combine the different dimensions of work now performed using the CLiC platform - imaging molecules, particles, and live cells - and explore the biophysics of molecular interactions across a range of scales and in increasingly complex/physiological settings.

In closing, the work presented in this thesis is broadly applicable to investigating microscopic and therapeutic properties of a wide range of nanomedicines and nanomaterials, as a function of modifications to the drugs and delivery vehicles, contributing to the development of next generation of personalized medicines where single-molecule and single-particle resolution is required.

Appendix A

Supplementary Information (SI): Free Energy of a Polymer in Slit-like Confinement from the Odijk Regime to the Bulk

A.1 Methods

A.1.1 Flow Cell Preparation

Standard coverslips, No. 1 (25 mm square, 130–150 μm thick, part No. 48366-089, VWR) and No. 1.5 (25 mm square, 160–190 μm thick, part No. 48366-249, VWR), were used to make the imaging flow cells. The No. 1 coverslips were UV-laser-etched to form sample inlets. Coverslips were cleaned by immersing them in a warm bath of Hellmanex III detergent, followed by ethanol, acetone, and then deionized water baths, consecutively, all at 50°C for 20 minutes each. They were then treated with piranha solution (2:1 mixture of sulfuric acid and 30% hydrogen peroxide) for 30 minutes and finally with 1M potassium hydroxide for 15 minutes.

Flow cells were formed by adhering the No. 1.5 coverslips to the No. 1 coverslips using

a double-sided adhesive tape (30 μm thick, Nitto Denko 5603; 10 μm , Nitto Denko 5601). Tape patterns were laser-cut at the center to form a flow channel and a circular imaging chamber, as shown in Figs. 1b and 4 of Berard *et al.* [57]. The choice of tape thickness determines the height gradient of the chamber.

A.1.2 DNA Sample Preparation

Linearized pUC19 samples were extracted and purified from transfected *E. coli* cells and then treated with the single-cutting restriction endonuclease NdeI (NEB), and purified on a spin column (Qiagen) into in a $1\times$ TE buffer solution (10 mM tris-Cl (pH 8.0) and 1 mM EDTA). EDTA was added to chelate divalent cations to inhibit DNase activity from enzymatic contaminants.

DNA labeling was done by preparing equal volumes of the DNA sample in $1\times$ TE buffer and YOYO-1 dye (absorption peak = 489 nm), also dissolved in $1\times$ TE. The YOYO-1 concentration was set such that there were 10 base pairs per YOYO-1 molecule. As YOYO-1 lengthens dsDNA by 0.5 nm per YOYO-1 molecule, for our pUC19 plasmid of 2686 bp, the contour length increases by 134 nm, to 1.047 μm [105], corresponding to an ideal wormlike-chain R_g in bulk of 123 nm. The DNA was added to the YOYO-1 and left to sit in the dark for 50 minutes. The sample was then refrigerated, ready for experiments.

Nonreactive Cy5 dye (absorption peak = 650 nm) was used for chamber height measurements. It was also prepared in $1\times$ TE buffer and refrigerated.

Immediately before performing experiments, the labeled DNA and Cy5 were added

to the experimental buffer, 50 mM tris-Cl (pH 8.0), 1 mM EDTA, along with 1:100 β -mercaptoethanol (BME) as an anti-photobleaching agent. The BME also prevents photonicing of the DNA caused by covalent reactions between the DNA and YOYO-1 dye. At pH 8.0 at room temperature, tris is 64% ionized and EDTA is mostly triply ionized, and so the ionic strength of our solution was 35 mM, which gives a Debye length < 2 nm, so the DNA's electrostatic interaction with the walls is negligible. Also, at this ionic strength, the Kuhn length has been predicted by OSF theory to deviate negligibly from the standard value of 100 nm [106, 107]. Competing theories exist [108, 109], but experimental measurements are in insufficient agreement to conclusively support any one over another [110, 111], and so we have elected to assume $L_K = 100$ nm.

A.1.3 Microscope and Illumination

The experiments were performed on a Nikon TI-E microscope with a $60\times$ NA 1.49 oil immersion objective (Nikon part no. MBH76160) or a $40\times$ NA 1.30 oil immersion objective (Nikon part no. MRH01401). The objective was mounted on a Perfect Focus System (PFS), which allows for automated corrections of drift in the objective's focus. Images were acquired with an Andor iXon 897 EMCCD camera with the sensor cooled to -70°C . A Coherent 488-nm Sapphire laser was used to excite stained DNA molecules, with its power 3.6–7.2 mW at the objective, and 50 ms exposure time. The same 488-nm laser was used to acquire interference fringe images, attenuated to 0.036–0.072 mW at the objective with an OD2 neutral density filter, for chamber geometry characterization. A second laser (647 nm Coherent OBIS at approximately

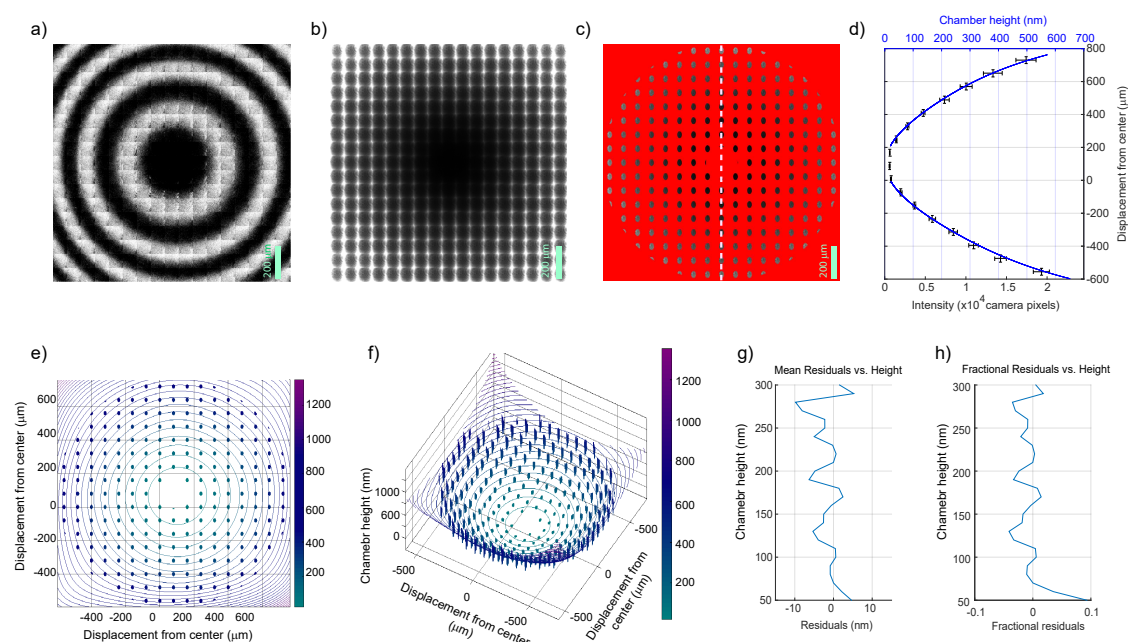


Figure A.1: Chamber height characterization. The same y axis applies to panels **a** through **d**. **a)** Fringe scan: Stitched 17×17 raster scan of interference fringes caused by chamber geometry using 488-nm laser source. Exposure time = 50 ms; magnification = $90\times$ ($60\times$ objective and $1.5\times$ relay lens); total imaging region = $1360\text{-}\mu\text{m}$ square, step sizes = $80\ \mu\text{m}$, number of frames = 1. **b)** Dye scan: fluorescence of free Cy5 molecules in the chamber, with identical acquisition parameters as fringe scan, save for excitation with 647-nm laser; exposure time = 200 ms. **c)** Masked dye scan: Regions colored red are not used for the chamber height fit, eliminating the rasterization effect of the unmasked dye scan. The exclusion of regions of the chamber outside the doughnut-shaped area eliminates the center of the chamber, which, owing to coverslip-coverslip contact, deviates significantly from a polynomial curve, as well as the corners of the chamber, which are too dense with particles to be analyzed and thus an accurate determination of their height is not necessary. Dashed white line is the line along which the chamber height profile is shown in **d**. **d)** Chamber height profile: Solid blue line shows the fitted chamber height along the dashed white line in **c**. The central region of the chamber excluded from the fit is not shown. Black points and horizontal error bars show the mean and standard deviation in the normalized dye intensity for the parts of the fields of view along same dashed white line that are not masked out. Vertical error bars are the width of the non-masked out areas. Scaling the polynomial fit to absolute heights for this dataset was based on fixing the height to match two interferometry minima (innermost and second-innermost dark ring in **a**). Inset: Dye intensity at low chamber heights. **e,f)** Plots of dye intensity (solid surface plot) and fitted chamber contours (lines) from different viewing angles (directly above, and tilted, respectively). **g,h)** Mean residuals in (absolute and proportional) of the fitted height, in 10-nm height bins.

0.1 mW power) was used to acquire dye images, also to be used for chamber geometry characterization.

A.1.4 CLiC Microscopy Setup

The prepared flow cell was placed on a microscope plate. A chuck shown in Fig. 1 (main text), with reservoirs for flowing samples into the flow cell was mounted onto the flow cell and microscope plate, using thumbscrews. The microscope plate was then mounted on an XY-meso stage (Mad City, custom-made) above the objective of the microscope.

The flow cell chamber was initially wetted with 50 mM tris-Cl (pH 8.0), 1 mM EDTA solution. The push-lens was then lowered (controlled by a nano-positioner, part No. P-602.1SL, Physik Instrumente) onto the flow cell to form the CLiC chamber. The distance required to achieve coverslip-coverslip contact was determined by observing interferometry rings. To establish a stable imaging chamber, the push-lens was over-pushed by 2 μm beyond the first point of contact. Measurements were done by performing raster scans (with grids of 15×15 to 21×21 fields of view, see Fig. A.1). Chamber stability and symmetry were verified before flowing in DNA samples. Typically, the chamber stabilized completely after tens of minutes, but three fringe scans (Fig. A.1a) were taken over a period of one hour to be certain.

Once a stable chamber was verified (by reproducible fringe profiles), the DNA sample was prepared for flowing into the imaging chamber. DNA samples were diluted to a desired concentration, mixed with the Cy5 dye (final concentration, 2.3 μM), and loaded into the chamber. This concentration of DNA in the chamber, denoted as the bulk concentration C_{bulk} , determined the accessible range of confinement height. Hence several experiments with varying C_{bulk} were performed as shown in Fig. 2 (main text).

A.1.5 Data Collection

The DNA sample was allowed to equilibrate for an hour after insertion into the chamber. This period was established by repeatedly measuring concentration profiles after this elapsed time and identifying when concentration as a function of position stopped varying with time. Data collection involved a sequence of measurements of the dye scans (Fig. A.1b), DNA scans (Fig. A.2), and fringe scans (Fig. A.1a), taken in that order. There was no risk from the dye scan of bleaching the DNA, since YOYO-1's absorption at 647 nm and Cy5's absorption at 488 nm are both negligible. Interferometry scans were performed after the first DNA scan since they were performed with the same laser wavelength as the DNA scan. Additionally, the laser intensity was decreased by a factor of 100 when performing fringe scans.

Both the DNA and the dye scans required acquiring high resolution images (80- μm square field of view). The PFS was used to adjust the focus during scans to correct for small deformations in the bottom of the chamber when required (~ 100 nm or less, for the entire imaged region). Measurements were repeated over several hours, to verify chamber geometry stability and sample equilibration. Once enough measurements were obtained, the push-lens was lifted such that the chamber was $\sim 0.5 \mu\text{m}$ at the center. A dye fluorescence image was taken at this height, denoted the "probe image", to capture the spatial variation in the illumination intensity.

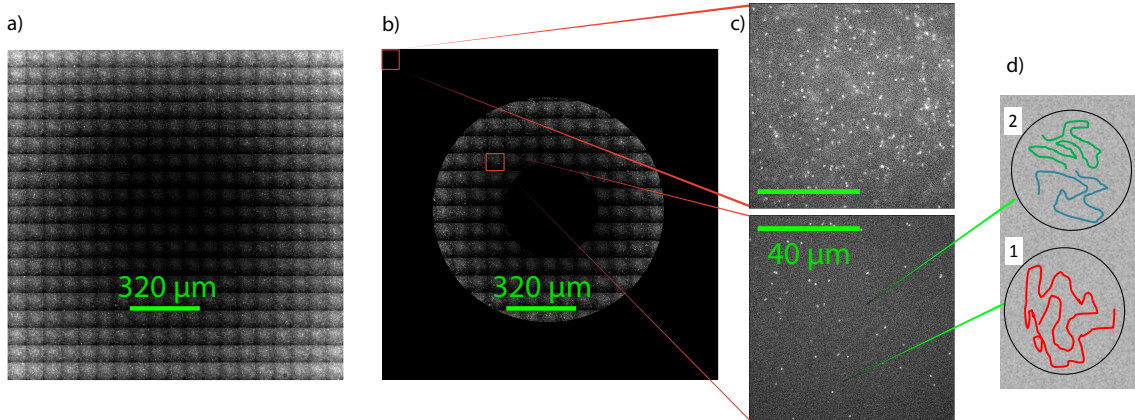


Figure A.2: **a)** DNA scan: Stitched 19×19 raster scan of the fluorescence of freely diffusing DNA molecules. The images were taken using a 488-nm laser source to excite the YOYO-1 DNA stain. This scan was performed with the following settings: Camera magnification = 90, step sizes = $80 \mu\text{m}$, number of frames = 50. **b)** Masked DNA scan. A ‘doughnut’-shaped mask was used to select regions of the full scan that can be used for tracking molecules. The center is masked out because there were no molecules to track at the center, while the peripheral area is masked out because the chamber height in that area is significantly greater than our optical system’s depth of field, and thus molecules can appear blurry and are not tracked reliably. **c)** Selected fields of view from the stitched scan, to compare the “trackable” region to the region where particles are not reliably in focus. **d)** Schematics of typical particle trajectories obtained from the particle tracking algorithms.

A.2 Data Analysis

A.2.1 Chamber Height Characterization

Chamber height calculations were performed in MATLAB. Characterizing chamber geometry was performed in two steps. First, dye fluorescence intensity throughout the chamber (which is proportional to chamber height) was fitted to a sixth-order, two-dimensional polynomial. Second, direct interferometry was performed as described by Berard *et al.* [57]. Interferometry data was used to scale and constrain the chamber fit based on the dye fluorescence.

Images taken of dye fluorescence were first normalized by a Gaussian fit of the probe image. This was necessary to eliminate the laser beam profile, which gives a noticeable rasterization effect, from the dye fluorescence images. The normalization was done as shown below;

$$I_{\text{norm}} = \frac{I_{\text{scan}} - \min(I_{\text{scan}})}{\tilde{I}_{\text{probe}} - \min(\tilde{I}_{\text{probe}})} + \min(I_{\text{scan}}) \quad (\text{A.1})$$

where I_{scan} are the scan images, $\min(I_{\text{scan}})$ and $\min(\tilde{I}_{\text{probe}})$ are the minimum intensity pixel of all the scan and probe images, respectively, and \tilde{I}_{probe} is the Gaussian fit of the probe image.

The normalized dye images were stitched into a single image—a *dye scan*, as shown in Fig. A.1b. To reduce rasterization effects, the edges of the fields of view making up the complete dye scan were masked out (Fig. A.1c). The stitched image was then fitted to a sixth-order polynomial subject to constraints (discussed below). Residuals between the fit and the rasterization-corrected dye scan are shown in Fig. A.1g,h. The fitting relied on the coverslip-coverslip contact during measurements. This was achieved in experiments by over-pushing the push-lens (as mentioned in CLiC Microscopy setup above) and monitoring the interferometry scans, making sure the center remained maximally dark.

The interferometry images, Fig. A.1a, were used determine the fitted chamber height map in two ways. First, they were use to constrain the polynomial fit of the stitched dye scan. Pairs of points on different fringe minima (dark rings) i and j were chosen and the

fit at those points was required to yield a ratio of $i/j \pm 0.02$ at these positions. Chamber heights at interferometry minima were given by

$$h_m = \frac{m\lambda}{2n} \frac{1}{\cos(\theta)} \quad (\text{A.2})$$

where m is the m th dark ring from the center, λ is the illuminating laser's wavelength, n is the solution's index of refraction, and θ is the laser beam's incident angle.

In addition to constraining the fit algorithm, the fringe minima were used to scale the resulting polynomial fit, converting it from intensity units to nanometers. The fit was scaled by fixing the height at a fringe minimum as close to the middle of the dataset's usable height range to the height given by Fig. A.2 and the height at the minimum of the polynomial fit to zero. Fig. A.1c shows a profile of the dye fitting along a vertical axis, and it agrees with the interferometry rings. Height assignments are accurate within 5% based on systematic and statistical uncertainty in the chamber height fit, as described in Ref. [57, 112] and in Fig. A.1, except at heights < 100 nm. Here, near the point of coverslip-coverslip contact, the chamber geometry is distorted from a polynomial. At these low heights, we find that scaling the fit using the two innermost interferometry minima rather than fixing the minimum of the fit to zero height gives better results (Fig. A.3). The effect of this alternative scaling procedure is significant only for the two highest-concentration data sets, $C_{\text{bulk}}/\max(C_{\text{bulk}}) = 1.0$. For datasets with all heights > 100 nm, the difference between the two methods of scaling the polynomial fit is negligible.

Horizontal error bars in Fig. 3 of the main text were assigned as follows. Within each annulus representing a height bin, the height at every pixel is determined directly from dye fluorescence (converted from intensity to nanometers using the interferometry scan). As the dye scan has experimental noise and a non-constant excitation profile, the range of heights as would be implied by the dye scan within an annulus is greater than the range of heights in the polynomial fit within the same annulus. The horizontal error bars indicate the range from the 25th to the 75th percentile in these dye-derived heights (rather than the fit-derived heights).

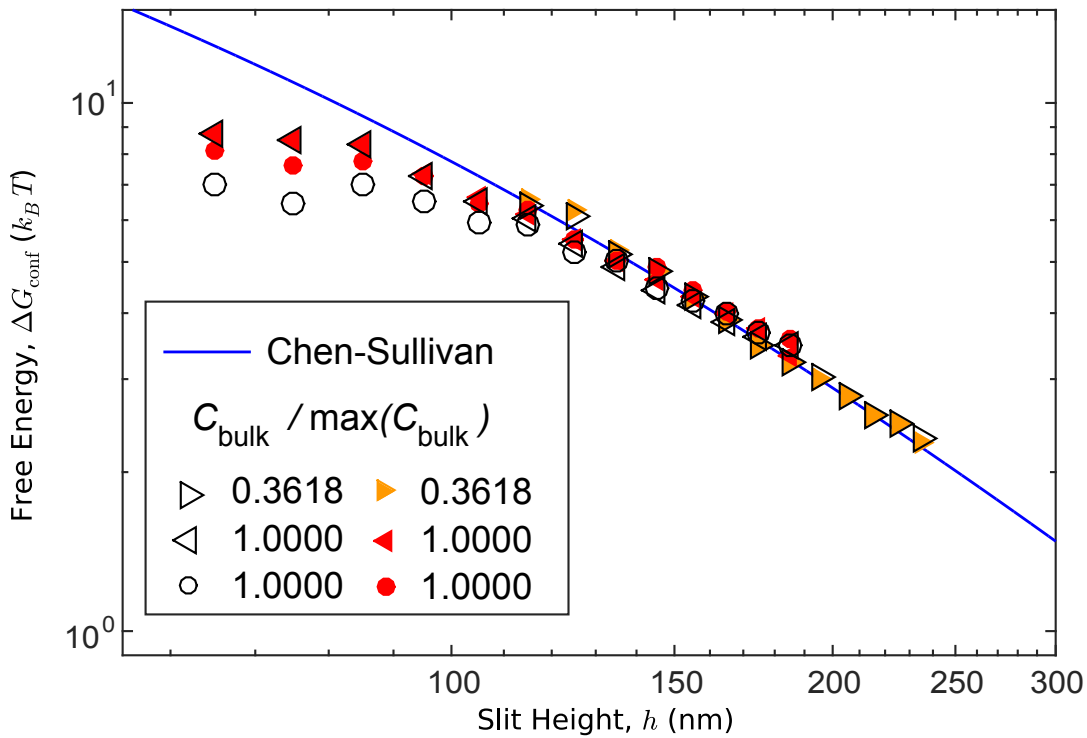


Figure A.3: ΔG_{conf} versus h , showing the effects of the alternative chamber-fitting technique. Colored markers show measured ΔG_{conf} for the three highest-concentration datasets, using the technique of scaling the polynomial fit of the measured dye intensity based on the two innermost interferometry minima. Uncolored open markers show ΔG_{conf} using one interferometry minimum and fixing the height at the position in the chamber corresponding to the polynomial fit's minimum.

A.2.2 Particle Identification and Trajectory Analysis

This step was performed using an ImageJ plugin that we adapted for our purposes for particle detection and tracking. It uses the “feature point detection and tracking algorithm” as described by Sbalzarini and Koumoutsakos [60]. Mobile particles were consistently 5 \sim 10 times brighter than the noise floor, and of visually uniform brightness. After the tracking algorithm was run, resulting trajectories were inspected to ensure that the tracker accurately found particles.

Before executing the particle-tracking algorithm, regions of interest were selected for each dataset. The highest trackable height was limited by either DNA’s bulk concentration or the objective’s depth of focus (Fig. A.2c top image). The lowest trackable region is also limited by bulk concentration and particles exclusion. Areas of the scan with heights outside this trackable regime were masked out, as shown in Fig. A.2b.

A.2.3 Counting Particles as a Function of Height

Every trajectory was assigned to a chamber-height bin (determined from its x, y coordinates and the aforementioned height map). During a movie, particles can enter or exit a field of view or visually overlap with other particles and thus create trajectories shorter in duration than that of the movie. Accordingly, we multiplied each trajectory’s contribution to the total particle count of a bin by the fraction of the movie for which the trajectory is found in the bin. This produces *notional* particle count $N(h)$ shown in

Fig. 2a (main text) as a function of height for a series of different bulk concentrations C_{bulk} .

$$N_{\text{average}}(h) = \frac{\sum_i^N t_i}{T \cdot A_{\text{annulus}}} \quad (\text{A.3})$$

where $N_{\text{average}}(h)$ is the particle concentration in one of the binned annulus at height h , N is the number of trajectories in the bin, t_i is the length of time of the i th trajectory, T is total length of the movie, and A_{annulus} is the annulus area.

In regions of high areal concentration, particles frequently visually collide, and the tracking algorithm momentarily loses a particle. This can result in an undercounting of lifetime-weighted particles. To ensure that our analysis was not significantly affected by this undercounting, we performed simulations of particles undergoing normal diffusion. Movies of this simulated data were constructed using experimentally determined point-spread-functions of the particles and experimental noise. We found that at an areal density of 10^{-8} particles per nm^2 , 2% of total trajectory length is lost, and so for all datasets, only height annuli with areal densities below this value were included. Undercounting can also be caused by particles momentarily moving outside of the depth of focus of the optical system, although at heights and concentrations used in our work this effect is less prevalent than undercounting due to particle overlap.

A.2.4 Calculating the Confinement Potential

The confinement potential calculations were performed using the relation for the change in free energy as a function of concentration.

$$C(h) = C_{\text{bulk}} \exp \left[\frac{-\Delta G_{\text{conf}}(h)}{k_{\text{B}}T} \right] \quad (\text{A.4})$$

$$\frac{\Delta G_{\text{conf}}(h)}{k_{\text{B}}T} = -\ln \left[\frac{N_{\text{average}}(h)}{h} \right] + \ln(C_{\text{bulk}}) \quad (\text{A.5})$$

where $C(h)$ is the particle concentration at height h , and ΔG_{conf} is the change in confinement free energy.

For each height h , a weighted mean of the ΔG_{conf} values from all datasets that were analyzed at that height was computed. Weights were proportional to the total number of particles counted for that height in a dataset.

A.2.5 Assigning Bulk Concentration per Dataset

A direct endogenous determination of the true bulk concentration C_{bulk} of a DNA in a dataset cannot be made in the experimental chamber. C_{bulk} may differ from the concentration based on spectrophotometric measurements of stock solution and dilution ratios because of (1) aggregation, (2) fragmentation of DNA, (3) the sticking of molecules to apparatus surfaces, and (4) inaccuracy of pipettes used for dilution. As (1–3) can only reduce the true C_{bulk} , we expect it to be lower than the calculated

concentration in the sample tube, C_{tube} .

To identify the true concentration of DNA in our experiments, we followed a two-step procedure. The first step is to measure the relative concentration at common heights across experiments to scale one experiment to another. We counted the number of particles in the highest common height annulus¹ for the highest-concentration datasets ($C_{\text{bulk}}/\max(C_{\text{bulk}}) = 1.0$ in Fig. 2 (main text)). We then scaled C_{tube} of lower-concentration datasets ($0.1 < C_{\text{bulk}}/\max(C_{\text{bulk}}) < 1.0$) that overlapped with this annulus so that the resulting concentrations of the lower-concentration datasets would imply the observed number of particles in the annulus². We repeated this procedure for the next set of lower-concentration datasets, adjusting their nominal concentrations based on the highest common annulus of the preceding set. These adjustments to C_{tube} were determined entirely by the observed concentrations of particles at overlapping annuli, and used no fitted or free parameters.

After this adjustment of concentration ensured that the datasets were internally consistent, we fitted the average ΔG_{conf} curve resulting from the 16 datasets to a combined theory curve. For the purpose of this fit, the prefactor in the Casassa formula is adjusted to take into account the semiflexibility of our polymers (see SI, “Simulations”); the prefactor is the unique choice that positions the Casassa curve such that there is a single point at which it agrees with the CS curve in both free energy and

¹The highest annulus in a particular experiment is the binning at the highest height in that experiment. For a set of experiments with overlapping heights, the highest common annulus is the binning at the highest shared height.

²The goal of this step is to estimate the true concentration of each experiment. The experiments at the lowest heights used higher nominal concentrations; and hence required less dilution and pipetting, introducing less potential for error. We therefore chose them to estimate the bulk concentration of those experiments that used lower concentrations and had overlapping heights.

force of confinement. Geometrically this is equivalent to moving the Casassa curve vertically on a log-log plot until it is tangent to the CS curve.

The combined theory curve is defined by the Chen-Sullivan (CS) curve at heights lower than the height at which the CS and Casassa curves coincide and by the Casassa curve at greater heights (see Fig. 3 (main text)). We fit for a single parameter by which to multiply every dataset's adjusted C_{bulk} that minimized the sum-of-squares difference between the theory curve and the mean ΔG_{conf} . It is important to fit the mean ΔG_{conf} data rather than measurements of ΔG_{conf} from each individual dataset so as not to bias the fit toward height regions that happen to be dense with experiments. The value of this parameter was 0.86, reflecting a reduction of 14% in the true C_{bulk} relative to the endogenously-rescaled C_{tube} values.

A.3 Simulations

In order to map out the free energy from the bulk to Odijk scaling regimes, two simulation approaches are used: a Monte Carlo (MC) method is used for larger slit heights and Langevin Dynamics (LD) simulations are performed for very tight slits.

For the Monte Carlo simulations, persistent pseudo-random walks are built by picking a random displacement unit vector \vec{v}_n and evaluating its associated energy

$$U_{\text{bend}} = \kappa(1 - \cos \theta), \tag{A.6}$$

in relation to the previous bond vector \vec{v}_{n-1} . The step is rejected or accepted using a

Metropolis scheme. To calibrate the model, unconfined chains of N -steps between 10–1000 are built in free space. From those conformations, the effective persistence length is found by a fit to the Kratky-Porod relation. We find that $\kappa = 5.0$ yields chains with a persistence length of $L_p \approx 4.0$ unit bond vectors. From this, our MC chain consists of $N = 84$ steps which corresponds to the persistence-length-to-contour-length ratio of pUC19.

The MC approach is then used to generate an ensemble of conformations for a given slit height. The walk is initiated by randomly placing the first monomer between the confining walls. We assume a uniform distribution for the chain ends between the walls. Additional monomers are added via the scheme outlined above. If the chain crosses one of the two walls, the growth of that chain is terminated — this is counted as a disallowed conformation. Conversely, an allowed conformation is generated when all N steps are made with no disallowed moves.

As the size of the ensemble grows, the ratio of the allowed to total (allowed + disallowed) conformations approaches the ratio of the partition functions for confined to unconfined chains which leads to a direct calculation of the confinement free energy. For wall spacings of h between 5–2000, we use $N_{\text{try}} = 1 \times 10^8$ attempts but need to increase it for wall spacings of $h = 2, 3$, and 4 unit bond vectors in order to obtain sufficient successful attempts.

To investigate the effect of semiflexibility, these calculations were performed for polymers of varying persistence lengths, $\kappa = (0, 5, 10, 20)$, and lengths, $N = (50, 100, 200, 500)$. From these results, we find that the Casassa formula (Eq. 4 of

main text) contains a model-dependent prefactor, even considering its effect on R_g . The free-energy cost of semi-flexible chains decreases from the value predicted by Casassa's formula for a flexible chain as chain rigidity increases, reflecting the fact that a semi-flexible chain contains a diminished number of degrees of freedom and thus has fewer conformations eliminated by the walls. We find that this effect can be absorbed into a stiffness-dependent prefactor. For the case of our pUC19 model $N = 84$ and $\kappa = 5.0$, this prefactor is sufficiently close to unity (≈ 0.90) to be neglected in Figure 2.4 (main paper). The reduction in free-energy cost owes to semi-flexibility itself rather than simply a change in R_g : rescaling the flexible polymer into Kuhn beads with the same R_g gives results different from the semi-flexible case.

Dynamical simulations were performed with a standard coarse-grained, generic polymer methodology [113]. To model dsDNA, the width of the polymer is set to 5 nm and hence $\sigma = 5$ nm where σ is the bead size. Correspondingly, the Kuhn length is set to $L_K = 20\sigma$ to match the 100 nm Kuhn length of dsDNA. The polymer is built out of 183 beads to give a contour length of 1047 nm in agreement with that of pUC19.

In correspondence with the theory, an ideal polymer was constructed in which there are no excluded volume interactions between monomers that are non-adjacent along the polymer backbone. Neighboring monomers are prevented from overlapping by the Weeks-Chandler-Anderson (WCA) potential which is a shifted and truncated Lennard-Jones

interaction [114]. It is given by

$$U_{\text{WCA}}(r) = \begin{cases} 4\epsilon \left[\left(\frac{\sigma}{r}\right)^{12} - \left(\frac{\sigma}{r}\right)^6 \right] + \epsilon & \text{for } r < r_c \\ 0 & \text{for } r \geq r_c \end{cases} \quad (\text{A.7})$$

where ϵ is the characteristic energy, here set to $k_{\text{B}}T$, σ is the nominal monomer size, 5 nm, which is set in simulation units to 1, and r_c is the cut-off distance and is set to $2^{1/6}\sigma$. Monomers along the polymer are bonded together via a Finitely Extensible Nonlinear Elastic (FENE) potential:

$$U_{\text{FENE}}(r) = -\frac{1}{2}k_{\text{f}}r_0^2 \ln \left(1 - \frac{r^2}{r_0^2} \right). \quad (\text{A.8})$$

We follow the model of Kremer and Grest [115] and set $k_{\text{f}} = 30\epsilon/\sigma^2$ and $r_0 = 1.5\sigma$. As we require a semi-flexible polymer, backbone stiffness is implemented via a harmonic potential given by

$$U_{\text{bend}}(\theta) = \frac{1}{2}k_{\text{s}}(\theta - \theta_0)^2 \quad (\text{A.9})$$

where θ is the angle formed by three consecutive monomers along the polymer backbone, θ_0 is the equilibrium angle which is set to π , and k_{s} is the bending constant. For this potential, the Kuhn length is approximately equal to the bending constant: $L_{\text{K}}/\sigma \approx 2k_{\text{s}}/k_{\text{B}}T$. As discussed above, we set $k_{\text{s}} = 10k_{\text{B}}T$ and thus have a Kuhn length $\approx 20\sigma$ in the simulations. The simulated polymer contained $N = 183$ monomers.

The confining walls are implemented as continuous surfaces. Interactions between the

monomers and the walls are governed by the WCA potential as given above. Simulations are performed with the distance between the walls varying from $\tilde{h} = 2.5\text{--}50.0\sigma$. Due to the nature of the WCA interaction, the available space for the polymer will be $\sim \sigma$ less than this value. Likewise, as the theory corresponds to an infinitely thin polymer, the relevant height is this height minus the size of the simulation bead. Thus, the final simulation height used for plotting is $h = \tilde{h} - 2.0\sigma$.

As this work addresses static properties and not dynamics, hydrodynamics were not required in the simulations. For computational efficiency, we thus performed Langevin dynamics simulations in which the effects of the solvent are included implicitly in the equation of motion. This is achieved by adding a drag term and a random term to the standard molecular dynamics equation yielding

$$m\ddot{\vec{r}} = -\nabla U(\vec{r}) - \zeta\dot{\vec{r}} + \vec{R}(t). \quad (\text{A.10})$$

In this equation, $U(\vec{r})$ is the sum of the conservative potentials, ζ is the friction coefficient, and $\vec{R}(t)$ is a random number that satisfies

$$\langle \vec{R}(t) \rangle = 0 \quad (\text{A.11})$$

$$\langle \vec{R}(0) \cdot \vec{R}(t) \rangle = 2k_{\text{B}}T\zeta\delta(t) \quad (\text{A.12})$$

in accordance with the fluctuation dissipation theorem.

To obtain the confinement free energy from simulations, we followed the approach of

Dimitrov *et al.* [116] by calculating the average force on the walls due to the monomers, $f_{\text{conf}}(h)$. This is related to the confinement free energy by

$$f_{\text{conf}}(h) = -\frac{d}{dh}G_{\text{conf}}(h). \tag{A.13}$$

The free energy of confinement, G_{conf} , was calculated by numerically integrating the $f_{\text{conf}}(h)$ data. Simulations were performed from very tight confinement up to $h/L_K = 1.83$ and thus there is a numerical constant, G_0 , that must be added to G_{conf} . This was calculated using the Chen-Sullivan formula to equal $0.100 k_B T$. The simulation results for G_{conf} are shown in Fig 4 (main paper) together with the Monte Carlo simulations from the main text (Fig. 3).

Appendix B

Supplementary Information (SI): Single-particle Measurements of Size and Loading of Drug-delivery Lipid Nanoparticles

B.1 Comparisons with other sizing techniques

Convex Lens induced Confinement (CLiC) microscopy is a new technique for determining the size distribution of a population of nanoscopic objects, where the size of each member of the population is measured directly and independently. Our method adds to an evolving landscape of nano-characterization techniques, including single-molecule techniques such as AFM, Cryo-electron Microscopy (Cryo-TEM), Resistive Pulse Sensing (RPS) and optical tweezers. These join a suite of established bulk measurement techniques for particle sizing, such as flow-fractionation, size exclusion chromatography, centrifugation and light scattering techniques, including Dynamic Light Scattering (DLS), Nanoparticle Tracking Analysis (NTA) and Fluctuation Correlation Microscopy (FCM). Table [B.1](#) gives a summary of the typical

Methods	Typical detection lower-limit	Principle	Single molecule resolution	Solution	Long timescale observation
DLS	2 nm	Temporal intensity fluctuations of diffusing particles	yes	yes	no
NTA	30 nm	Tracking of diffusing particles	yes	yes	no
AFM	0.5 nm	Topographic map of immobilized particles	yes	no	yes
Cryo-TEM	2 nm	Electron transmission through immobilized particles	yes	no	yes
FCM	300 nm	Light scattering of flowing particles	yes	yes	no
RPS	40 nm	Conductivity of flowing particles	no	yes	no
CLiC imaging	1 nm	Tracking of confined diffusing particles	yes	yes	yes

Table B.1: Comparison of particle size characterization methods. Typical detection lower-limits and principles of DLS [117], NTA, AFM, Cryo-TEM, RPS [118], FCM [119], and CLiC imaging. CLiC is unique in providing single-molecule resolution, without tethers in solution, and long observation periods.

lower-limit of detection and the functioning principle of these methods, including whether their measurements are in solution or require surface immobilization, and the capacity for long-time detection.

The most commonly used technique to characterize particle size is DLS [16], which uses a coherent light source to create a fluctuating interference pattern due to Brownian motion changing the relative distance between particles [17]. The diffusion constant can be extracted from the decay of the autocorrelation function of these fluctuations, which reflects the time scale of particles moving relative to each other. Particle size

information is then obtained from diffusion constant and buffer viscosity, using the Einstein-Stokes relation. This technique has been used to measure the sizes of particles with sub-nanometer resolution [18].

However, the presence of large particles, even in small quantities, can skew the results and mask the underlying size distribution. Heterogeneity in particle size within a sample is challenging to quantify, and the indirect interpretation of size from DLS data can obscure results. [19] [20]. Therefore, single molecule measurements are required to have a better understanding of the size distribution of samples, and to quantify aggregates or different populations with distinct sizes.

NTA is able to measure the sizes of individual particles by imaging their scattering in unconfined solution. However, particles drift in and out of the focal plane of the microscope resulting in significant fluctuations in the scattering intensity [21], limiting the precision and accuracy of size measurements.

In AFM, the size and shape of immobilized particles can be estimated with sub nanometer resolution [22]. However, immobilization may affect the structural properties of the particles, inducing conformational changes and adding bias [23].

Cryo-TEM avoids both staining and fixation by rapidly freezing the particle suspension in liquid ethane [24], [25]. However, low throughput, complicated sample preparation protocols, and high cost are all limiting factors for this technique, although it is often used to complement DLS [26].

FCM is an indirect technique used to analyze single cells and particles in the sub-micrometer range [27]. The optical signal depends on both the size and refractive

index of the particle, and drops dramatically with reducing radius. This makes the detection of sub-wavelength particles challenging [28]. In RPS [29] since the aperture size must be comparable to the size of the nanoparticles, it poses limitations on the heterogeneity and size range of the sample [30]. Optical tweezers can be used to measure the size of a single nanoparticle, but with such low throughput that it would not be possible to construct a statistically significant distribution from hundreds or thousands of independent measurements.

DLS and NTA are both of particular interest for comparison with CLiC data, since - as with CLiC - these techniques both make direct measurements of diffusivity, and derive size distributions from Stokes-Einstein models relating diffusivity to size. This similarity in physical basis gives us an opportunity to compare a bulk measurement of an ensemble average to the average over an ensemble of directly measured microscopic states. In this paper we have demonstrated how to account for confinement in both the derivation of diffusivity from MSD, and of size from diffusivity by means of a modified Stokes-Einstein model. Our proof-of-principle measurements on polystyrene beads agree within 1 nm of the manufacturer's size characterizations as measured using electron microscopy (see Table B.2).

For more complex LNP samples, expectation value of our size distribution is significantly larger than that measured by DLS, which begs the question of which technique yields the 'correct' size characterization. CLiC is a more direct measurement of diffusivity, watching each particle diffuse. The ensemble-averaged size distribution measured by DLS depends on a model of autocorrelation times for scattering events

from a macroscopic population of particles, and is further removed from a direct diffusivity measurement.

Soft materials such as LNPs also have a more complex diffusive behavior arising from non-elastic degrees of freedom, and may require further and interesting modifications of the Stokes-Einstein relation, which assumes a hard sphere moving through a viscous medium. A soft particle requires a model of a viscous sphere moving in a medium of different viscosity.

The model needed to compute the confinement correction due to the influence of solid surfaces will also require a more complex treatment, which includes inelastic particle collision and surface charge interactions.

B.2 Particle detection, tracking and sizing

B.2.1 Pyramid approach to particle detection

To identify singly occupied micro-wells, our single-particle detection pipeline uses a Laplacian Pyramid [120] in a top-down scheme [121]. The algorithm computes the location of a single particle in a given frame. For computational efficiency, we use the Difference of Gaussian method to detect particles across multiple scales [122]. Provided with a series of images, the centroid locations are computed at each frame and then compiled. We then apply a threshold to reject videos if a particle was not detected in at least 85% of the frames. Finally, we manually inspect the selected wells, and eliminate any that have multiple occupants. As a result, pits containing only a single particle are

selected for the following analysis.

B.2.2 Single-particle tracking in confinement

To measure the size and intensity of single particles, we employed single-particle tracking (SPT) [96,97], and a mean-squared displacement (MSD) analysis adapted for a cylindrical geometry.

Gaussian fitting to single particles. Localization of single diffusing particles was aided by applying a Gaussian noise filter with a standard deviation σ equal to the diffraction limit,

$$\sigma = \frac{\Lambda}{2NA} \times \frac{M}{p}, \quad (\text{B.1})$$

where Λ is the fluorophore wavelength, NA is the numerical aperture, M is the magnification, and p is the on camera pixel size. The term $\frac{M}{p}$ scales σ from the object plane to the image plane and converts the units to pixels. This effectively reduces the noise smaller than the expected signal. The point spread function in each frame was then fit using two-dimensional Gaussian function $G(x, y)$ [98–100],

$$G(x, y) = Ae^{-\left(\frac{(x-x_0)^2}{2\sigma^2} + \frac{(y-y_0)^2}{2\sigma^2}\right)} + B, \quad (\text{B.2})$$

where the amplitude A , the background B , the variance σ^2 , and the particle's position (x_0, y_0) are left as fitting parameters. Eq. B.2 was used to determine the position of a particle in a single frame. A trajectory of the form, $\mathbf{r} = \{(x_1, y_1), (x_2, y_2), \dots, (x_N, y_N)\}$ was obtained by repeating this process for each successive frame.

MSD calculation from single particle tracking. Having the trajectories in this form, the mean-square displacements of each particle can be calculated. The empirical estimation ρ , of the true mean square displacement is defined to be [123]

$$\rho(n\Delta t) = \frac{1}{N-n} \sum_{i=1}^{N-n} (\mathbf{r}_{i+n} - \mathbf{r}_i)^2, \quad (\text{B.3})$$

$$n = 1, \dots, N-1,$$

where N is the total number of frames, \mathbf{r}_i is the i th position of the trajectory \mathbf{r} , and Δt is the exposure time. In this definition, every displacement of each discrete time interval is used to calculate the mean-square displacement estimation. One advantage of this MSD definition is it makes the early points more precise by averaging many displacements. The trade-off is that the displacement measurements are overlapped, introducing correlations between the MSD points [123]. However, this can be mitigated by choosing a lower number of fitting points.

Confined diffusion theory. A previously developed theoretical MSD under 2D circular confinement [79] was modified for curve fitting, including the effect of finite exposure time and shot noise as an offset [80]. The fitting model for the estimated MSD points given by Eq. B.3 is:

$$\text{MSD}(t) = O + r^2 \left(1 - 8 \sum_{m=1}^{\infty} \frac{e^{[-\alpha_{1m}^2 \frac{t}{\tau}]} }{\alpha_{1m}^2 (\alpha_{1m}^2 - 1)} \right), \quad (\text{B.4})$$

where O is the offset, a is the confinement radius, $\tau = \frac{r^2}{D}$ is the characteristic time scale, D is the diffusion coefficient, and α_{1m} is the m^{th} positive root of the derivative of the

Bessel function of the first kind. In practice, since the sum quickly converges, we only include the first 4 terms for curve fitting. Parameters D , O , and r were determined using non-linear least squares fitting.

Limiting cases of confined diffusion. Under confinement, the MSD(t) is expected to saturate at a value proportional to an area accessible for diffusion, i.e., $\text{MSD}(t) \approx r^2$, in the limit $t \rightarrow \infty$ [123]. In the short time limit $t \ll \tau$, the exponential in the second term of Eq. S4 can be expanded in a power series, and the MSD(t) is reduced to $4Dt$ [79], the free 2D-diffusion MSD. A typical MSD curve with data given by Eq. S3 and fit using Eq. S4 is shown in Figure 3.1 D.

B.2.3 Corrections for size measurement under parallel planes of confinement

To correct for the effect of confinement on the measured diffusion coefficients, we performed a series of experiments as a function of micro-well depth d_w (see Figure B.1(A), (B) and (C)). We then fit the data to a theoretical model given by [81, 101]:

$$D_{\parallel} = \frac{k_B T}{6\pi\eta a} \left(1 - 1.004 \left(\frac{a}{z} \right) + 0.418 \left(\frac{a}{z} \right)^3 + 0.21 \left(\frac{a}{z} \right)^4 - 0.169 \left(\frac{a}{z} \right)^5 + O \left(\frac{a}{z} \right)^6 \right). \quad (\text{B.5})$$

where $D_{\parallel} = D_0 \lambda^{-1}$ is the of measured diffusivity of a particle confined between two parallel planes separated by a distance d_w , k_B is the Boltzmann constant, T is the temperature, η is kinetic viscosity of the solution, $a = d_0/2$ is the hydrodynamic radius

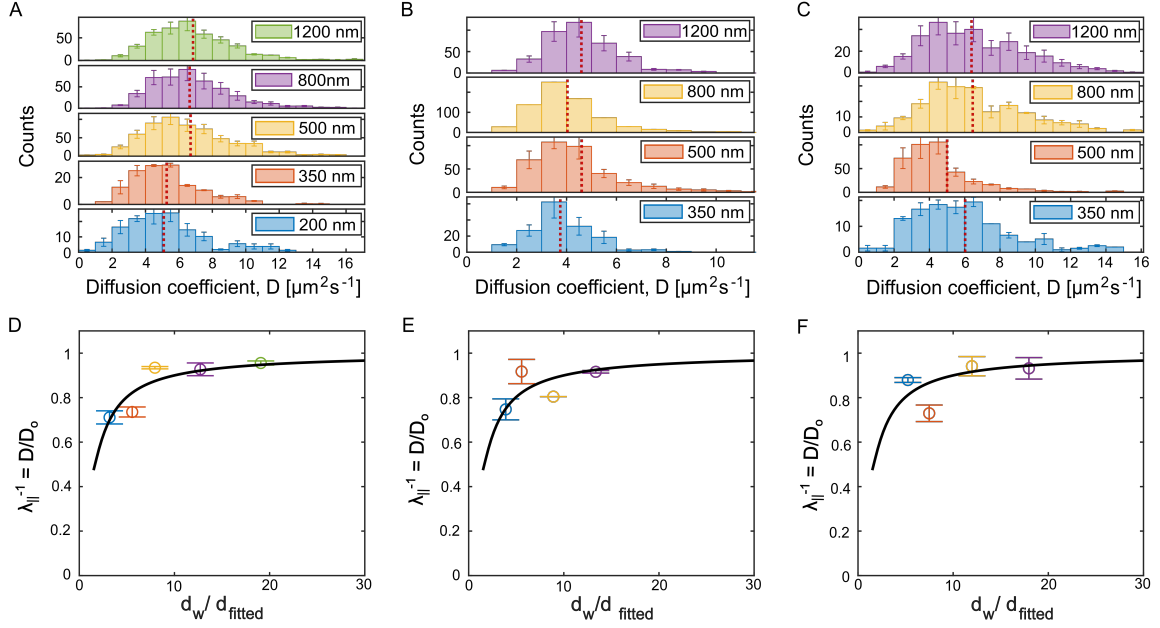


Figure B.1: Diffusion coefficient measurements at varying confinement depth, for (A) unloaded LNPs (B) siRNA loaded LNPs and (C) control LNPs with no ionizable lipids. For each sample type the measurements were repeated at 4 or 5 different confinement depths ($d_w = [200, 350, 500, 800, 1200 \text{ nm}]$). Each bar plot - except the second row in (B) - shows an average of 2 to 3 experiments, i.e. each bin and error bar are obtained by averaging the corresponding histogram bins from individual experiments. The red dashed lines are also obtained from averaging the mean values of individual experiments. (C), (D) and (E) show fitting of these mean values to the theoretical model, to obtain the unconfined diffusivity of the different nanoparticles, with d_0 as the fitting parameter.

given by the Stokes-Einstein equation, $\lambda_{||}$ is a correction factor for diffusivity under confinement (eq. 2), and $z = d_w/2$ is the distance to the mid-plane. The equation was re-written in terms of d_0 and d_w , and d_0 was used as the fitting parameter. We assumed the $O\left(\frac{a}{z}\right)^6$ term to be negligible in our fitting. We used Eq. 1 to calculate D_0 and hence $\lambda_{||}$ values as a function of d_w (black lines in Figures S1 (D), (E) and (F)).

This fitting procedure uses information from measurements at all confinement depths to yield a particle size that best fits all the data. Results for beads are shown in Figure 3.1, and those for LNPs are shown in Figure B.1. Table B.2 gives a summary of all

the results. Size distributions in Figures 3.2, 3.3 and 3.6 – which were also measured in 500nm deep pits – were rescaled using $\lambda(500nm)$ values in this table, for corresponding particle formulations, i.e., we used λ values obtained from confinement experiments with corresponding formulations. However, for the case of pH 4 unloaded LNPs we were unable to obtain experiments with good statistics for the confinement measurements, due to low SNR obtained with a 40x objective. Hence, we used the correction factor measured with pH 7.4 samples, as their size distributions overlap significantly.

B.3 LNP cargo-loading distributions

B.3.1 Photobleaching measurements

Figure 4 shows typical photobleaching traces ((A), (D) and (G)) constructed from tracking the particles' fluorescence intensities. The intensity trace, measured in photoelectrons, is given by the amplitude of the fitted two-dimensional Gaussian obtained during tracking (Eq. S2). A particle labelled with multiple fluorophores will appear to have discrete decreasing steps in intensity, corresponding to independent photobleaching events.

The steps were then detected using a two-sample t-test algorithm for edge detection (see Chen et al. [88] for details). Briefly, an intensity trace is iteratively scanned for potential bleaching steps, until no statistically significant step can be added. The algorithm can be used with or without assuming constant variance in the intensity trace. Additionally, the significance value in the statistical test is set by an empirically

	d_w [nm]	200	350	500	800	1200
polystyrene NPs in Di Water	λ^{-1}	0.760	0.860	0.902	0.938	0.959
	$\langle d \rangle$ [nm]	62 ± 2	45 ± 2	47 ± 1	48 ± 2	43 ± 1
	d_{kde} [nm]	64 ± 2	49 ± 1	49 ± 6	49 ± 1	46 ± 3
	Fitted d_0 [nm]	49 ± 6				
	EM d_0 [nm]	48 ± 6				
	DLS d_0 [nm]	43.5 ± 0.4				
Unloaded LNP, in 1xPBS pH7.4 NPs	λ^{-1}	0.699	0.822	0.875	0.921	0.947
	$\langle d \rangle$ [nm]	61 ± 7	70 ± 1	54 ± 1	61 ± 2	59 ± 2
	d_{kde} [nm]	62 ± 2	70 ± 2	59 ± 4	63 ± 2	62 ± 6
	Fitted d_0 [nm]	63 ± 4				
	DLS d_0 [nm]	46.3 ± 0.4				
	loaded LNP, in 1xPBS pH7.4	λ^{-1}	-	0.750	0.822	0.888
$\langle d \rangle$ [nm]		-	96 ± 10	89 ± 5	100	88 ± 2
d_{kde} [nm]		-	90 ± 4	81 ± 4	99	91 ± 1
Fitted d_0 [nm]		90 ± 10				
DLS d_0 [nm]		61.3 ± 0.9				
Control LNP, in 1xPBS pH7.4		λ^{-1}	-	0.812	0.867	0.916
	$\langle d \rangle$ [nm]	-	60 ± 7	89 ± 3	58 ± 3	60 ± 7
	d_{kde} [nm]	-	68 ± 3	79 ± 4	65 ± 3	68 ± 3
	Fitted d_0 [nm]	67 ± 9				
	DLS d_0 [nm]	49.3 ± 2.9				

Table B.2: Summary of fitting for diffusion coefficients measurements under parallel planes confinement. λ^{-1} values are obtained from fitted theoretical model in Figure B.1 (black lines in (D), (E) and (F)). $\langle d \rangle$ are particle sizes calculated from the mean diffusion coefficient (red lines in the Diffusion coefficient distributions in Figures 1E, S1A, S1B and S1C). d_{kde} is the peak of fitted kernel density functions to the size distributions (Figure 1F). They are also shown by black dashed lines in Figure 3.1. Fitted a are the fitting parameters in equation 5 – for the different cases – and they correspond to the diffusion coefficients (D_0) far away from the confining planes.

determined threshold. For our measurements, we used the option of no assumed constant variance and the threshold was set to 2.

The resulting distributions of the final steps (Figure 4(b), (E) and (H)) were fit with kernel density estimation - to find (and avoid overestimating) the unit step size ΔI of a single photobleaching event. We used MATLAB's `distfit` fitting function for kernel

density fitting and obtained the maximum likelihood step intensity in the distribution from the mode of the fitted distribution (Figure 4).

B.4 Simulation of confined particles

B.4.1 Optimizing Imaging Parameters: Quantifying Bias and Variance

To accurately extract the diffusive trajectories using SPT, optimal imaging parameters such as exposure time and laser power need to be carefully chosen. To this end, we built simulations to advise the choice of these parameters for data collection. Additionally, the simulations were used to find an optimal fitting scheme for extracting diffusion coefficients. Specifically, each diffusing particle was simulated as a 2D Gaussian intensity profile under circular well confinement with a known diffusion coefficient and signal to noise ratio (SNR). We then analyzed these particle trajectories to determine the expected variance and bias of the measured diffusion coefficients before correcting for hydrodynamic effects.

Random walk simulation. The random walk trajectory \mathbf{r} was simulated by drawing step sizes from a zero mean normal distribution with a standard deviation of $\sqrt{2Dt_{exp}}$, where D is the diffusion coefficient of the simulated particle and t_{exp} is the exposure time. The initial particle position was chosen to be at the center of the micro-well. A reflecting boundary condition at the edge of the well was used.

Incorporating the point spread function and noise. To simulate motion blur

resulting from the finite exposure time, each frame is composed of multiple sub-frames, where each sub-frame is formed by placing a Gaussian intensity profile at the location of the particle. The spatial intensity profile $I(x, y)$, is related to the point spread function (PSF) of the microscope by:

$$I(x, y) = I_0 e^{-\left(\frac{(x-x_n)^2 + (y-y_n)^2}{2\omega_0^2}\right)} \quad (\text{B.6})$$

where ω_0 is the PSF size which was calculated with the fluorophore wavelength, the numerical aperture, and the pixel size of the system, and I_0 is the peak intensity which was also calculated with the parameters of the optical system. For real experimental video data with motion blur, the number of sub-frames is infinite as a result of the continuous diffusion process. For our simulations the number of sub-frames was chosen heuristically to be 50. This was determined to be sufficient for obtaining blurring effects similar to the experimental videos, yet small enough for computational efficiency. Camera shot noise was simulated and added to each frame, pixel by pixel, with each pixel intensity value being drawn from a Poisson distribution whose mean is equal to the value of the PSF at that location. The same procedure was done to add EM register noise.

Comparing simulation to experiment. Figure 3.1 C validates that the profile of the simulation movie is comparable to the real experimental movie. The chosen frames have signal-to-noise ratios (SNR) and signal-to-background ratios (SBR) in close agreement with each other. Figure 3.1 C (ii and iv) show the fitted amplitude A (147 photoelectrons for experiment and 140 photoelectrons for simulations) of the Gaussian

fit function Eq. B.2, the noise of the image N (19 photoelectrons for experiment and 23 photoelectrons for simulations), and the fitted PSF size σ_{PSF} (1.9 for both experiment and simulations). Together, they show simulations can be used to closely match experiments given the characteristics of the experimental data. For each simulated movie, the trajectory is then recorded and used to calculate the MSD.

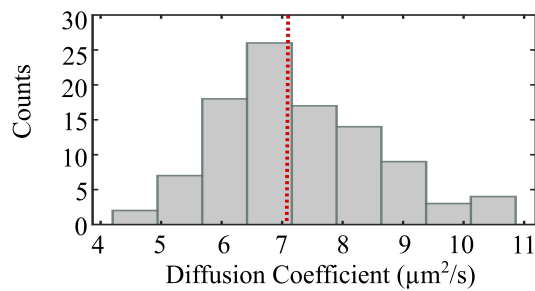


Figure B.2: Simulation validation. Extracted diffusion coefficients are seen to be normally distributed with a mean diffusion coefficient of $\langle D \rangle = 7.3 \mu\text{m}^2/\text{s}$ with a standard error of $\sigma \langle D \rangle = 0.1 \mu\text{m}^2/\text{s}$. Using 100 simulations, a systematic bias ($\sim 4\%$) was found for the given imaging parameters.

As an example, Figure B.2 shows the distribution of diffusion coefficients extracted from 100 simulations with a true diffusion coefficient of $7 \mu\text{m}^2/\text{s}$. A sample MSD curve of a simulated particle - from this distribution - is also shown in Figure 3.1 D of the main paper. Each simulation assumed the following imaging parameters which matched experimental settings that were used to train the simulations: 30 mW objective power, a 30 ms exposure time, and consisted of 500 frames. MSD points calculated from Eq. B.3 were then fit using Eq. B.4. In addition, we found that the fitting was robust independent of the number of fitting points. The average diffusion coefficient was determined to be $7.3 \pm 0.1 \mu\text{m}^2/\text{s}$ indicating a systematic error of $\sim 4\%$. This simulation study shows that we can extract the diffusion coefficient of a particle, with a small systematic error. It is also

worth noting that there is a variance (note the width of the histogram) associated with our measurement, even though the underlying population is a delta function. Therefore, for even a monodisperse sample, we expect the measured size distribution to have some measurement error associated with it. How the bias and variance depend on the input parameters and fitting scheme is investigated in the following sections.

Establishing bounds on SNR for quantitative size measurements.

Simulations were used as a tool to guide experiments, by suggesting the optimal exposure time and laser power. First, simulations were used to find a lower bound on the SNR required to minimize localization errors incurred from tracking. We found that the mean squared error between the localized position and the underlying generated trajectory was minimized for a SNR of approximately 2 or greater. Using simulations, the SNR was measured as a function of exposure time for different laser intensity. The SNR is defined as:

$$SNR = \frac{I_{Gaussian}}{Std(Image)}, \quad (B.7)$$

where $I_{Gaussian}$ is the fitted amplitude of the Gaussian function and $Std(Image)$ is the standard deviation of the entire image. From experiments, it was observed that the SNR increases as exposure time gets longer. However, for very long exposure times the SNR plateaus to a constant value. To investigate this behavior, we simulated movies with higher laser power settings and found there is one exposure time at which the SNR is maximized. The existence of such an optimal value is indeed expected. At a

low exposure time, low number of photons reach the detector and shot noise dominates, while at a high exposure time, the photons emitted are smeared across a larger area on the detector, causing the signal to decrease.

Simulations to investigate bias and variance for obtaining more robust results. For a given combination of diffusion coefficient, micro-well radius, and laser power, the choice of exposure time and the number of fitting points is crucial to minimize systematic bias and variance of the diffusivity measurement. An exposure time that is too long results in higher localization error, increasing the systematic bias and variance for a broad range of fitting points.

To isolate errors intrinsic to the model itself, we used the true trajectories generated by the random walk for calculating the MSD points, removing tracking errors. For a fixed exposure time, the systematic bias is observed to increase with increasing diffusion coefficient, suggesting that the choice of exposure time is crucial to accurately determine the diffusion coefficients.

Furthermore, the systematic bias depends on both the approximate time required for the MSD curve to saturate (characteristic timescale), $\tau = \frac{r^2}{D}$, and the exposure time t_{exp} . The ratio $\frac{\tau}{t_{exp}}$ is approximately the number of frames before saturation. As D increases, the ratio $\frac{\tau}{t_{exp}}$ and the number of MSD points before saturation decreases. This under-sampling of the MSD curve in the linear regime, ultimately results in poor fitting by non-linear least-squares, adding a systematic bias to the measured diffusion coefficients. Therefore, to reduce the bias the exposure times used should be decreased to make $\frac{\tau}{t_{exp}}$ sufficiently large. Additionally, the number of fitting points f was shown to add little

variation to the final results in the range $\frac{\tau}{t_{exp}} < f < \frac{N}{2}$, where N is the total number of frames used to compute the MSD estimator (Eq. S3).

To investigate the variance of measured diffusion coefficients, sets of simulated movies were generated with an increasing number of frames. For varying diffusion coefficients the variance decreases as the number of frames increases. Therefore, to minimize the variance of our measurements, we require movies to be as long as possible. However, experimentally this can be quite challenging as the fluorophores undergo photobleaching. As such, the non-zero variance will put a lower bound on the ability to measure heterogeneity.

Bibliography

- [1] J. S. Leith, A. Kamanzi, D. Sean, D. Berard, A. C. Guthrie, C. M. McFaul, G. W. Slater, H. W. de Haan, and S. R. Leslie, “Free energy of a polymer in slit-like confinement from the odijk regime to the bulk,” *Macromolecules*, vol. 49, no. 23, pp. 9266–9271, 2016.
- [2] P. F. McKay, K. Hu, A. K. Blakney, K. Samnuan, J. C. Brown, R. Penn, J. Zhou, C. R. Bouton, P. Rogers, K. Polra, *et al.*, “Self-amplifying rna sars-cov-2 lipid nanoparticle vaccine candidate induces high neutralizing antibody titers in mice,” *Nature communications*, vol. 11, no. 1, pp. 1–7, 2020.
- [3] D. Witzigmann, J. A. Kulkarni, J. Leung, S. Chen, P. R. Cullis, and R. van der Meel, “Lipid nanoparticle technology for therapeutic gene regulation in the liver,” *Advanced Drug Delivery Reviews*, 2020.
- [4] C. E. Thomas, A. Ehrhardt, and M. A. Kay, “Progress and problems with the use of viral vectors for gene therapy,” *Nature Reviews Genetics*, vol. 4, no. 5, pp. 346–358, 2003.
- [5] N. Bessis, F. GarciaCozar, and M. Boissier, “Immune responses to gene therapy vectors: influence on vector function and effector mechanisms,” *Gene therapy*, vol. 11, no. 1, pp. S10–S17, 2004.

- [6] H. Yin, R. L. Kanasty, A. A. Eltoukhy, A. J. Vegas, J. R. Dorkin, and D. G. Anderson, “Non-viral vectors for gene-based therapy,” *Nature Reviews Genetics*, vol. 15, no. 8, pp. 541–555, 2014.
- [7] P. R. Cullis and M. J. Hope, “Lipid nanoparticle systems for enabling gene therapies,” *Molecular Therapy*, vol. 25, no. 7, pp. 1467–1475, 2017.
- [8] S. C. Semple, A. Akinc, J. Chen, A. P. Sandhu, B. L. Mui, C. K. Cho, D. W. Sah, D. Stebbing, E. J. Crosley, E. Yaworski, *et al.*, “Rational design of cationic lipids for sirna delivery,” *Nature biotechnology*, vol. 28, no. 2, pp. 172–176, 2010.
- [9] A. K. Leung, Y. Y. Tam, S. Chen, I. M. Hafez, and P. R. Cullis, “Microfluidic mixing: A general method for encapsulating macromolecules in lipid nanoparticle systems,” *J. Phys. Chem. B*, vol. 119, no. 28, pp. 8698–8706, 2015.
- [10] N. Pardi, S. Tuyishime, H. Muramatsu, K. Kariko, B. L. Mui, Y. K. Tam, T. D. Madden, M. J. Hope, and D. Weissman, “Expression kinetics of nucleoside-modified mrna delivered in lipid nanoparticles to mice by various routes,” *Journal of Controlled Release*, vol. 217, pp. 345–351, 2015.
- [11] J. A. Kulkarni, J. L. Myhre, S. Chen, Y. Y. C. Tam, A. Danescu, J. M. Richman, and P. R. Cullis, “Design of lipid nanoparticles for in vitro and in vivo delivery of plasmid dna,” *Nanomedicine: Nanotechnology, Biology and Medicine*, vol. 13, no. 4, pp. 1377–1387, 2017.

- [12] S. Patel, R. C. Ryals, K. K. Weller, M. E. Pennesi, and G. Sahay, "Lipid nanoparticles for delivery of messenger rna to the back of the eye," *Journal of Controlled Release*, vol. 303, pp. 91–100, 2019.
- [13] N. MAURER and J. KULKARNI, "Recent advances in lipid nanoparticle-mediated mrna therapy," *AMERICAN PHARMACEUTICAL REVIEW*, vol. 22, no. 5, 2019.
- [14] J. A. Kulkarni, D. Witzigmann, J. Leung, Y. Y. C. Tam, and P. R. Cullis, "On the role of helper lipids in lipid nanoparticle formulations of sirna," *Nanoscale*, vol. 11, no. 45, pp. 21733–21739, 2019.
- [15] M. Jayaraman, S. M. Ansell, B. L. Mui, Y. K. Tam, J. Chen, X. Du, D. Butler, L. Eltepu, S. Matsuda, J. K. Narayanannair, *et al.*, "Maximizing the potency of sirna lipid nanoparticles for hepatic gene silencing in vivo," *Angewandte Chemie*, vol. 124, no. 34, pp. 8657–8661, 2012.
- [16] M. Hartmann, "Light scattering by small particles. von hc vande hulst. new york: dover publications, inc. 1981. paperback, 470 s., 103 abb. und 46 tab., us \$7.50," *Acta Polymerica*, vol. 35, no. 4, pp. 338–338, 1984.
- [17] B. J. Berne and R. Pecora, *Dynamic light scattering: with applications to chemistry, biology, and physics*. Courier Corporation, 2000.
- [18] M. D. M. F.K. McNeil-Watson, "Measuring sub nanometre sizes using dynamic light scattering," *J. Nanoparticle Res.*, vol. 10, p. 823–829, 2008.

- [19] J. D. Nickels, J. Atkinson, E. Papp-Szabo, C. Stanley, S. O. Diallo, S. Perticaroli, B. Baylis, P. Mahon, G. Ehlers, J. Katsaras, *et al.*, “Structure and hydration of highly-branched, monodisperse phytoglycogen nanoparticles,” *Biomacromolecules*, vol. 17, no. 3, pp. 735–743, 2016.
- [20] E. A. A. C. T. R. Nieuwland, “Optical and non-optical methods for detection and characterization of microparticles and exosomes,” *J. Thromb. Haemost.*, vol. 8, p. 2596–2607, 2010.
- [21] E. A. A. C. T. R. Nieuwland, “Particle size distribution of exosomes and microvesicles determined by transmission electron microscopy, flow cytometry, nanoparticle tracking analysis,” *J. Thromb. Haemost.*, vol. 12, p. 1182–1192, 2014.
- [22] C. G. G. Binnig, C.F. Quate, “Phys. rev. lett.,” *Atomic Force Microscope*, vol. 56, no. 9, p. 930–933, 1986.
- [23] T. K. L. Montelius and L. Samuelson, “Applied physics letters,” *Applied Physics Letter*, vol. 66, no. 26, p. 3627, 1995.
- [24] C. S. M. Kyte, “A precision cryostat design for manual and semi- automated cryo-plunge instruments,” *Rev. Sci. Instrum.*, vol. 87, 2016.
- [25] J. M. J. J. A. P.Schultz, “Cryo-electron microscopy of vitrified specimens,” *Q. Rev. Biophys.*, vol. 21, p. 129–228, 1988.
- [26] R. M. C. S. N.A. Ranson, “An introduction to sample preparation and imaging by cryo-electron microscopy for structural biology,” *Methods.*, vol. 100, pp. 3–15, 2016.

- [27] C. D. S. C. K. M. A.F. Hill, “Techniques used for the isolation and characterization of extracellular vesicles: Results of a worldwide survey, j. extracell. vesicles,” *J. Extracell. Vesicles.*, vol. 5, 2016.
- [28] A. G. Y. Y. A. Nalbant, “Optical and surface plasmonic approaches to characterize extracellular vesicles. a review,” *Anal. Chim. Acta.*, vol. 1005, p. 1–15, 2017.
- [29] R. de Blois and C. Bean, “Counting and sizing of submicron particles by the resistive pulse technique,” *Rev. Sci. Instrum.*, vol. 41, 1970.
- [30] H. O. T. M. J. C. M. F. Höök, “Bioinspired, nanoscale approaches in contemporary bioanalytics (review),” *Biointerphases.*, vol. 13, 2018.
- [31] T. Odijk, “Theory of lyotropic polymer liquid crystals,” *Macromolecules*, vol. 19, no. 9, pp. 2313–2329, 1986.
- [32] J. Z. Chen and D. Sullivan, “Free energy of a wormlike polymer chain confined in a slit: crossover between two scaling regimes,” *Macromolecules*, vol. 39, no. 22, pp. 7769–7773, 2006.
- [33] E. F. Casassa and Y. Tagami, “An equilibrium theory for exclusion chromatography of branched and linear polymer chains,” *Macromolecules*, vol. 2, no. 1, pp. 14–26, 1969.
- [34] D. J. Berard, F. Michaud, S. Mahshid, M. J. Ahamed, C. M. J. McFaul, J. S. Leith, P. Bérubé, R. Sladek, W. Reisner, and S. R. Leslie, “Convex lens-induced nanoscale templating,” *Proc Natl Acad Sci U S A*, vol. 111, pp. 13295–300, Sep 2014.

- [35] P. S. Doyle, J. Bibette, A. Bancaud, and J.-L. Viovy, “Self-assembled magnetic matrices for dna separation chips,” *Science*, vol. 295, p. 2237, Mar 2002.
- [36] E. Y. Chan, N. M. Goncalves, R. A. Haeusler, A. J. Hatch, J. W. Larson, A. M. Maletta, G. R. Yantz, E. D. Carstea, M. Fuchs, G. G. Wong, S. R. Gullans, and R. Gilmanshin, “Dna mapping using microfluidic stretching and single-molecule detection of fluorescent site-specific tags,” *Genome Res*, vol. 14, pp. 1137–46, Jun 2004.
- [37] S. K. Das, M. D. Austin, M. C. Akana, P. Deshpande, H. Cao, and M. Xiao, “Single molecule linear analysis of dna in nano-channel labeled with sequence specific fluorescent probes,” *Nucleic Acids Res*, vol. 38, p. e177, Oct 2010.
- [38] E. T. Dimalanta, A. Lim, R. Runnheim, C. Lamers, C. Churas, D. K. Forrest, J. J. de Pablo, M. D. Graham, S. N. Coppersmith, S. Goldstein, and D. C. Schwartz, “A microfluidic system for large dna molecule arrays,” *Anal Chem*, vol. 76, pp. 5293–301, Sep 2004.
- [39] H. Cao, Z. Yu, J. Wang, J. O. Tegenfeldt, R. H. Austin, E. Chen, W. Wu, and S. Y. Chou, “Fabrication of 10 nm enclosed nanofluidic channels,” *Applied Physics Letters*, vol. 81, no. 1, pp. 174–176, 2002.
- [40] E. Y. Chan, N. M. Goncalves, R. A. Haeusler, A. J. Hatch, J. W. Larson, A. M. Maletta, G. R. Yantz, E. D. Carstea, M. Fuchs, G. G. Wong, S. R. Gullans, and R. Gilmanshin, “Dna mapping using microfluidic stretching and single-

- molecule detection of fluorescent site-specific tags,” *Genome Research*, vol. 14, no. 6, pp. 1137–1146, 2004.
- [41] K. Jo, D. M. Dhingra, T. Odijk, J. J. de Pablo, M. D. Graham, R. Runnheim, D. Forrest, and D. C. Schwartz, “A single-molecule barcoding system using nanoslits for dna analysis,” *Proceedings of the National Academy of Sciences*, vol. 104, no. 8, pp. 2673–2678, 2007.
- [42] S. M. Stavis, J. Geist, M. Gaitan, L. E. Locascio, and E. A. Strychalski, “Dna molecules descending a nanofluidic staircase by entropophoresis,” *Lab Chip*, vol. 12, pp. 1174–1182, 2012.
- [43] T. Odijk, “The statistics and dynamics of confined or entangled stiff polymers,” *Macromolecules*, vol. 16, no. 8, pp. 1340–1344, 1983.
- [44] A. R. Klotz, L. Duong, M. Mamaev, H. W. de Haan, J. Z. Y. Chen, and W. W. Reisner, “Measuring the confinement free energy and effective width of single polymer chains via single-molecule tetris,” *Macromolecules*, vol. 48, no. 14, pp. 5028–5033, 2015.
- [45] E. F. Casassa, “Equilibrium distribution of flexible polymer chains between a macroscopic solution phase and small voids,” *Journal of Polymer Science Part B: Polymer Letters*, vol. 5, no. 9, pp. 773–778, 1967.
- [46] T. Burkhardt, “Free energy of a semiflexible polymer in a tube and statistics of a randomly-accelerated particle,” *Journal of Physics A*, vol. 30, pp. L167–L172, 1997.

- [47] P. G. De Gennes, *Scaling Concepts in Polymer Physics*. Cornell University Press: Ithaca, NY, 1979.
- [48] D. R. Tree, A. Muralidhar, P. S. Doyle, and K. D. Dorfman, “Is dna a good model polymer?,” *Macromolecules*, vol. 46, no. 20, pp. 8369–8382, 2013.
- [49] Y. Wang, G. H. Peters, F. Y. Hansen, and O. Hassager, “Equilibrium partitioning of macromolecules in confining geometries: Improved universality with a new molecular size parameter,” *The Journal of chemical physics*, vol. 128, no. 12, p. 124904, 2008.
- [50] D. R. Tree, W. F. Reinhart, and K. D. Dorfman, “The odijk regime in slits,” *Macromolecules*, vol. 47, no. 11, pp. 3672–3684, 2014.
- [51] W. Reisner, K. J. Morton, R. Riehn, Y. M. Wang, Z. Yu, M. Rosen, J. C. Sturm, S. Y. Chou, E. Frey, and R. H. Austin, “Statics and dynamics of single dna molecules confined in nanochannels,” *Phys. Rev. Lett.*, vol. 94, p. 196101, May 2005.
- [52] D. J. Bonthuis, C. Meyer, D. Stein, and C. Dekker, “Conformation and dynamics of dna confined in slitlike nanofluidic channels,” *Phys. Rev. Lett.*, vol. 101, p. 108303, Sep 2008.
- [53] J. Tang, S. L. Levy, D. W. Trahan, J. J. Jones, H. G. Craighead, and P. S. Doyle, “Revisiting the conformation and dynamics of dna in slitlike confinement,” *Macromolecules*, vol. 43, no. 17, pp. 7368–7377, 2010.

- [54] P. Cifra, “Weak-to-strong confinement transition of semi-flexible macromolecules in slit and in channel,” *The Journal of Chemical Physics*, vol. 136, no. 2, pp. –, 2012.
- [55] L. Dai, J. J. Jones, J. R. C. van der Maarel, and P. S. Doyle, “A systematic study of dna conformation in slitlike confinement,” *Soft Matter*, vol. 8, pp. 2972–2982, 2012.
- [56] S. R. Leslie, A. P. Fields, and A. E. Cohen, “Convex lens-induced confinement for imaging single molecules,” *Anal Chem*, vol. 82, pp. 6224–9, Jul 2010.
- [57] D. Berard, C. M. J. McFaul, J. S. Leith, A. K. J. Arsenault, F. Michaud, and S. R. Leslie, “Precision platform for convex lens-induced confinement microscopy,” *Rev. Sci. Instrum.*, vol. 84, p. 103704, 2013.
- [58] I. Teraoka, *Polymer Solutions: an Introduction to Physical Properties*. John Wiley: New York, NY, 2002.
- [59] M. J. Ahamed, S. Mahshid, D. J. Berard, F. Michaud, R. Sladek, W. W. Reisner, and S. R. Leslie, “Continuous confinement fluidics: Getting lots of molecules into small spaces with high fidelity,” *Macromolecules*, vol. 49, no. 7, pp. 2853–2859, 2016.
- [60] I. F. Sbalzarini and P. Koumoutsakos, “Feature point tracking and trajectory analysis for video imaging in cell biology,” *Journal of structural biology*, vol. 151, no. 2, pp. 182–195, 2005.

- [61] B. Shi, Y. K. Shin, A. A. Hassanali, and S. J. Singer, "Dna binding to the silica surface," *The Journal of Physical Chemistry B*, vol. 119, no. 34, pp. 11030–11040, 2015.
- [62] P. Cifra and T. Bleha, "Simulations of partitioning in size exclusion chromatography," *International Journal of Polymer Analysis and Characterization*, vol. 6, no. 6, pp. 509–520, 2001.
- [63] P. Cifra and T. Bleha, "Partition coefficients and the free energy of confinement from simulations of nonideal polymer systems," *Macromolecules*, vol. 34, no. 3, pp. 605–613, 2001.
- [64] V. Torchilin, "Multifunctional nanocarriers," *Multifunctional nanocarriers*, vol. 58, pp. 1532–55, 2006.
- [65] A. Puri, K. Loomis, B. Smith, J. Lee, A. Yavlovich, E. Heldman, and R. Blumenthal, "Lipid-based nanoparticles as pharmaceutical drug carriers: From concepts to clinic," *Critical reviews in therapeutic drug carrier systems*, vol. 26, pp. 523–80, 01 2009.
- [66] M. H. P. Cullis, "Lipid nanoparticles systems for enabling gene therapies," *Molecular Therapy*, vol. 25, pp. 1467–1475, 2017.
- [67] R. v. d. M. A. Kulkarni, P. Cullis, "Lipid nanoparticles enabling gene therapies: From concepts to clinical utility," *Nucleic Acid Therapeutics*, vol. 28, no. 3, pp. 146–157, 2018.

- [68] D. S. Goodsell, *Bionanotechnology: lessons from nature*. John Wiley & Sons, 2004.
- [69] A. M. Reichmuth, M. A. Oberli, A. Jaklenec, R. Langer, and D. Blankschtein, “mrna vaccine delivery using lipid nanoparticles,” *Therapeutic Delivery*, vol. 7, pp. 319–34, 2016.
- [70] S. Patel, R. C. Ryals, K. K. Weller, M. E. Pennesi, and G. Sahay, “Lipid nanoparticles for delivery of messenger rna to the back of the eye,” *J. Control. Release*, vol. 303, pp. 99–100, 2019.
- [71] H. Lv, S. Zhang, B. Wang, S. Cui, and J. Yan, “Toxicity of cationic lipids and cationic polymers in gene delivery,” *J. Control Release*, vol. 114, no. 1, pp. 100–109, 2006.
- [72] D. Berard, C. M. J. McFaul, J. S. Leith, A. K. J. Arsenault, F. Michaud, and S. R. Leslie, “Precision platform for convex lens-induced confinement microscopy,” *Rev. Sci. Instrum.*, vol. 84, p. 103704, 2013.
- [73] D. J. Berard, M. Shayegan, F. Michaud, G. Henkin, S. Scott, and S. Leslie, “Formatting and ligating biopolymers using adjustable nanoconfinement,” *Applied Physics Letters*, vol. 109, no. 3, p. 033702, 2016.
- [74] G. Henkin, D. Berard, F. Stabile, M. Shayegan, J. S. Leith, and S. R. Leslie, “Manipulating and visualizing molecular interactions in customized nanoscale spaces,” *Analytical chemistry*, vol. 88, no. 22, pp. 11100–11107, 2016.

- [75] S. Scott, Z. M. Xu, F. Kouzine, D. J. Berard, C. Shaheen, B. Gravel, L. Saunders, A. Hofkirchner, C. Leroux, J. Laurin, D. Levens, C. Benham, and S. Leslie, “Visualizing structure-mediated interactions in supercoiled dna molecules,” *Nucleic acids research*, vol. 46, no. 9, pp. 4622–4631, 2018.
- [76] S. Scott, C. Shaheen, B. McGuinness, K. Metera, F. Kouzine, D. Levens, C. Benham, and S. Leslie, “Single-molecule visualization of the effects of ionic strength and crowding on structure-mediated interactions in supercoiled dna molecules,” *Nucleic acids research*, vol. 47, no. 12, pp. 6360–6368, 2019.
- [77] M. Shayegan, R. Tahvildari, K. Metera, L. Kisley, S. W. Michnick, and S. R. Leslie, “Probing inhomogeneous diffusion in the microenvironments of phase-separated polymers under confinement,” *Journal of the American Chemical Society*, vol. 141, no. 19, pp. 7751–7757, 2019.
- [78] “Life technologies. fluospheres fluorescent color kit, carboxylate-modified microspheres, 0.04 um *5% solids*. catalog number = f-10720.” https://assets.thermofisher.com/TFS-Assets/LSG/certificate/Certificates%20of%20Analysis%1241418_F10720.pdf. Accessed: 2021-03-27.
- [79] T. Bickel, “A note on confined diffusion,” *Physica A: Statistical Mechanics and its Applications*, vol. 377, no. 1, pp. 24–32, 2007.
- [80] X. Michalet, “Mean square displacement analysis of single-particle trajectories with localization error: Brownian motion in an isotropic medium,” *Physical Review E*,

- vol. 82, no. 4, p. 041914, 2010.
- [81] B. Lin, J. Yu, and S. A. Rice, “Direct measurements of constrained brownian motion of an isolated sphere between two walls,” *Physical Review E*, vol. 62, no. 3, p. 3909, 2000.
- [82] T. Benesch, S. Yiacoumi, and C. Tsouris, “Brownian motion in confinement,” *Physical Review E*, vol. 68, no. 2, p. 021401, 2003.
- [83] X. Bian, C. Kim, and G. E. Karniadakis, “111 years of brownian motion,” *Soft Matter*, vol. 12, no. 30, pp. 6331–6346, 2016.
- [84] J. A. Kulkarni, M. M. Darjuan, J. E. Mercer, S. Chen, R. Van Der Meel, J. L. Thewalt, Y. Y. C. Tam, and P. R. Cullis, “On the formation and morphology of lipid nanoparticles containing ionizable cationic lipids and sirna,” *ACS nano*, vol. 12, no. 5, pp. 4787–4795, 2018.
- [85] C. Wan, T. Allen, and P. Cullis, “Lipid nanoparticle delivery systems for sirna-based therapeutics,” *Drug delivery and translational research*, vol. 4, no. 1, pp. 74–83, 2014.
- [86] J. A. Kulkarni, D. Witzigmann, J. Leung, R. van der Meel, J. Zaifman, M. M. Darjuan, H. M. Grisch-Chan, B. Thöny, Y. Y. C. Tam, and P. R. Cullis, “Fusion-dependent formation of lipid nanoparticles containing macromolecular payloads,” *Nanoscale*, vol. 11, no. 18, pp. 9023–9031, 2019.

- [87] J. A. Kulkarni, D. Witzigmann, S. Chen, P. R. Cullis, and R. van der Meel, “Lipid nanoparticle technology for clinical translation of sirna therapeutics,” *Accounts of chemical research*, vol. 52, no. 9, pp. 2435–2444, 2019.
- [88] Y. Chen, N. C. Deffenbaugh, C. T. Anderson, and W. O. Hancock, “Molecular counting by photobleaching in protein complexes with many subunits: best practices and application to the cellulose synthesis complex,” *Molecular biology of the cell*, vol. 25, no. 22, pp. 3630–3642, 2014.
- [89] C. Allen, N. Dos Santos, R. Gallagher, G. Chiu, Y. Shu, W. Li, S. Johnstone, A. Janoff, L. Mayer, M. Webb, *et al.*, “Controlling the physical behavior and biological performance of liposome formulations through use of surface grafted poly (ethylene glycol),” *Bioscience reports*, vol. 22, no. 2, pp. 225–250, 2002.
- [90] J. Viger-Gravel, A. Schantz, A. C. Pinon, A. J. Rossini, S. Schantz, and L. Emsley, “Structure of lipid nanoparticles containing sirna or mrna by dynamic nuclear polarization-enhanced nmr spectroscopy,” *J. Phys. Chem.*, vol. 122, no. 7, pp. 2073–2081, 2018.
- [91] S. Hirota, C. T. de Ilarduya, L. G. Barron, and F. C. Szoka Jr, “Simple mixing device to reproducibly prepare cationic lipid-dna complexes (lipoplexes),” *Biotechniques*, vol. 27, no. 2, pp. 286–290, 1999.
- [92] L. B. Jeffs, L. R. Palmer, E. G. Ambegia, C. Giesbrecht, S. Ewanick, and I. MacLachlan, “A scalable, extrusion-free method for efficient liposomal

- encapsulation of plasmid dna,” *Pharmaceutical research*, vol. 22, no. 3, pp. 362–372, 2005.
- [93] J. A. Kulkarni, Y. Y. C. Tam, S. Chen, Y. K. Tam, J. Zaifman, P. R. Cullis, and S. Biswas, “Rapid synthesis of lipid nanoparticles containing hydrophobic inorganic nanoparticles,” *Nanoscale*, vol. 9, no. 36, pp. 13600–13609, 2017.
- [94] G. Emilsson, R. L. Schoch, L. Feuz, F. Hook, R. Y. Lim, and A. B. Dahlin, “Strongly stretched protein resistant poly (ethylene glycol) brushes prepared by grafting-to,” *ACS applied materials & interfaces*, vol. 7, no. 14, pp. 7505–7515, 2015.
- [95] Z. Zhang, S. R. Park, A. Pertsinidis, and A. Revyakin, “Cloud-point peg glass surfaces for imaging of immobilized single molecules by total-internal-reflection microscopy,” *Bio-protocol*, vol. 6, no. 7, pp. e1784–e1784, 2016.
- [96] H. Shen, L. J. Tauzin, R. Baiyasi, W. Wang, N. Moringo, B. Shuang, and C. F. Landes, “Single particle tracking: From theory to biophysical applications,” *Chemical Reviews*, vol. 117, no. 11, pp. 7331–7376, 2017.
- [97] C. Manzo and M. F. Garcia-Parajo, “A review of progress in single particle tracking: from methods to biophysical insights,” *Reports on Progress in Physics*, vol. 78, no. 12, 2015.
- [98] M. K. Cheezum, W. F. Walker, and W. H. Guilford, “Quantitative comparison of algorithms for tracking single fluorescent particles,” *Biophysical Journal*, vol. 81, no. 4, pp. 2378 – 2388, 2001.

- [99] C. Anderson, G. Georgiou, I. Morrison, G. Stevenson, and R. Cherry, “Tracking of cell surface receptors by fluorescence digital imaging microscopy using a charge-coupled device camera. low-density lipoprotein and influenza virus receptor mobility at 4 degrees c,” *Journal of Cell Science*, vol. 101, no. 2, pp. 415–425, 1992.
- [100] G. Schütz, H. Schindler, and T. Schmidt, “Single-molecule microscopy on model membranes reveals anomalous diffusion,” *Biophysical Journal*, vol. 73, no. 2, pp. 1073 – 1080, 1997.
- [101] J. Happel and H. Brenner, *Low REynolds Number Hydrodynamics*. Kluwer, 1983.
- [102] K. Tsekouras, T. C. Custer, H. Jashnsaz, N. G. Walter, and S. Pressé, “A novel method to accurately locate and count large numbers of steps by photobleaching,” *Molecular biology of the cell*, vol. 27, no. 22, pp. 3601–3615, 2016.
- [103] J. Garry, Y. Li, B. Shew, C. C. Gradinaru, and A. D. Rutenberg, “Bayesian counting of photobleaching steps with physical priors,” *The Journal of chemical physics*, vol. 152, no. 2, p. 024110, 2020.
- [104] Y. Chen, N. C. Deffenbaugh, C. T. Anderson, and W. O. Hancock, “Molecular counting by photobleaching in protein complexes with many subunits: best practices and application to the cellulose synthesis complex,” *Molecular Biology of the Cell*, vol. 25, no. 22, pp. 3630–3642, 2014.
- [105] B. Kundukad, J. Yan, and P. S. Doyle, “Effect of yoyo-1 on the mechanical properties of dna,” *Soft matter*, vol. 10, no. 48, pp. 9721–9728, 2014.

- [106] T. Odijk, “Polyelectrolytes near the rod limit,” *Journal of Polymer Science: Polymer Physics Edition*, vol. 15, no. 3, pp. 477–483, 1977.
- [107] J. Skolnick and M. Fixman, “Electrostatic persistence length of a wormlike polyelectrolyte,” *Macromolecules*, vol. 10, no. 5, pp. 944–948, 1977.
- [108] A. V. Dobrynin, “Electrostatic persistence length of semiflexible and flexible polyelectrolytes,” *Macromolecules*, vol. 38, no. 22, pp. 9304–9314, 2005.
- [109] G. S. Manning, “The persistence length of dna is reached from the persistence length of its null isomer through an internal electrostatic stretching force,” *Biophysical Journal*, vol. 91, no. 10, pp. 3607–3616, 2006.
- [110] C. G. Baumann, S. B. Smith, V. A. Bloomfield, and C. Bustamante, “Ionic effects on the elasticity of single dna molecules,” *Proceedings of the National Academy of Sciences*, vol. 94, no. 12, pp. 6185–6190, 1997.
- [111] A. Brunet, C. Tardin, L. Salomé, P. Rousseau, N. Destainville, and M. Manghi, “Dependence of dna persistence length on ionic strength of solutions with monovalent and divalent salts: A joint theory–experiment study,” *Macromolecules*, vol. 48, no. 11, pp. 3641–3652, 2015.
- [112] C. M. J. McFaul, J. Leith, B. Jia, F. Michaud, A. Arsenault, A. Martin, D. Berard, and S. Leslie, “Single-molecule microscopy using tunable nanoscale confinement,” in *Physical Chemistry of Interfaces and Nanomaterials XII* (N. Banerji and C. Silva,

- eds.), vol. 8811, pp. 1 – 12, International Society for Optics and Photonics, SPIE, 2013.
- [113] G. Slater, C. Holm, M. Chubynsky, H. De Haan, A. Dubé, K. Grass, O. Hickey, C. Kingsburry, D. Sean, T. Shendruk, and L. Z., “Modeling the separation of macromolecules: A review of current computer simulation methods,” *Electrophoresis*, vol. 30, pp. 792–818, 2009.
- [114] J. D. Weeks, D. Chandler, and H. C. Andersen, “Role of repulsive forces in determining the equilibrium structure of simple liquids,” *The Journal of chemical physics*, vol. 54, no. 12, pp. 5237–5247, 1971.
- [115] G. S. Grest and K. Kremer, “Molecular dynamics simulation for polymers in the presence of a heat bath,” *Phys. Rev. A*, vol. 33, pp. 3628–3631, May 1986.
- [116] D. Dimitrov, A. Milchev, K. Binder, L. I. Klushin, and A. M. Skvortsov, “Universal properties of a single polymer chain in slit: Scaling versus molecular dynamics simulations,” *The Journal of chemical physics*, vol. 128, p. 234902, 2008.
- [117] E. K. K. B. G. M. W. Jaroslaw Grobelny, “Detection limits of dls and uv-vis spectroscopy in characterization of polydisperse nanoparticles colloids,” *Journal of Nanomaterials.*, vol. 2013, 2013.
- [118] U. Joanne Lannigan, “Analytical challenges of extracellular vesicle detection: A comparison of different techniques,” *Journal of Quantitative Cell Science*, 2015.

-
- [119] R. H. Victoria Shpacovitch, “Optical and surface plasmonic approaches to characterize extracellular vesicles. a review,” *Analytica Chimica Acta*, vol. 1005, pp. 1–15, 2018.
- [120] E. H. Adelson, C. H. Anderson, J. R. Bergen, P. J. Burt, and J. M. Ogden, “Pyramid methods in image processing,” *RCA engineer*, vol. 29, no. 6, pp. 33–41, 1984.
- [121] R. L. Gregory, *The intelligent eye*. ERIC, Weidenfeld & Nicolson, 1970.
- [122] T. Lindeberg, “Image matching using generalized scale-space interest points,” *Journal of mathematical Imaging and Vision*, vol. 52, no. 1, pp. 3–36, 2015.
- [123] H. Qian, M. P. Sheetz, and E. L. Elson, “Single particle tracking. analysis of diffusion and flow in two-dimensional systems,” *Biophysical journal*, vol. 60, no. 4, pp. 910–921, 1991.